INTERROGATING THE INTERACTIONS OF ONCOGENIC KRAS MUTANTS WITH SOS AND BRAF

A Dissertation

by

ZAHRA MOGHADAMCHARGARI

Submitted to the Graduate and Professional School of
Texas A&M University
In partial fulfillment of the requirements for the degree of

DOCTOR OF PHILOSOPHY

Chair of Committee,	Arthur Laganowsky
Committee Members,	David H. Russell
	Frank M. Raushel
	Thomas Meek
Head of Department,	Simon North

August 2021

Major Subject: Chemistry

ABSTRACT

Mutations in RAS are associated with many different cancers, and RAS has been a therapeutic target for more than three decades. Studying the biochemical properties of RAS mutants and most importantly the interaction with activator and downstream effectors lay a foundation to better understand how RAS functions in signaling pathway. In chapter 2, high-resolution native mass spectrometry (MS) was used to determine the kinetics and transition state thermodynamics of intrinsic hydrolysis for KRAS and oncogenic mutants. MS data reveal heterogeneity where both 2'-deoxy and 2'-hydroxy forms of GDP (Guanosine diphosphate) and GTP (Guanosine triphosphate) are bound to the recombinant enzyme. In addition, MS results show that the transition state thermodynamics for the intrinsic GTPase activity of KRAS is both enthalpically and entropically unfavorable. The oncogenic mutants, G12C, Q61H and G13D unexpectedly exhibit a higher 2'-deoxy GTP intrinsic hydrolysis rate compared to that for GTP.

In chapter 3, the interaction of RAS mutants with a specific guanine nucleotide exchange factor, Son of Sevenless (SOS), is studied. Native ion mobility-mass spectrometry was employed to monitor the assembly of the catalytic domain of SOS (SOS^{cat}) with KRAS and three cancer-associated mutants (G12C, G13D, and Q61H), leading to the discovery of different molecular assemblies and distinct conformers of SOS^{cat} engaging KRAS. Also, $KRAS^{G13D}$ exhibits high affinity for SOS^{cat} and is a potent allosteric modulator of its activity. A structure of the $KRAS^{G13D}$•SOS^{cat} complex was determined using cryogenic electron microscopy providing insight into the enhanced affinity of the mutant protein. In addition, we find that $KRAS^{G13D}$-GTP can allosterically increase the nucleotide exchange rate of KRAS at the active site more than two-fold compared to KRAS-GTP. Furthermore, small molecule RAS•SOS disruptors fail to dissociate $KRAS^{G13D}$•SOS^{cat} complexes underscoring the need for more potent disruptors.

Lastly, chapter 4 is focused on the biochemical characterization of BRAF, a downstream effector of RAS. Our results indicate that BRAF populates different stoichiometries with MEK1 and 14-3-3 dimers. In the presence of ATP, BRAF undergoes dimerization suggesting that ATP promotes the activation of BRAF. In addition, copper stimulates the dimerization of BRAF in MEK1-independent manner.

DEDICATION

First and foremost, I would like to dedicate my thesis to the love of my life, Mehdi Shirzadeh, who has always been supportive, inspiring and cooperative during the hardships of graduate school and life. This work is also dedicated to my amazing parents for their endless love, sacrifice and prayers and to my sister, Azam, who has been a role model to me to work hard and pursue my dreams.

ACKNOWLEDGEMENTS

I would like to express my deepest gratitude and appreciation to my committee chair, Dr. Arthur Laganowsky, for giving me the opportunity to do research in his group and for his invaluable guidance throughout my PhD. He always encouraged me to work hard and raised a spirit of adventure in my research. This dissertation would not have been possible without his patience and persistent help.

I would also like to thank my committee members, Professors David H. Russell, Thomas Meek and Frank Raushel for their guidance and support throughout the course of this research. Thanks also go to my friends and colleagues and the department faculty and staff for making my time at Texas A&M University a great experience.

CONTRIBUTORS AND FUNDING SOURCES

Contributors

1. Faculty committee recognition

This work was supervised by a thesis (or) dissertation committee consisting of Professors Arthur Laganowsky and David H. Russell and Frank Raushel of the Department of Chemistry and Professor Thomas Meek of the Department of Biochemistry.

2. Collaborator contribution

The Cryo-electron microscopy data for chapter 3 was provided by our collaborator, Professor Minglei Zhao.

All other work conducted for the thesis (or) dissertation was completed by the student independently.

Funding Sources

Graduate study was supported by National Institute of Health (NIH) NCI and NCI/NIGMS (RO1GM121751), NIGMS (DP2GM123486), and NIH (P41GM128577). Part of this work was performed at the National Center for Cryo EM Access and Training (NCCAT) and the Simons Electron Microscopy Center located at the New York Structural Biology Center, supported by the NIH Common Fund Transformative High Resolution Cryo-Electron Microscopy program (U24 GM129539,) and by grants from the Simons Foundation (SF349247) and NY State Assembly.

NOMENCLATURE

KRAS	Kirsten rat sarcoma viral oncogene homolog
HRAS	Harvey rat sarcoma viral oncogene homolog
NRAS	Neuroblastoma RAS viral oncogene homolog
GTPase	Guanosine triphosphatase
GTP	Guanosine triphosphate
GDP	Guanosine diphosphate
GppNp	Guanosine 5’-[β,γ-imido] triphosphate trisodium)\
Mant-GTP γS	2'/3'-O-(N-Methyl-anthraniloyl)-guanosine-5'-(γ-thio)-triphosphate
BODIPY-GTP	2'/3'-O-(2-Aminoethyl-carbamoyl)-Guanosine-5'-triphosphate
GEFs	Guanine nucleotide exchange factors
GAPs	GTPase activating proteins
RTKs	Receptor tyrosine kinases
EGFR	Epidermal growth factor receptor
Grb2	Growth factor receptor-bound protein 2
MEK1/2	Extracellular signal regulated kinase ½
PM	Plasma membrane
PI3K	Phosphatidylinositol 3-kinase
PDK1	3-phosphoinositide-dependent kinase 1
mTOR	Mammalian target of rapamycin
PIP2	Phosphatidylinositol-3,4-biphosphate
PIP3	Phosphatidylinositol-3,4,5-biphosphate

HVR	Hypervariable region
SOS	Son of Sevenless
Rem	RAS exchanger motif
CR	Conserved region
CRD	Cystein rich domain
RBD	RAS binding domain
MS	Mass spectrometry
CSD	Charge state distribution
ESI	Electrospray ionization
CRM	Charge residue model
IEM	Ion evaporation model
CEM	Chain ejection model
CID	Collision induced dissociation
SID	Surface induced dissociation
ECD	Electron capture dissociation
UVPD	Ultra violet photo dissociation
IM	Ion mobility spectrometry
DTIMS	Drift tube ion mobility spectrometry
TWIMS	Traveling wave ion mobility spectrometry
FAIMS	Field-asymmetric ion mobility spectrometry
CCS	Collision cross section
DC	Direct current
RF	Radio frequency

FTICR	Fourier transform ion cyclotron resonance
EMR	Extended mass range
UHMR	Ultra high mass range
Cryo-EM	Cryo-electron microscopy
TEV	Tobacco Etch Virus
EDTA	Ethylenediaminetetraacetic acid
β –ME	β-Mercaptoethanol

TABLE OF CONTENTS

Page

LIST OF FIGURES

Page

LIST OF TABLES

Page

1. INTRODUCTION

1.1. RAS signaling

RAS mutations were first discovered more than 30 years ago, and numerous studies have since characterized RAS proteins as major oncogenes that approximately found in 30% of human cancers (1, 2). The implication of RAS in different types of cancer prompted researchers to identify and characterize the biochemical behavior of RAS proteins for more than three decades (3). RAS proteins are members of small GTPases that act as molecular switches by alternating between active GTP bound and inactive GDP bound states. The activation of RAS is tightly regulated by Guanine nucleotide exchange factor (GEFs) such as Son of Sevenless (SOS) that catalyzes the exchange of GDP by GTP (4). Inactivation of RAS is regulated by GTPase activating proteins (GAPs) that accelerate the intrinsic GTP hydrolysis by 10^5 factor (5). RAS proteins regulate diverse cellular processes including differentiation, proliferation, apoptosis and survival (6, 7). RAS signaling is initiated through the activation of integral membrane receptors called receptor tyrosine kinases (RTKs) such as epidermal growth factor receptors (EGFR). Upon activation of EGFR by epidermal growth factor (EGF) ligands (8), the signal is communicated to other proteins downstream of EGFR. (Figure 1.1). One of these proteins is SOS that is recruited to the plasma membrane (PM) by adaptor proteins such as Grb2. SOS facilitates the exchange of GDP by GTP and activates RAS. It has been shown that RAS bound to GTP can form a dimer or higher order oligomers called RAS nanoclusters that has an essential role in signal transmission and provide binding site for effector binding. Dimers or higher architecture of RAS bound to GTP binds to downstream effector, RAF kinase, leading to the phosphorylation and dimerization of RAF ready to bind to its substrate MEK1/2 (9, 10). RAF dimers phosphorylates MEK1/2, and MEK1/2

phosphorylates and activates ERK1/2. ERK1/2 subsequently activates and phosphorylates other transcription factors leading to gene transcription, cell proliferation and differentiation (11). RAS is also involved in another signaling pathway called RAS-PI3K-Akt pathway (12, 13). In this pathway, active RAS recruits PI3K (Phosphatidylinositol 3-kinase) to PM where it binds to its substrate PIP2 (Phosphatidylinositol-3,4-biphosphate) and phosphorylates PIP2 to PIP3 (Phosphatidylinositol-3,4,5-biphosphate). PIP3 in turn recruits PDK (3-phosphoinositide-dependent kinase 1) and Akt to PM, and PDK activates Akt, and Akt in turn phosphorylates mTOR (mammalian target of rapamycin) leading to cell growth and survival.

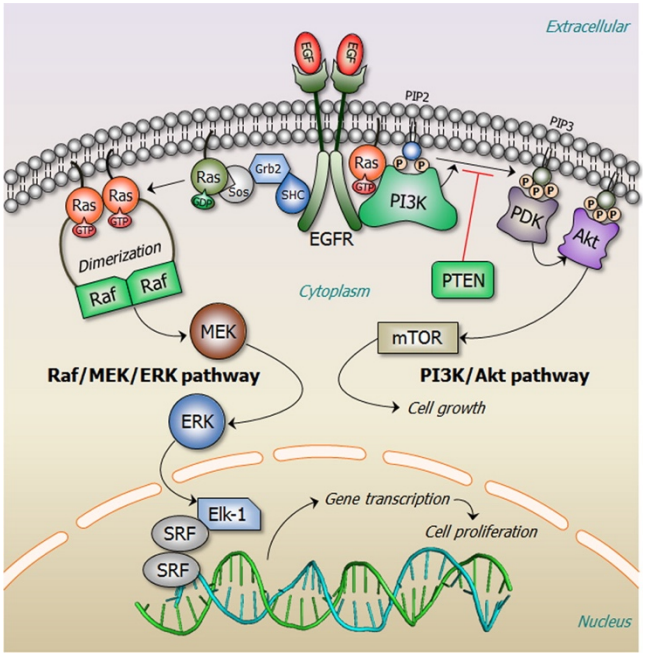

Figure 1.1. RAS signaling in the mitogen-activated protein kinase (MAPK), RAF−MEK−ERK pathway, and phosphatidylinositol 3-kinase (PI3K)/Akt pathway. Reprinted with permission from *Chemical Review*, 116, 6607-665. Copyright 2016, American Chemical Society.

1.2. Isoforms of RAS and cancer implication

The three human RAS genes [Kirsten rat sarcoma viral oncogene homolog (KRAS), neuroblastoma RAS viral oncogene homolog (NRAS) and Harvey rat sarcoma viral oncogene homolog (HRAS)] encode four RAS proteins, with two KRAS isoforms (KRAS4A and KRAS4B) which arises from alternative RNA splicing (14). KRAS4B is the predominant splice variant and expressed in many tissues and hence is the focus of cancer research. Multiple sequence alignment shows that all RAS isoforms share highly conserved sequence similarity (89%) in the catalytic domain and an extremely low sequence identity (8%) observed in hypervariable region (HVR) that recruits RAS to PM. Despite a high sequence similarity across RAS isoforms, the frequency and distribution of RAS mutations are not the same. KRAS is the most frequently mutated isoform (86%) followed by NRAS (11%) and HRAS (3%) (15, 16). Each mutated RAS isoform appears in different tumor types, for example KRAS mutations are detected at very high frequency in lung, colon and pancreatic ductal adenocarcinoma tumors. NRAS mutations occur in hematopoietic tumors and in malignant melanomas, whereas HRAS mutations are the most frequent in bladder tumors and head and neck squamous cell carcinoma (17, 18). The majority of oncogenic RAS mutations are found at amino acid residues glycine 12 and 13, and Q61. These mutations impair the intrinsic and GAPs-mediated hydrolysis of GTP and lock the protein in an active state and hence prolong downstream signaling associated with oncogenic cell growth (19-21). The catalytic domain of RAS consists of six ß-strands flanked by five α-helices and ten connecting loops(22, 23) (Figure 1.2A). Three regions of RAS constitute the active site of GDP or GTP including functional p-loop (residues 10-17), switch I (30-38) and switch II (59-76).

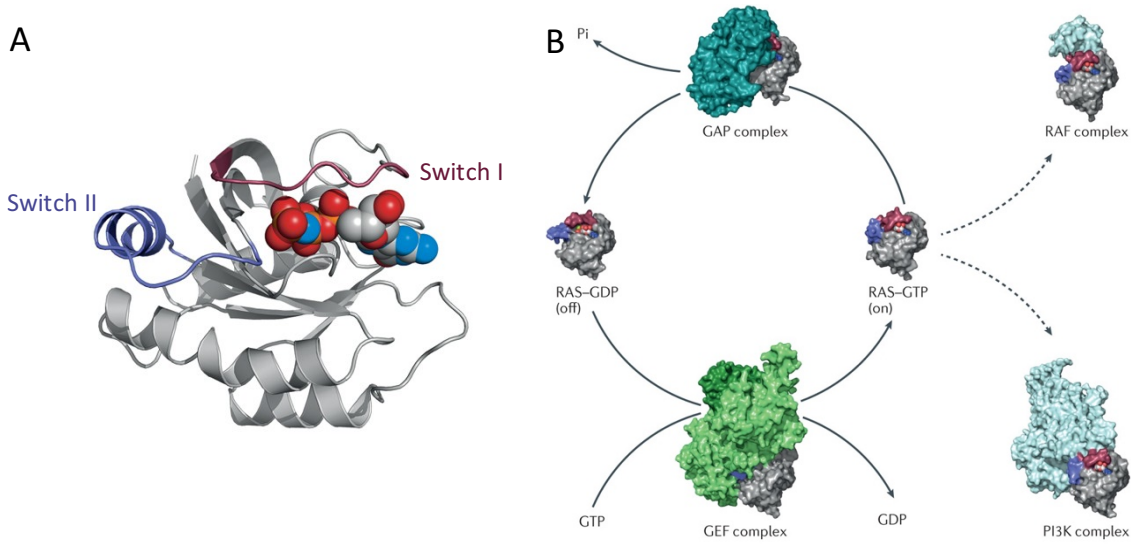

Figure 1.2. The catalytic domain of RAS and RAS nucleotide exchange cycle. (A) the crystal structure of catalytic domain of RAS with switch I and II shown in dark pink and blue, respectively. (B) RAS switches between active GTP bound state and inactive GDP bound state. The activation and inactivation of RAS is facilitated by GEFs and GAPs, respectively. Reprinted with permission from *Nature Reviews Drug Discovery*, 15, 771-785. Copyright 2016, Nature Publishing Group, a division of Macmillan Publishers Limited. All Rights Reserved.

1.3. The interaction of RAS with SOS

The activity of RAS is regulated by switching between GDP bound and GTP bound states (Figure 1.2B). RAS has a slow intrinsic nucleotide exchange rate ($2x10^{-3}$ s^{-1}) that is catalyzed by GEFs via exchanging GDP for GTP (24, 25), and the active RAS as a product can interact and activate downstream effectors including RAF kinase and PI3K complex (Figure 2B). SOS is a RAS-specific GEFs that accelerates the exchange of GDP for GTP by several orders of magnitude (26). Human SOS has ~1330 residues with different domains including histone domains, a DbI homology (DH) domain, a pleckstrin (PH) domain followed by the catalytic domain (SOS^{cat}) that consists of RAS exchanger motif (Rem) and Cdc25 domian (4) (Figure 1.3A). SOS is recruited to PM at the C-terminus which provides docking sites for adaptor protein Grb2 (27). The first crystal

structure of HRAS in complex with SOS^{cat} shows that HRAS is bound to Cdc25 without any contact with Rem domain (28). Two helices of SOS^{cat} including αH and αI are inserted into the nucleotide binding site of RAS inducing conformational change in the p-loop, switch I and switch II regions of HRAS. The pronounced deviation of switch I and II of HRAS leads to the opening of nucleotide binding site which in turn facilitates the release of the nucleotide and binding to an abundant extracellular GTP. The subsequent studies on regulation of RAS by SOS revealed an unexpected discovery of a second RAS bound to SOS^{cat} (29) (Figure 1.3B). The second RAS was distal to RAS bound to CdC25 domain (active site) and was located between Rem and CdC25. Further characterization of the ternary complex showed that RAS bound to distal site can allosterically increase the rate of the nucleotide exchange at the active site, and that the increase in rate is more considerable for RAS bound GTP (RAS-GTP) (29).

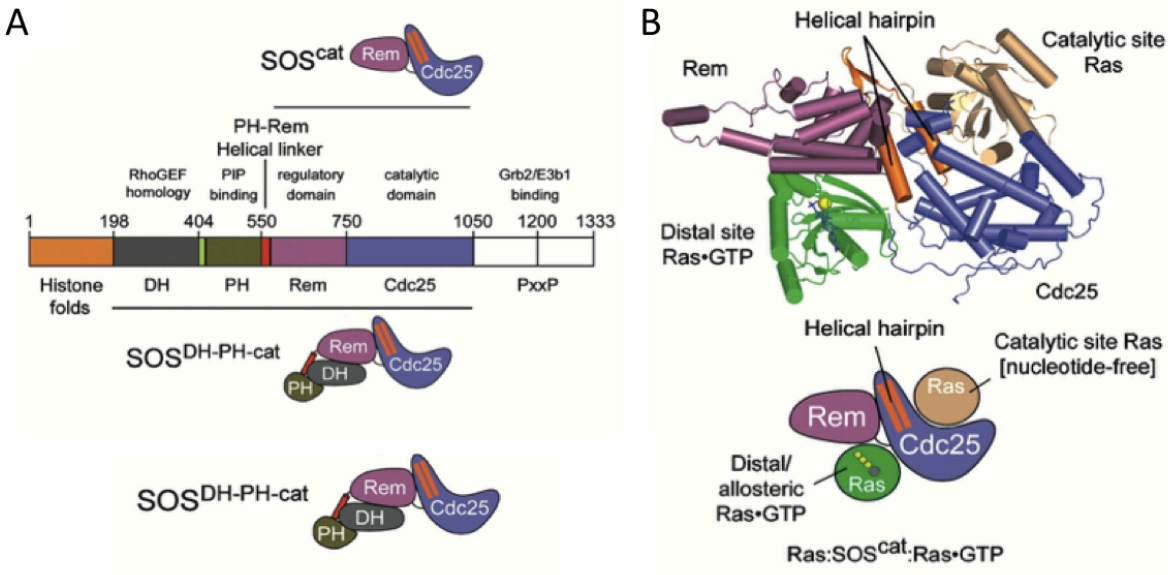

Figure 1.3. Domain organization and structure of SOS in complex with RAS. (A) Different domains of SOS along with catalytic domain are shown. (B) The structure of $HRAS:SOS^{cat}:HRAS^{Y64A}$.GTP complex reveals two different sites for RAS binding including active and allosteric sites. Reprinted with permission from *Cell*, 119, 393-405. Copyright 2004 by Cell press.

1.4. Interaction of RAS with RAF

RAF kinases are downstream effectors of RAS, and association with RAS-GTP leads to the activation of RAF kinases (30, 31). The aberrant alterations in RAF is the onset of different kinds of cancers, most notably melanoma. Three different RAF isoforms are expressed in mammals including ARAF, CRAF and BRAF, the latter being a most frequently mutated kinase in human cancer (32). All RAF paralogs share three conserved regions including CR1, CR2 and CR3 (33) . CR1 located at N terminus contains RAS binding domain (RBD) that binds active RAS-GTP and a cysteine rich domain (CRD) that localizes RAF to PM and binds to two Zn^{2+} ions (Figure 1.4A).

CR2 is a serine/threonine rich region and CR3 contains the catalytic domain of RAF that undergo dimerization upon RAF activation. Intramolecular interaction between the N-terminus of RAF with the C-terminus kinase domain shifts RAF in an autoinhibited conformation and renders RAF as an inactive cytosolic conformer (31). Recent Cryo electron microscopy of full length BRAF in complex with MEK1 and 14-3-3 dimers shows that BRAF is in quiescent state and adopts an inactive state (Figure 1.4B) (34). The phosphorylation of different amino acid positions in CR2 (S365) and CR3 (S729) provide docking sites for 14-3-3 dimers and dephosphorylating of S365 drives the active dimerization of RAF enabling the phosphorylation of MEK1, the RAF substrate (Figure 1.4C). Thus, the phosphorylation of S365 and 729 and binding to 14-3-3 dimers are driving forces to convert RAF into regulated, inactive monomer unable to form dimers. Dephosphorylation of inhibitory sites of S365 and S729 (Figure 1.4C), binding active RAS-GTP to RBD and phosphorylation of activating kinase segments release the autoinhibited conformation and drive the activation of RAF into homodimers or heterodimers and initiates a cascade of phosphorylation of MEK1/2 and MEK1/2 subsequently phosphorylates ERK1/2.

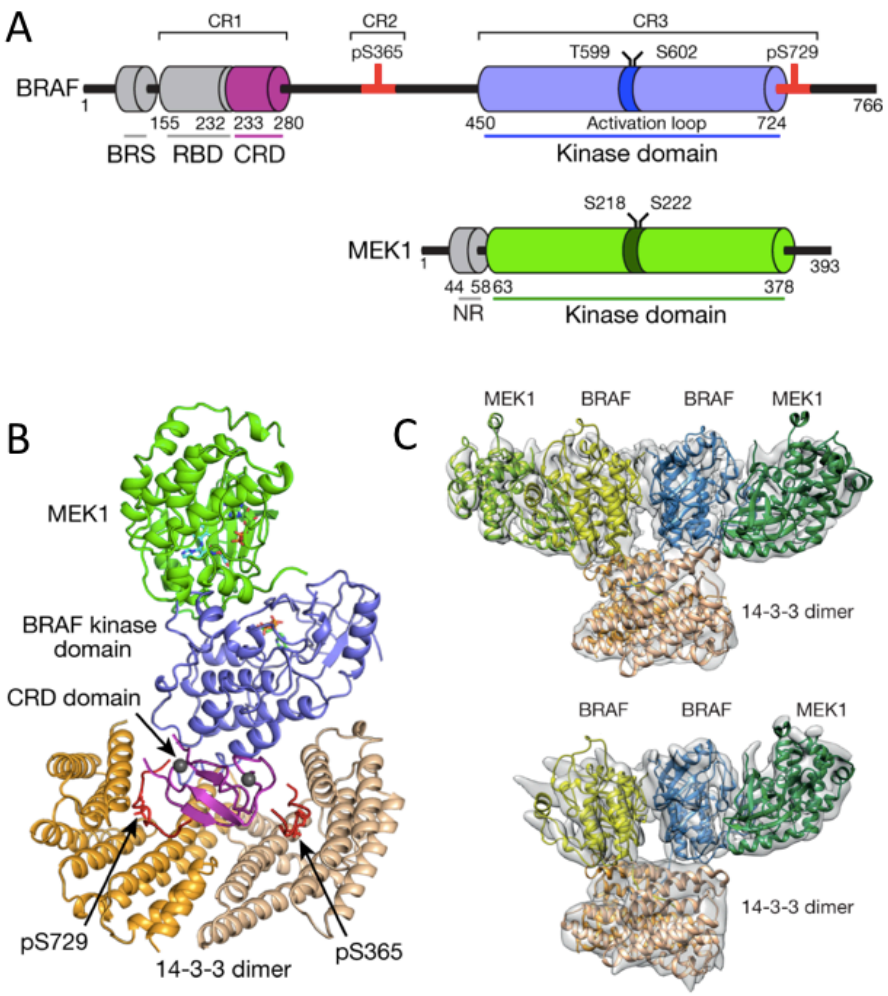

Figure 1.4. BRAF in complex with MEK1 and 14-3-3 dimers. (A) Domain organization of BRAF and MEK1. The phosphorylation sites are shown on top of the cartoon and different domains at the bottom. (B) The cartoon representation of BRAF bound to MEK1 and 14-3-3 dimers (orange and tan). BRAF, MEK1 and CRD domains are coloured similarly to (A). CRD is bound to two Zn2+ ions shown by dark grey spheres. (C) Dephosphorylation at S365 (S365A) leads to dimerization of BRAF with one or two MEK1 bound subunits. 14-3-3 dimer bridges between two BRAF monomers. Reprinted with permission from *Nature*, 575, 545-550. Copyright 2019, The Park *et al*, under exclusive license to Springer Nature Limited.

1.5. Native Mass Spectrometry (MS)

Native mass spectrometry (MS) has evolved as a powerful analytical technique for structural biology since 1990 (35). Native MS refers to the analysis of biological samples at their native state by means of non-denaturing buffers and optimization of instrumental parameters to remove salts

and adducts without disruption of the structure (36). In contRASt to denaturing MS in which non-covalent interactions of proteins are disrupted by organic solvents, non-covalent interactions of protein and protein complexes are preserved throughout native MS experiments. One of the evidences of preserving native like structure of proteins detected by native MS is exhibited by narrower charge state distribution (CSD) of proteins compared to traditional denatured MS. For example, the native MS of bovine serum albumin adopts an average charge of +15 (Figure 1.5B). In contrast, the CSD of denatured MS of bovine serum albumin in the presence of 1% formic acid shifted to 50+ due to more expanded/unfolded structure of the protein enabling the exposed basic amino acids to adopt charge and therefore having a wider CSD (Figure 1.5A). As shown in figure 1.5B, a mixture of proteins are analyzed using native and denaturing MS. While denatured MS shows convolved CSD at lower m/z region, native MS shows separation of all five proteins each of which representing a narrow CSD and well-resolved charge states and hence report the molecular weight and stoichiometry of proteins (Figure 1.5B). Other peaks are observed for serum albumin and apo ferritin demonstrating the ability of MS to report the heterogeneity of sample. Native MS therefore provides information on protein complexes and their subunit stoichiometry (37), protein dynamics and topology (38, 39), binding partners (RNA, DNA, lipids, etc) and equilibrium binding constants (40), thermodynamics and kinetics (41, 42).

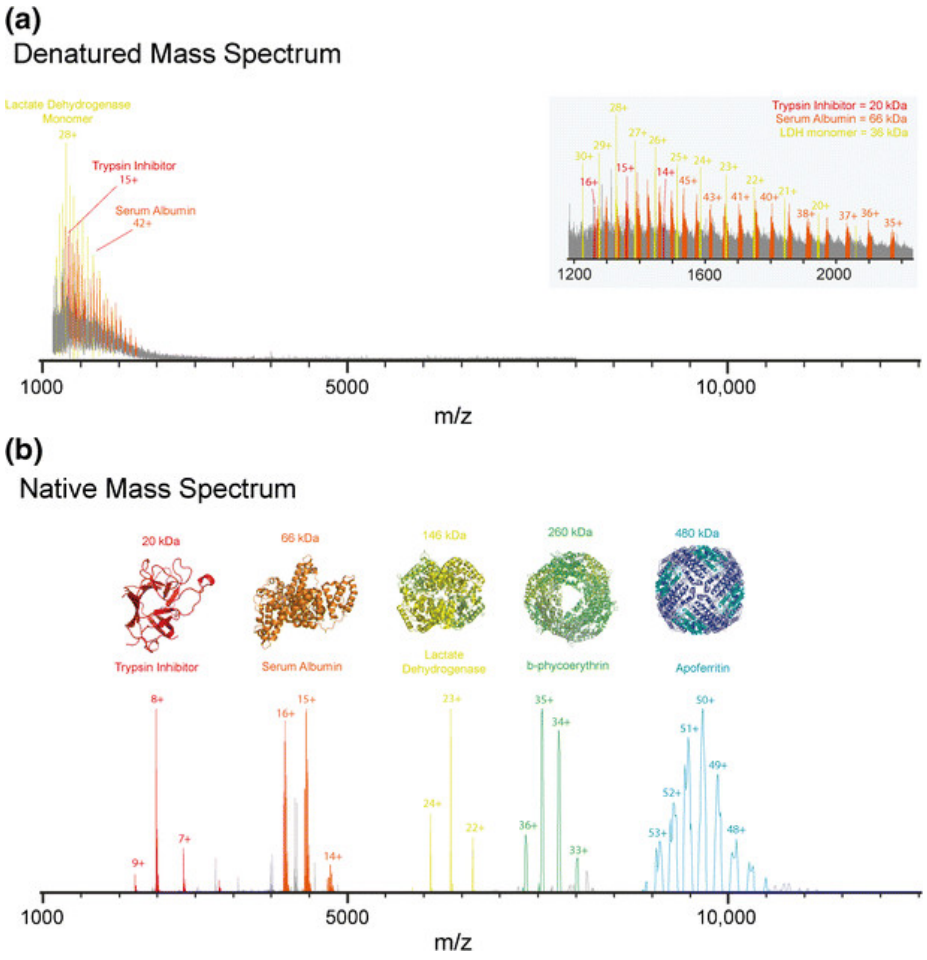

Figure 1.5. The comparison of denatured versus native MS of identical protein mixtures. (A) Denatured and (B) native mass spectra of a mixture of proteins, trypsin inhibitor (red), serum albumin (orange), B-phycoerythrin (green), lactate dehydrogenase (yellow) and apoferritin (blue). Denatured and native mass spectra are acquired in water:acetonitrile:formic acid in 50:49:1 ratio or 100 mM ammonium acetate (pH=7.4), respectively. In contRASt to denatured mass spectrum showing different proteins are clustered in low m/z region with average high charge, native mass spectrum reveals separate, resolved CSD for each protein with lower average charge state. Native mass spectra of serum albumin and apoferritin also display heterogeneity. Reprinted with permission from *JASMS*, 28, 5-13. Copyright 2017 Leney *et al*.

1.6. Electrospray ionization

Native MS studies of proteins or protein complexes utilizes a soft ionization technique to ionize biomolecule samples such as nano-electrospray ionization (ESI) method that induce little or no structural perturbation of protein complexes (43, 44). In this technique, a high electric potential is

applied using a platinum wire or gold-coating capillary emitter containing the biomolecule of interest. The applied potential geneartes charged droplets at the tip of the capillary forming a "taylor cone" (45, 46) which in turn promotes the formation of nascent charged droplets (Figure 1.6). The droplets undergo solvent evaporation and are transmitted inside of the mass spectrometer due to potential and pressure gradient. The solvent evaporation results in droplets shrinkage until the surface tension holding the droplet together is equal to the columbic repulsion of charges confined in a droplet leading to droplet fission, and ultimately gas phase ions are generated. The advantages of nano-ESI is to produce droplets with smaller diameters to aid better desolvation and also lower flow rates (nl/min) which decreases sample amount for analysis to a few microliter.

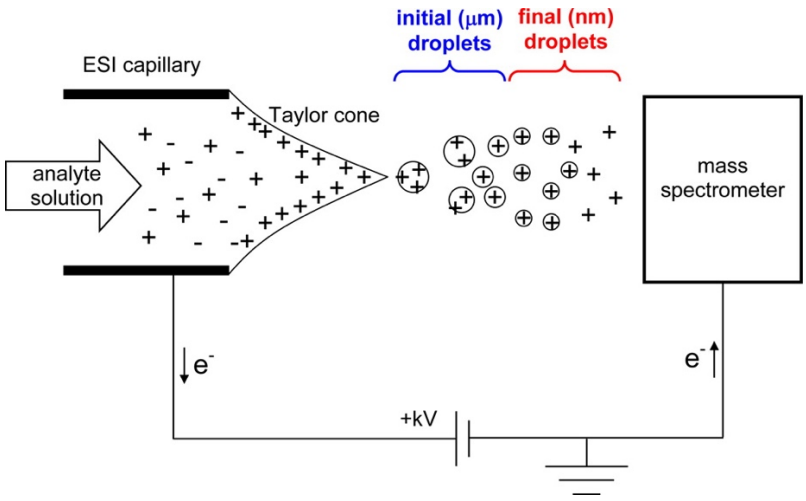

Figure 1.6. Electrospray ionization source schematics. Charged droplets emitted from capillary undergo fission and evaporation to yield naked gas phase ions. Reprinted with permission from *Analytical Chemistry*, 85, 2-9. Copyright 2013, American Chemical Society.

1.7. The mechanism of ion formation in ESI

In spite of simple implementation of ESI, the mechanism of ion formation is not very well understood and it is still the subject of debate among MS community. ESI produces multiply charged ions in the form of $[M+nH]^{n+}$ where M is the molecular weight of the protein and n is the

number of proton adducted to the protein. There are two principal models proposed on how ions are generated during ESI process: ion evaporation model (IEM) (47, 48) and charge residue model (CRM) (49). In IEM model, due to the excess charge inside the droplet and columbic repulsion between analyte ion and other charges, ion is pushed to the surface of the droplet and ultimately to the gas phase (Figure 1.7A). This model has been shown to be applicable for small ions. In CRM, the droplets undergo fission and evaporation until they yield the naked gas phase ions (Figure 1,7B). It is widely recognized that large folded proteins and protein complexes ions (>6000 Da) are generated using CRM model (46, 50). Unfolded and disordered proteins do not follow CRM model but rather follows a proposed model referred to as chain ejection model (CEM) (51). In folded globular species, polar residues reside at the surface whereas nonpolar and hydrophobic parts are buried and are not solvent accessible. A different scenario exist for unfolded species in which hydrophobic core is solvent exposed and protein adopts more extended structure. The more extended/hydrophobic nature of the protein makes it unfavorable to stay inside the droplet and it will subsequently be ejected from droplet (Figure 1,7C). The other extended/unfolded chains sequentially are expelled to the gas phase. Overall, IEM, CRM and CEM provide plausible mechanisms of ion formation for small molecules, folded and unfolded proteins, respectively.

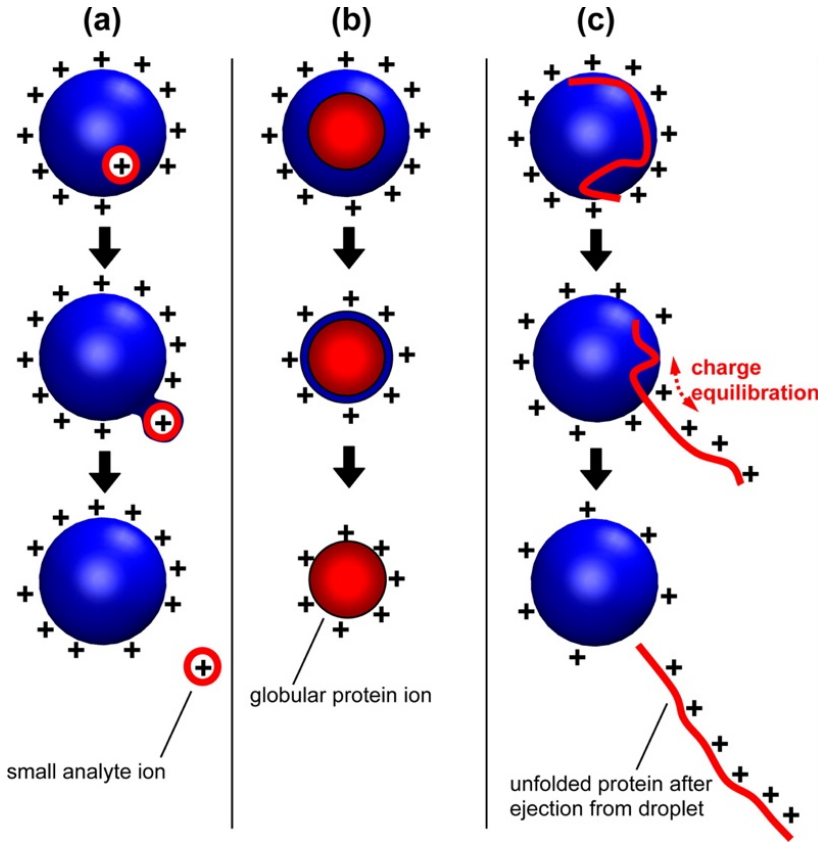

Figure 1.7. Different mechanisms of ion formation during ESI process. (A) IEM model shows the ejection of a small ion from droplet surface into the gas phase. (B) CRM illustrates that the final charge remained on the surface of the released gas phase ion is inherited from the charge on the initial droplet. (C) CEM displays the ejection of a disordered region of the protein due to high gained charge after ionization. Reprinted with permission from *Analytical Chemistry*, 85, 2-9. Copyright 2013, American Chemical Society.

1.8. Dissociation and activation of protein complexes

Although much effort has been made to maintain non-covalent interactions of protein complexes in gas phase over the past decades, activation and dissociation of ions becomes an interesting route to gain compositional information of protein complexes and their constituents (52). Several ion activation methods have been developed to gain structural insight of protein complexes including collision-induced dissociation (CID) (52), surface-induced dissociation (SID) (53), electron capture dissociation (ECD) (54) and UVPD (55). However, the majority of data acquired for

dissociation of large protein complexes has been collected using CID. These activation methods provide invaluable information on subunit stoichiometry, composition and topology of protein complexes (56, 57) and aid to determine the accurate molecular weight of different subunits by removing adducts and solvent adducted to the protein during ESI process.

1.8.1. Collision-induced dissociation (CID)

During CID process, gas phase ions undergo colliding with inert gas molecules (58) such as nitrogen and argon and their translational energy converted to internal energy leading to subsequent dissociation of subunits if the activation barrier is overcome (59, 60) (Figure 1.8A). The mechanism of CID process proposed by Benesch(61) suggests that multiple collisions with gas molecules causes a local unfolding of the protein and charge migration occurs to newly exposed area. Due to the further collisions with neutral gas molecules, more unfolding and charge migration occurs until the columbic repulsion balances with intramolecular forces keeping the unfolded monomer to the rest of the complex and unfolded subunit eventually dissociates. This process yields a highly-charged unfolded subunit with large surface area and a relatively lowly charged folded complex missing one subunit (stripped oligomer, n-1 mer) (Figure 1.8C). Charge partitioning during CID process is asymmetric according to mass as higher mass stripped oligomer carries less charge compared to monomer, but it is symmetric according to the surface area. The sum of the charges of stripped oligomer and highly-charged monomer corresponds to the charge of the precursor ion.

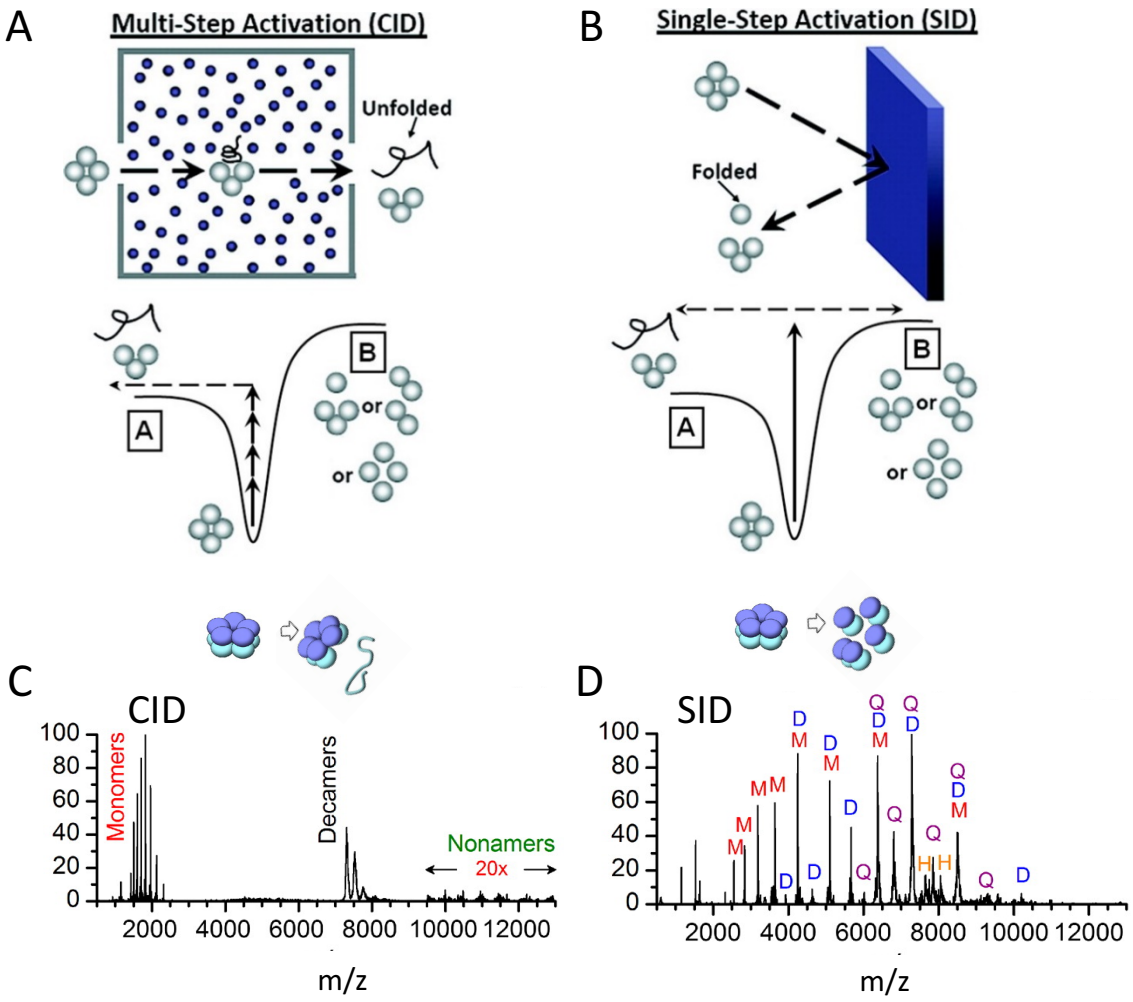

Figure 1.8. Dissociation pathway of noncovalent protein complexes illustrated by CID and SID. (A) In CID, a highly charged unfolded subunit is dissociated after undergoing multiple collisions with small gas molecules. (B) A fast, single step activation of ions with a surface target that leads to dissociation of folded subunits. (C) CID of a decameric protein complex results in an ejection of a highly charged unfolded monomer and a stripped oligomer (nonamer) at higher m/z region. (D) SID of the same decameric complex generate distinct dissociation products including dimer (D), tetramer (Q) and hexamers (H). Reprinted with permission from *Accounts of Chemical Research*, 47, 1010-1018. Copyright 2014, American Chemical Society. Further permissions related to the material excerpted should be directed to the ACS.

1.8.2. Surface-induced dissociation

Although CID provides structural information of protein complexes, it does not offer much insight on protein complexes substructure, and due to small size of target gas molecules, the amount of

energy deposited into large ions are not sufficient enough to dissociate large protein complexes. Another activation technique, surface-induced dissociation (SID) (53, 62) utilizes a much bigger mass target, a surface that imparts a lot more energy to gas phase ions compared to smaller target such as neutral gas molecules. Compared to CID that increases the internal energy of ions through multiple collisions, SID is a fast, single step that efficiently deposits a large amount of energy to gas phase ions overcoming the dissociation barrier (39) (Figure 1.8B). The symmetric charge dissociation pattern observed in SID experiments suggests of dissociation of folded sub-oligomers (Figure 1.8D) with minimal structural rearrangements which enables the release of native substructures of protein complexes to determine the topology of the complex.

1.9. Ion mobility spectrometry

Ion mobility spectrometry provides useful structural information of biomolecules ranging from small molecules (lipids, carbohydrates, peptides, nucleic acids, etc) to large protein complexes (63). An ion mobility device separates gas phase ions based on size, shape and charge analogous to electrophoresis in solution phase (64) (Figure 1.9A). IM coupled with MS (IM-MS) gives complementary information including mobility and m/z of gas phase ions. Different instrumentation of ion mobility spectrometry has been developed and used including drift-time ion mobility spectrometry (DTIMS) (65), traveling-wave ion mobility spectrometry (TWIMS) (66) and field-asymmetric ion mobility spectrometry (FAIMS) (67), with former two the most commonly used types of ion mobility spectrometry. In DTIMS, the oldest form of ion mobility spectrometry, ions are pulsed into a drift tube and driven by a weak electric filed in the direction of applied field (Figure 1.9B). The drift tube is also filled with an inert buffer gas such as helium or nitrogen and ions undergo interaction with the buffer gas. The time taken for ions to traverse

the tube differ based on their size and is proportional to rotationally-averaged collision cross section (CCS) of ions. As a result, smaller ions travel faster the drift tube compared to more extended ions due to different interaction with buffer gas. The measured drift time is used to calculate CCS using Mason-Schamp equation (68):

$$\Omega = \left(\frac{3ze}{16N_0}\right)\left(\frac{2\pi}{\mu k_B T}\right)^{\frac{1}{2}}\left(\frac{1}{K_0}\right) \quad \text{(eq. 1.1)}$$

Where z is the charge state of the ion, N is the density of the neutral gas, T is the temperature of the drift tube, k_B is Boltzmann constant, e is the elementary charge and K_0 is reduced mobility (mobility measured at standard pressure and temperature).

High resolving power (R>100) and direct CCS calculations are the advantages of DTIMS. Another type of IM spectrometry is TWIMS (66) (Fig 1.9C) that is built of stacked ring ion guides with opposite phases of Radio frequency (RF) voltages applied on each electrode leading to confine ions inside the IM chamber. Along with RF voltage, a direct current (DC) voltage is also applied on electrodes to propel ions axially. The applied DC voltage on adjacent electrodes creates a travelling wave in which gas phase ions 'surf' and cross the ion mobility cell. Smaller sized ions move along the travelling wave, while larger ions lag behind and roll over the wave and takes longer time to elute the IM cell. Adjustment of magnitude and velocity of travelling wave voltages leads to mobility separation of ions of different sizes. Direct CCS measurements in TWIMS are not applicable due to the constant changing of the voltages necessary to create a travelling wave. The calibrants with similar physical and chemical characteristics to analytes that have known CCS values measured by DTIMS are used to calculate the CCS of the analyte. In comparison to other structural biophysical techniques, IM-MS has multiple advantages including a small quantity of sample required for analysis, rapid gas phase separation and the size-independent analysis of

biomolecule of interest capable to study large protein complexes with molecular weight of 3 and 4 MDa. Lower purity of analytes can also be studied using IM-MS compared to X-ray crystallography and NMR owing to high selectivity of IM-MS to enable analysis of complex mixtures with similar mobilities or m/z information (69). Other applications of IM-MS include assessing the conformational changes of proteins upon ligand binding (70, 71) or post translational modifications, aggregation intermediates (72, 73), conformational dynamics (74, 75), CCS measurements, protein unfolding and topology (76).

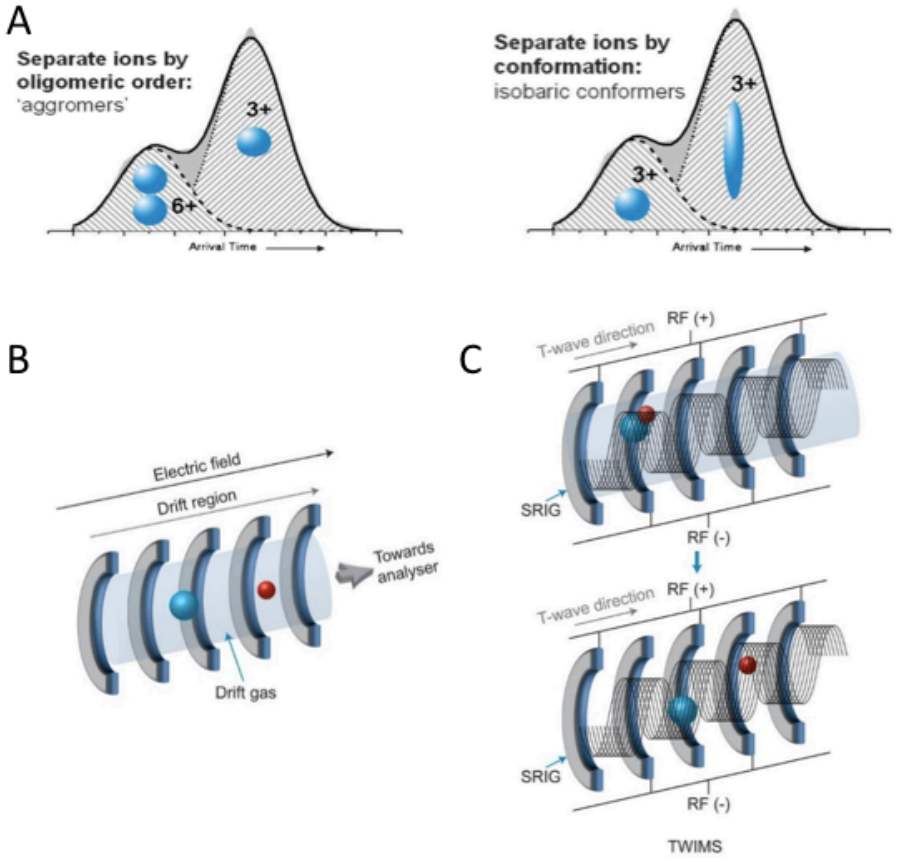

Figure 1.9. The schematics of frequently used IM devices. (A) IM has the ability to separate species with same m/z information including the aggromers and isobaric conformers. Representative diagram of (B) DTIMS and (C) TWIMS. Reprinted with permission from *Chemical Society Review*, 41, 4335-4355 and *Nature Chemistry*, 6, 281-294. Copyright 2014, Nature Publishing Group, a division of Macmillan Publishers Limited. All Rights Reserved.

1.10. Analyzing of large protein ions and protein complexes

Separation of gas phase ions with different m/z values is achieved by mass analyzers. There are different mass analyzers developed including ion-trapping instruments, Fourier transform ion cyclotron resonance (FTICR), Quadrupole, Orbitrap and time of flight (TOF) mass analyzers. The latter three mass analyzers are the most frequent ones to analyze large protein ions, and they will be discussed in detail below.

1.10.1. Quadrupole mass analyzers

A quadrupole mass analyzer consists of four cylindrical rods with radius r and an inscribed circle radius of r_0 (Figure 1.10A)

$$r_0 = r/1.145 \qquad \text{(eq. 1.2)}$$

with each opposing rods are connected to the same electric outlet (77) (Figure 1.10A). A combination of radio frequency (RF) voltage, V, and a DC voltage, U, is applied to the rods to pass through an ion with specific m/z value. If only DC voltages is applied to the rods, no ion will pass through because ions hit the rods with negative polarity and discharge. At RF-only mode ions with large window of masses will pass through, and hence a quadruple can be used as an ion guide. However, at a given U/V ratio, only ions that have a certain m/z value will pass through the rods due to stable trajectory, and other ions with unstable trajectory will discharge by colliding with rods (Figure 1.10B). Hence, quadrupoles can act as a "mass filter" only allowing ions with known m/z ratio. The maximum m/z analyzed by a quadrupole is shown by:

$$\left[\frac{m}{z}\right]_{max} = 7\times10^6\, V_m/(\upsilon^2 r_0^2) \qquad \text{(eq. 1.3)}$$

where r_0 is an inscribed radius between the rods, V_m is the magnitude of RF voltage and υ is the RF frequency (78). The maximum m/z resolved by quadrupole has a direct relationship with RF

voltage magnitude and an inverse relationship with r_0 and υ. Reducing the RF frequency would increase the capability of quadrupole to mass filter larger ions. However, decreasing RF frequency in a quadrupole mass analyzer leads to drop in resolution which can be improved by using tandem instruments. The advantages of quadrupole mass analyzers include fast operation, low cost and no requirement to operate at very high vacuum.

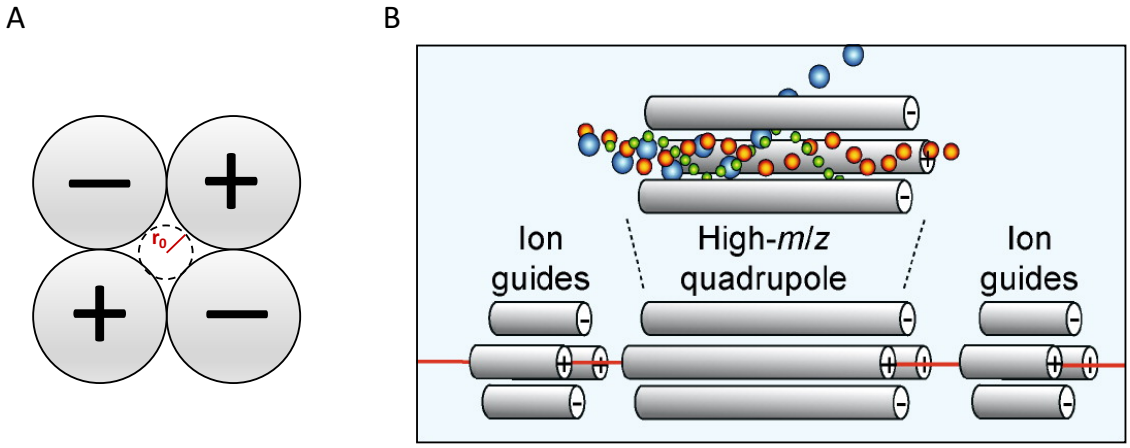

Figure 1.10. The cartoon representative of quadrupole mass analyzer. (A) schematic cut of four quadrupole rods. (B) A single ion with a specific m/z value pass through the rods and reach to the detector (Orange ions), while other ions with different m/z values (blue and green) have an unstable trajectory and collide with rods. Reprinted with permission from *Annual Review of Biochemistry*, 76, 167-189. Copyright 2007 by Annual Reviews. All rights reserved.

1.10.2. Time of flight mass analyzers (TOF)

TOF mass analyzers are routinely used to analyze ions of large protein complexes due to their inherent capability of unlimited mass range (79). The principle is to separate ions with different m/z ratios in a filed free tube under high vacuum. Each ion with a certain m/z value takes a different flight time (t) to traverse the tube with a distance d. If the acceleration voltage for an ion is Vs, the kinetic energy of the ion is given by (78):

$$\frac{mV^2}{2} = qV_S = zeV_S = E_K \qquad \text{(eq. 1.4)}$$

By replacing the time needed for an ion to travel the tube ($t = \frac{d}{V}$) and substitute for V in equation 1-4 gives:

$$t^2 = m/z(\frac{d^2}{2V_{se}}) \quad \text{(eq. 1.5)}$$

The derived formula shows that the square time of an ion to traverse the tube is proportional to its m/z value. A reflectron is embedded at the end of the tube to correct for kinetic energy dispersion of ions produced at the source. An ion with higher kinetic energy travels deeper into the reflectron and hence takes longer path to reach to the detector. On the other hand, another ion with smaller kinetic (same m/z value) energy penetrates less to the reflectron and experience a shorter path. Thus, both these ions with same m/z value but different energies arrive to the detector at the same time and detected accordingly by means of multichannel detectors (MCP). Quadrupoles has been usually implemented with TOF mass analyzers along with collision cell to perform tandem mass experiments. The arrangement of one of the prevalent types of tandem mass instruments, QTOF is shown in Figure 1.11. After generation of ions at source, a distinct ion with specific m/z value is selected via quadrupole and further activated in collision cell, and the products of activation are analyzed and detected by TOF mass analyzer and detector, respectively.

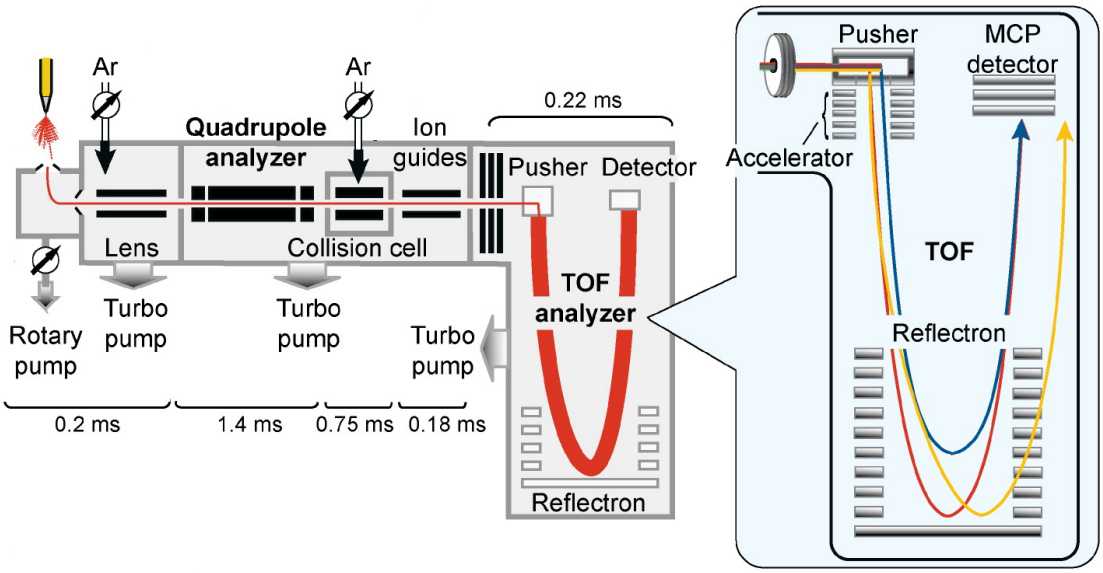

Figure 1.11. Schematic of a tandem Q-TOF mass spectrometer. A single ion with specific m/z value passes through a quadrupole and to a collision cell for further activation of an ion by colliding with a neutral gas buffer. Ions subsequently enter TOF analyzer where they are separated based on their time of flight. Ions with similar m/z value with different velocities reach the detector at the same time using a reflectron to correct their kinetic energy dispersion. In this case, the faster ion (red line) penetrates deeper into the reflectron and lag behind the slower ion (blue line) and hence detected by MCP at the same time. Reprinted with permission from *Annual Review of Biochemistry*, 76, 167-189. Copyright 2007 by Annual Reviews. All rights reserved.

1.10.3. Orbitrap mass analyzer

Since the introduction of orbitrap mass analyzers first at 1999 by Makarov (80), it extensively has been used to identify, characterize and quantify biological samples in both proteomics and assessing protein complexes in their native state due to its high resolution and accuracy. The immediate advantages of Orbitrap compared to TOF and FT-ICR mass analyzers are higher resolving power and no need for superconducting magnets, respectively. The cut-out of an Orbitrap analyzer is shown in figure 1.12A. It consists of a central spindle like electrode and two outer electrodes (81). The ions injected into the Orbitrap in pulse from an external ion storage device called C-trap and start to oscillate around the central electrode by applying voltage on the

central and outer electrodes creating an electrostatic field. The harmonic oscillation of ions will then be detected by outer electrodes by means of image current. Ions with different m/z ratio experience a different oscillation frequency which is the principle of ion separation in Orbitrap mass analyzers. A Fourier transform analysis is then performed to convert the digitized image current in time domain to frequency domain that results in determination of accurate masses of different ions.

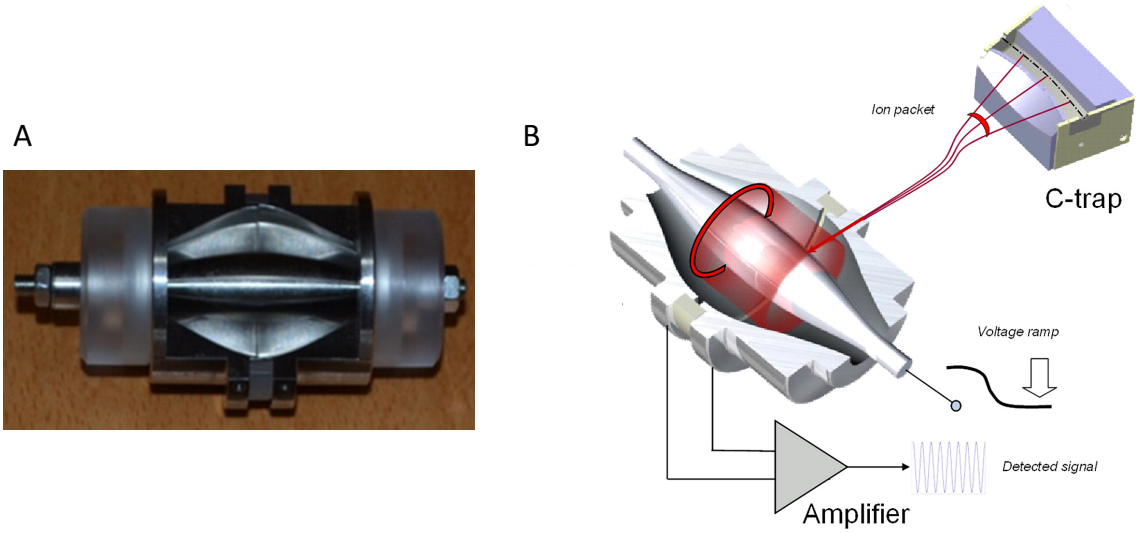

Figure 1.12. The schematics of an Orbitrap mass analyzer. (A) The cross-section of an Orbitrap device shows the central and outer electrodes. (B) Ions with same kinetic energy are pulsed as a packet into the Orbitrap where they harmonically oscillate around the central electrode and are separated based on their m/z values. Reprinted with permission from *Analytical Chemistry*, 85, 5288-5296. Copyright 2013, American Chemical Society.

2. INTRINSIC GTPASE ACTIVITY OF KRAS MONITORED BY NATIVE MASS SPECTROMETRY [*]

2.1. Introduction

RAS proteins regulate diverse cellular processes, including cell proliferation, apoptosis, differentiation, migration, and cell growth.(6, 82-86) RAS proteins function as a molecular switch cycling between inactive guanosine diphosphate (GDP) and active guanosine triphosphate (GTP) bound states.(87-90) Conformational changes in three main regions of RAS is associated with the exchange of bound GDP for GTP: switch I (residues 30-38), switch II (residues 59-76) and P-loop (residues 10-17).(3) In the active state, RAS binds and activates downstream effectors (RAF kinase, PI3K, and Ral guanine nucleotide dissociation stimulator).(3) RAS proteins possess low intrinsic GTP hydrolysis and guanidine nucleotide exchange rates.(91, 92) These attributes are regulated by guanine nucleotide exchange factors (GEFs), which accelerate the exchange of GDP for GTP, and GTPase-activating proteins (GAPs), which stimulate the hydrolysis of GTP leading to deactivation of the active state.(93)

The first mutated genes in human cancers were discovered nearly four decades ago that mapped to activating mutations in RAS genes.(94, 95) To date, the three RAS proteins (H-RAS, KRAS, and N-RAS) have high overall sequence identity and are the most commonly mutated of all discovered oncogenes with 30% of human cancers containing RAS mutations.(92, 96, 97)

---

[*] Reprinted with permission from Moghadamchargari, Z.; Huddleston, J.; Shirzadeh, M.; Zheng, X.; Clemmer, D.; Raushel, F. M.; Russell, D. H.; and Laganowsky, A. Intrinsic GTPase Activity of K-RAS Monitored by Native Mass Spectrometry. *Biochemistry,* **2019***,* 58, 3396-3405. Copyright (2019) by American Chemical Society

Nearly all oncogenic RAS genes contain mutations that map to residues G12, G13 and Q61, which often impairs the intrinsic and GAP-stimulated GTP hydrolysis leading to unregulated cell signaling and tumor growth.(21, 92, 98-100) More specifically, KRAS is the most frequently mutated isoform which has a high frequency in pancreatic cancer (70-90%), colon cancer (30-50%), and lung cancer (20-30%).(7, 101, 102) KRAS oncogenic mutants exhibit differences in the biological behavior of tumors, and understanding the intrinsic biochemical and structural properties of oncogenic mutants can potentially accelerate the development of therapeutics.(103-105)

The kinetics of GTP hydrolysis for RAS proteins has been extensively studied by an arsenal of biochemical and biophysical methods, such as nuclear magnetic resonance (NMR), Fourier transform infrared spectroscopy (FTIR), radiolabeled substrates, and spectroscopic assays wherein the amount of phosphate released by enzymatic hydrolysis is monitored.(21, 106-108) RAS proteins are able to switch to an inactive state either through intrinsic hydrolysis or interacting with GAPs which accelerate the hydrolysis rate by 10^5.(109) Previous studies have shown RAS has a slow intrinsic hydrolysis rate and oncogenic mutations display an even slower rate of GTP hydrolysis that essentially locks RAS in an active state. The energetics of intrinsic GTP hydrolysis determined for H-RAS suggests that the enthalpic effect is the dominant barrier of the transition state.(110)

Native mass spectrometry (MS) is an emerging biophysical technique to study protein structure and function (111, 112). In native MS, protein complexes in a volatile, non-denaturing solution (typically ammonium acetate) are ionized using nano-electrospray ionization(78, 113) and the instrument tuned to preserve protein structure and noncovalent interactions in the mass spectrometer.(114-116) This unique ability has enabled the analysis of direct ligand binding,

protein dynamics and topology, subunit stoichiometry, and measurement of thermodynamics and binding affinities.(41, 117-120) More recently, high-resolution native mass spectrometry is able to characterize the binding of small molecules such as drugs, nucleotides, lipids, metals and small enzyme cofactors.(118, 121, 122) Ion mobility (IM) is a gas phase electrophoretic separation of molecules based on the size and shape of ions, and when it is combined with MS it can provide structural information by measuring the rotationally averaged collision cross section (CCS). Native IM-MS can monitor direct molecular interactions of molecules with protein complexes and also provide unparalleled insight into the purity of protein samples.(113, 123)

Here, we use high-resolution native MS to directly measure the kinetics and energetics of intrinsic GTP hydrolysis of KRAS and oncogenic mutants: G12C, G13D, and Q61H. The "as isolated" mass spectra of KRAS and mutants reveal heterogeneity of the enzyme where both 2'-deoxy and 2'-hydroxy forms of GDP and GTP are bound. Hydrolysis of GTP to GDP and inorganic phosphate was monitored directly by the decrease in m/z of the intact ion from KRAS•GTP to KRAS•GDP. The intrinsic hydrolysis rates determined by native MS are in direct agreement with a spectroscopic assay that measures the concentration of inorganic phosphate. The hydrolysis rate of 2'-deoxy GTP (dGTP) was also monitored using mass spectrometry, and results show that three oncogenic mutants, Q61H, G13D and G12C, have a higher dGTP hydrolysis rate compared to that for GTP. The energetics of hydrolysis for KRAS and oncogenic mutants reveal the transition state is both enthalpically and entropically unfavorable, with enthalpic term being the largest barrier in the hydrolysis of GTP. Taken together, our results emphasize the utility of native high-resolution MS to study kinetic and thermodynamic properties of KRAS, including other GTPases, and uncover heterogeneity of nucleotides bound to KRAS that might be unrecognized using other biophysical techniques.

2.2. Materials and methods

2.2.1. Protein expression and purification

The KRAS4B (residues 1-170, UniProt P01116-2) plasmid for expression in *E. coli* was a kind gift from Dr. Kenneth D. Westover (University of Texas Southwestern Medical Center). The KRAS4B (referred here as KRAS) construct included an N-terminal TEV protease cleavable His_6 tag. All mutations were generated using Q5 site directed mutagenesis kit (New England Biolabs) following the manufacturer's protocol. Plasmids were transformed into Lemo21(DE3) *E. coli* (New England Biolabs) for protein expression. Several colonies were grown overnight at 37 °C in Luria broth (LB) supplemented with 50 μg/mL kanamycin. One liter of LB was inoculated with overnight culture and grown at 37 °C to OD (600 nm) 0.8. Protein expression was induced by addition of isopropyl β-D-1-thiogalactopyranoside (IPTG) to a final concentration of 500 μM IPTG and grown overnight at 18 °C. Cells were harvested by centrifugation at 5000*g* and cell pellets stored at -80 °C. Cell pellets were thawed at room temperature and resuspended in resuspension buffer (500 mM sodium chloride and 20 mM 2-amino-2-(hydroxymethyl)-1,3-propanediol (TRIS) pH 7.4 at room temperature) supplemented with a complete protease inhibitor tablet (Roche) and 5 mM β-mercaptoethanol (β-ME). The cell suspension was passed three times through a microfluidizer (Microfluidics M-110P) at 20,000 psi. The lysate was clarified by centrifugation at 30000*g* for 30 min and imidazole was added to a final concentration of 20 mM. The lysate was filtered using 0.45 μm syringe filter prior to loading onto a 5 mL HisTrap HP column (GE Healthcare) pre-equilibrated in buffer A (300 mM NaCl, 20 mM imidazole, 5 mM β-ME, 20% glycerol, and 20 mM TRIS pH 7.4 at room temperature). The protein was eluted with buffer A containing 500 mM imidazole. The peak fractions were pooled and desalted using HiPrep 26/10 desalting column (GE Healthcare) equilibrated in buffer A. The desalted protein was then

digested with TEV protease at 4 °C overnight to remove the N-terminal purification tag. The sample was passed over 5 mL HisTrap HP column and flow through containing tag-less protein was collected. The sample was further diluted (six times) and loaded onto a 5 mL HiTrap Q HP column (GE healthcare) equilibrated with buffer B (50 mM sodium chloride, and 20 mM TRIS pH 8 at room temperature) and eluted with a linear gradient to 100% buffer C (1 M sodium chloride, 20 mM TRIS pH 8 at room temperature) over five column volumes. The peak fractions containing protein were pooled, concentrated, and injected onto a Highload 16/600 Superdex 75 pg column (GE Healthcare) equilibrated in buffer D (150 mM sodium chloride, 5 mM β-ME, 20% glycerol, 20 mM 4-(2-hydroxyethyl)-1-piperazineethanesulfonic acid (HEPES) adjusted to pH 7.4). Peak fractions containing protein were pooled, concentrated using centrifugal concentrator (Millipore, 10k MWCO), flash frozen with liquid nitrogen and stored in -80 °C.

2.2.2. Determination of protein concentration

The protein concentration was determined using a UV-Vis spectrometer (Biospectrometer eppendorf) at 280 nm using an extinction coefficient of 11920 $M^{-1}cm^{-1}$.

2.2.3. Nucleotide exchange assay

KRAS and oncogenic mutants at a concentration of 100 μM were incubated in buffer D supplemented with 10 mM ethylenediaminetetraacetic acid (EDTA) and either 2 mM GTP (guanosine 5'-triphosphate, Sigma Aldrich) or dGTP (2'-deoxyguanosine 5'-triphosphate, Sigma Aldrich) for 2 hours at 4 °C. The nucleotide exchange reaction was then supplemented with 10 mM magnesium chloride and incubated for another hour at 4 °C. Excess nucleotide was removed using centrifugal buffer exchange device (Micro Bio-Spin 6 Column, Bio-Rad). To fully exchange GDP with GTP, this procedure was repeated one more time. The nucleotide exchanged sample was then supplemented with either GTP or dGTP at a final concentration of 2 mM, added to a

Slide-A-Lyzer MINI device (MWCO 2000 Da, Thermo), and dialyzed against 200 mM ammonium acetate overnight at 4 °C.

2.2.4. Native mass spectrometry

The protein loaded with either GTP or dGTP was buffer exchanged using Micro Bio-Spin 6 device into 200 mM ammonium acetate at pH 7.4 (pH was adjusted with ammonium hydroxide) and incubated at 25 °C. To monitor hydrolysis, samples were loaded into pulled borosilicate glass capillaries prepared in-house(124) and electrosprayed with voltage applied through a platinum wire inserted directly into the solution. Samples were introduced into Thermo Exactive Plus with extended mass range Orbitrap mass spectrometer. The mole fraction of GDP bound KRAS ($F_{KRAS•GDP}$) at different time points were deconvoluted using Unidec (125) and calculated as follows:

$$F_{K-RAS•GDP} = \frac{\sum_{i=0}^{3} K-RAS•GDP•A_i}{\sum_{i=0}^{3} K-RAS•GDP•A_i + \sum_{i=0}^{3} K-RAS•GTP•A_i} \quad \text{(eq. 2.1)}$$

Where *i* represents the number of the adducts (A) bound to KRAS. Mole fraction was converted to concentration:

$$[K - RAS \bullet GDP]_{total} = P_{total} \times F_{K-RAS•GDP} \quad \text{(eq. 2.2)}$$

and P_{total} is the total concentration of the enzyme. The mole fraction and concentration of KRAS bound GTP was calculated in a similar fashion. In order to obtain thermodynamic parameters for GTP hydrolysis, loaded proteins were incubated at four different temperatures: 10, 25, 30 and 37 °C. Instrument parameters (Table 2.1) were tuned to minimize gas phase activation and to preserve noncovalent interactions.

Table 2.1. The optimized parameters used for quantitative analysis of intrinsic hydrolysis using Q Exactive EMR.

m/z range	2000-3000
Resolution	140000
In-source collision energy dissociation (V)	10
Source temperature (°C)	100
Capillary voltage (KV)	1.6
Source DC offset (V)	25
Injection flatapole lens(V)	15
Inter flatapole DC (V)	10
Bent flatapole DC (V)	6
Transfer multipole DC (V)	2
Pressure (mbar)	3.4×10^{-10}

2.2.5. Native ion mobility mass spectrometry

KRAS and mutants were fully loaded with GTP and analyzed using an Agilent 6560 ion mobility Q-TOF mass spectrometer (Agilent Technologies, Santa Clara).(126) For native ion mobility mass spectrometry (IM-MS) measurements, ions were generated from a nanoelectrospray ionization source. Ions were then pulsed into the drift tube filled with ~3.95 torr of nitrogen gas, where they travelled under the influence of a weak electric field (5 V/cm.Torr). Ions exiting the drift tube were refocused by a rear ion funnel prior to QTOF MS detection and their arrival times (t_A) recorded. CCS values were determined from first principles with data acquired at different drift voltages.(127) Instrumental settings are given in the Supplemental Information (Table 2.2 and 2.3). The Agilent IM-MS Browser software was utilized to extract arrival time distributions (ATD), IMS data processing and all stepped field CCS calculations.

Table 2.2. NanoESI condition and front funnel settings for the 20,000 m/z extended mass range ion mode (Agilent 6560).

Capillary voltage (V)	1000-2000
Drying gas temperature (°C)	200
Drying gas flow (L/min)	1.5
Fragmentor (V)	400
High Pressure funnel delta (V)	150
High Pressure Funnel RF (V)	200
Trap funnel delta (V)	180
Trap funnel RF (V)	200
Trap Funnel Exit (V)	10

Table 2.3. Drift Tube Settings for Stepped Field Experiments in Positive Ion Mode

Time Sequence	Time (min)	Drift Tube Entrance (V)	Drift Tube Exit (V)	Rear Funnel Entrance (V)	Rear Funnel Exit (V)
1	0.0 – 0.5	1074	224	217.5	45
2	0.5 – 1.0	1174	224	217.5	45
3	1.0 – 1.5	1274	224	217.5	45
4	1.5 – 2.0	1374	224	217.5	45
5	2.0 – 2.5	1474	224	217.5	45
6	2.5 – 3.0	1574	224	217.5	45
7	3.0 – 3.5	1674	224	217.5	45

2.2.6. Malachite green assay

The intrinsic hydrolysis of KRAS was monitored using a malachite green assay.(128) In brief, malachite green reagent (1 mg/mL malachite green, 100 mg/mL ammonium molybdate and 0.01% Triton X-100 in 50 mL of 1 M hydrochloric acid) was prepared as described.(129) A standard curve was generated by serial dilutions of 1 mM dipotassium phosphate. The concentration of inorganic phosphate released during hydrolysis was determined at different time intervals for KRAS loaded with GTP. For each time point, 30 μL of malachite green reagent was added to 10 μL of 10 μM KRAS and incubated for 15 minutes. The absorbance was measured at 650 nm using a Synergy (MX) plate reader. All measurements were done in triplicates and solutions were made using OmniTrace Ultra water (Sigma Aldrich) to minimize background phosphate.

2.2.7. Analysis of intrinsic GTPase data

Kintek Explorer (version 7.6) was used to globally fit the kinetic data to a first order rate constant as follows:

$$K - RAS \bullet GTP \xrightarrow{k_{hyd}} K - RAS \bullet GDP + P_i \qquad \text{(eq. 2.3)}$$

And the integrated form:

$$[K - RAS \bullet GTP] = [K - RAS \bullet GTP]_0 e^{-k_{hyd}t} \qquad \text{(eq.2.4)}$$

The rate of the reverse reaction was assumed to be negligible. In order to obtain the energetics of intrinsic hydrolysis, the temperature dependence of rate constants was analyzed using the Eyring(130) equation:

$$k_{hyd} = \frac{k_B T}{h} e^{(-\frac{\Delta H^{\ddagger}}{RT} + \frac{\Delta S^{\ddagger}}{R})} \qquad \text{(eq. 2.5)}$$

Where k_{hyd} is the intrinsic hydrolysis rate constant, h is Plank's constant, k_B is Boltzman constant, R is gas constant, $\Delta H^{\ddagger}$ is the enthalpy of activation, and $\Delta S^{\ddagger}$ is the entropy of activation. To calculate $\Delta H^{\ddagger}$ and $\Delta S^{\ddagger}$, the linearized form of the Eyring equation was used:

$$\ln\frac{k_{hyd}}{T} = \frac{-\Delta H^{\ddagger}}{RT} + \frac{\Delta S^{\ddagger}}{R} + \ln\frac{k_B}{T} \qquad \text{(eq. 2.6)}$$

The natural log of k_{hyd}/T was plotted as a function of 1/T. $\Delta H^{\ddagger}$ and $\Delta S^{\ddagger}$ parameters were calculated from slope and intercept of this plot as follow:

$$\Delta H^{\ddagger} = -slope \times R \qquad \text{(eq. 2.7)}$$

$$\Delta S^{\ddagger} = \left(Intercept - \ln\frac{k_B}{T}\right) \times R \qquad \text{(eq. 2.8)}$$

2.3. Results

2.3.1. Heterogeneity of "as isolated" KRAS and oncogenic mutants

Previous work suggest that native MS can accurately reflect the solution binding properties of small molecules with proteins.(41, 117-120) Therefore, we recorded native mass spectra of purified protein samples on an orbitrap mass spectrometer tuned to preserve noncovalent interactions (Figure 2.1A).(121)

After deconvolution of native mass spectra,(125) a number of molecular species were observed for the "as isolated" proteins (Figure 2.1B, Table 2.4). For KRAS, the most intense signal has a molecular weight in agreement with KRAS bound to GDP (guanosine 5'-diphosphate), a hydrolysis product (Figure 2.1B).

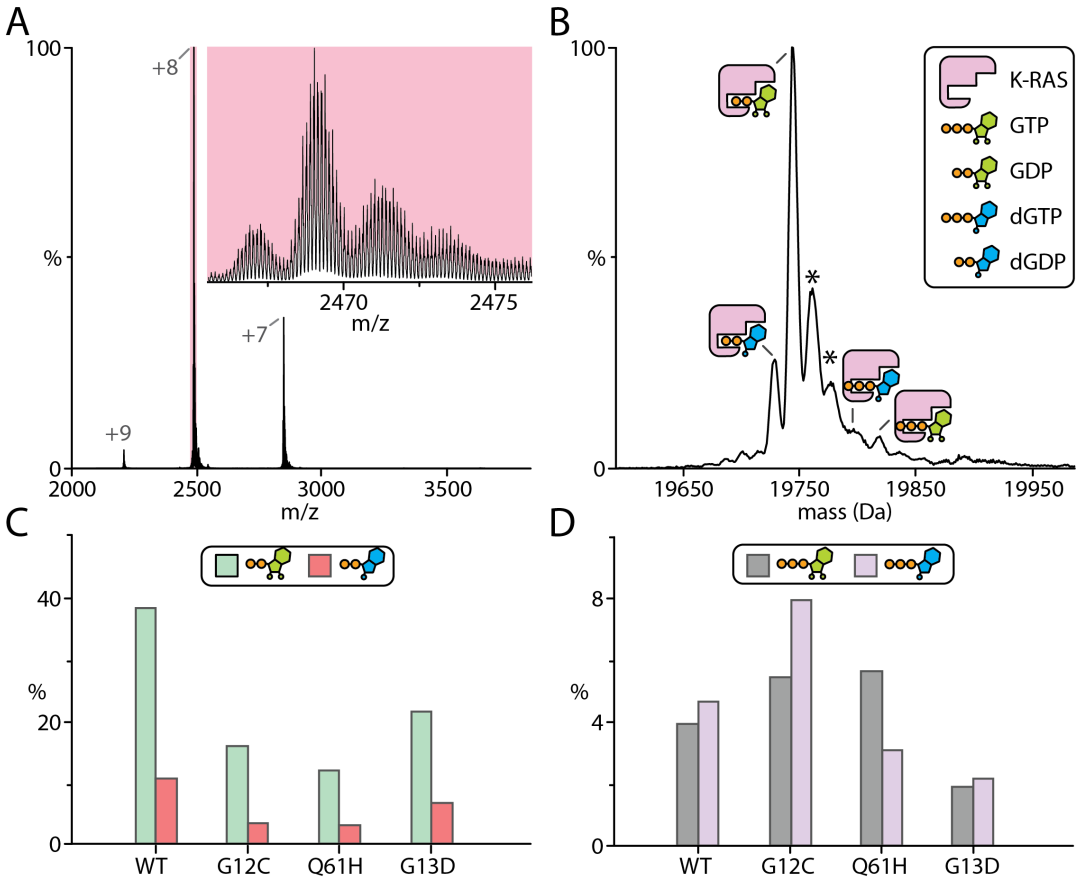

Figure 2.1. Native mass spectrometry reveals heterogeneity of "as isolated" KRAS and mutants. (A) Native mass spectrum of 2 μM KRAS in 200 mM ammonium acetate, pH 7.4. The inset is an expansion of the isotopically resolved 8+ charge state of KRAS bound to GDP (B) Deconvolution of the mass spectrum shown in (A) using UniDec.(125) The different nucleotide bound states of KRAS are labeled. Asterisk represents sodium and/or magnesium bound adducts. (C and D) Mole fraction of KRAS and mutants bound to the 2'-deoxy and 2'-hydroxy forms of (C) GDP and (D) GTP.

Interestingly, a mass that is 16 Da lighter is also measured, which corresponds to KRAS bound to 2'-deoxyguanosine 5'-diphosphate (dGDP). Although at lower abundance, signal is present for the molecular weights of KRAS bound to dGTP (2'-deoxyguanosine 5'-triphosphate) and GTP (guanosine 5'-triphosphate). Native mass spectra for oncogenic mutants acquired with the same instrument settings also show binding of dGDP, GDP, GTP and dGTP (Figure 2.2, Table 2.4). However, a peak with molecular weight heavier than the mass of GTP is also observed for

$KRAS^{G13D}$ (Figure 2.2B). In addition, adducts, such as sodium and magnesium, are bound to KRAS and mutants (Figure 2.2D). There are also considerable differences in the mole fraction of dGDP, GDP, dGTP, and GTP bound to KRAS and oncogenic mutants (Figure 2.1C and D). For example, the WT protein has an almost equal abundance of dGTP and GTP bound whereas $KRAS^{Q61H}$ and $KRAS^{G12C}$ were bound to a larger fraction of GTP and dGTP, respectively. These results illustrate the ability of native MS to provide insight into sample heterogeneity and also suggest that each oncogenic mutant may have different affinities towards the 2'-deoxy versus 2'-hydroxy forms of guanosine nucleotides.

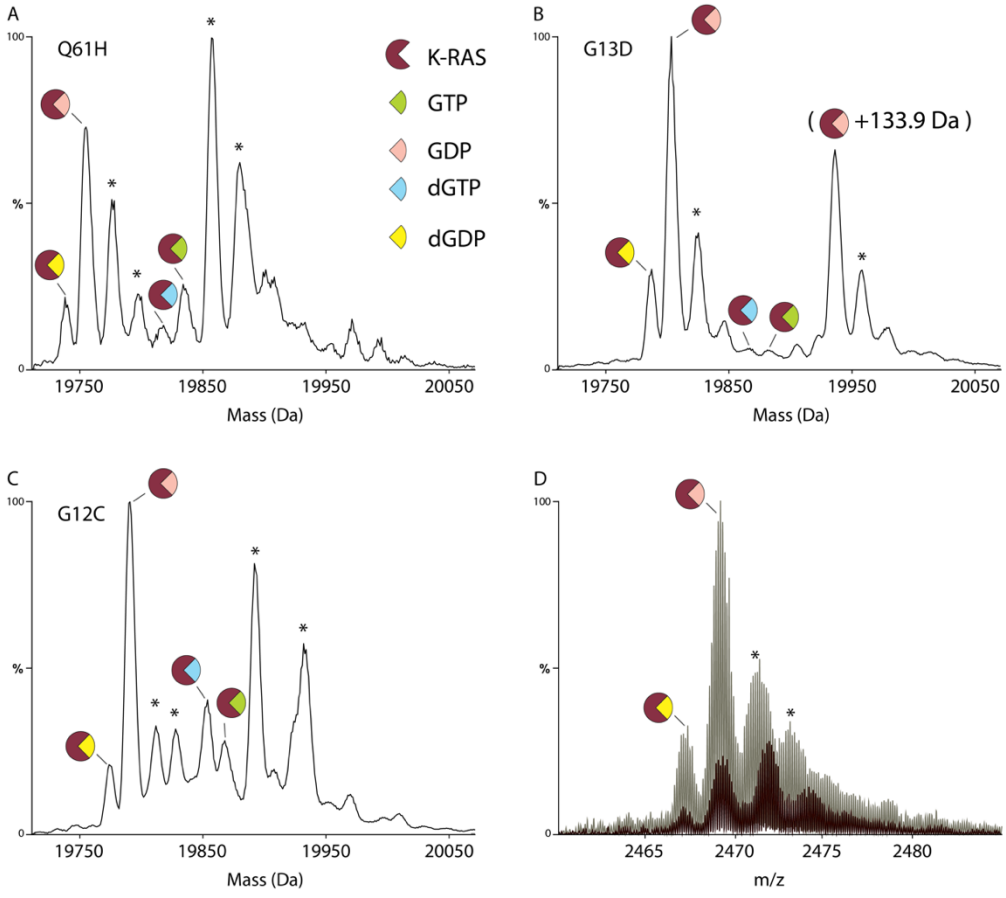

Figure 2.2. Deconvolution of native mass spectra for oncogenic KRAS mutants (A) Q61H, (B) G13D and (C) G12C reveal binding of 2'-deoxy and 2'-hydroxy forms of GDP and GTP. (D) Overlay of native mass spectra of KRAS (8+) as isolated (gray) and with magnesium acetate added to the spray solution (maroon). Asterisk denotes bound sodium or magnesium adducts.

Table 2.4. Theoretical and measured monoisotopic masses for 2'-deoxy and 2'-hydroxy forms of GDP and GTP bound to KRAS WT and mutants. The measured monoisotopic mass is calculated by deconvolution the native mass spectra using Thermo protein deconvolution software.

Protein	Species	Measured monoisotopic mass (Da)	Theoretical monoisotopic mass (Da)	Average mass (Da)	ppm
WT	dGDP	19717.69	19717.67	19729.12	0.938
	GDP	19733.71	19733.67	19745.04	2.11
	dGTP	19796.60	19796.63	19797.92	1.58
	GTP	19810.56	19812.63	19820.96	104.57
G12C	dGDP	19762.93	19763.64	19775.04	35.86
	GDP	19778.96	19779.64	19791.04	34.40
	dGTP	19841.87	19842.60	19853.92	37.09
	GTP	19855.88	19858.60	19868.00	137.31
G13D	dGDP	19775.69	19776.68	19786.72	50.04
	GDP	19791.71	19792.68	19803.68	48.95
	dGTP	19854.61	19855.64	19865.60	51.98
	GTP	19873.57	19871.64	19881.60	97.42
Q61H	dGDP	19726.60	19727.67	19737.68	54.44
	GDP	19742.63	19743.67	19753.68	52.63
	dGTP	19805.56	19806.63	19817.68	54.27
	GTP	19821.58	19822.63	19834.64	53.12

2.3.2. Collision cross section measurements of KRAS and oncogenic mutants bound to GTP

In order to structurally compare the active state of KRAS with oncogenic mutants, KRAS proteins loaded with GTP were analyzed by ion mobility mass spectrometry. The native mass spectra show that the proteins are predominantly bound to GTP and adducts with a molecular weight consistent with sodium or magnesium (Figure 2.3 and 2.4).

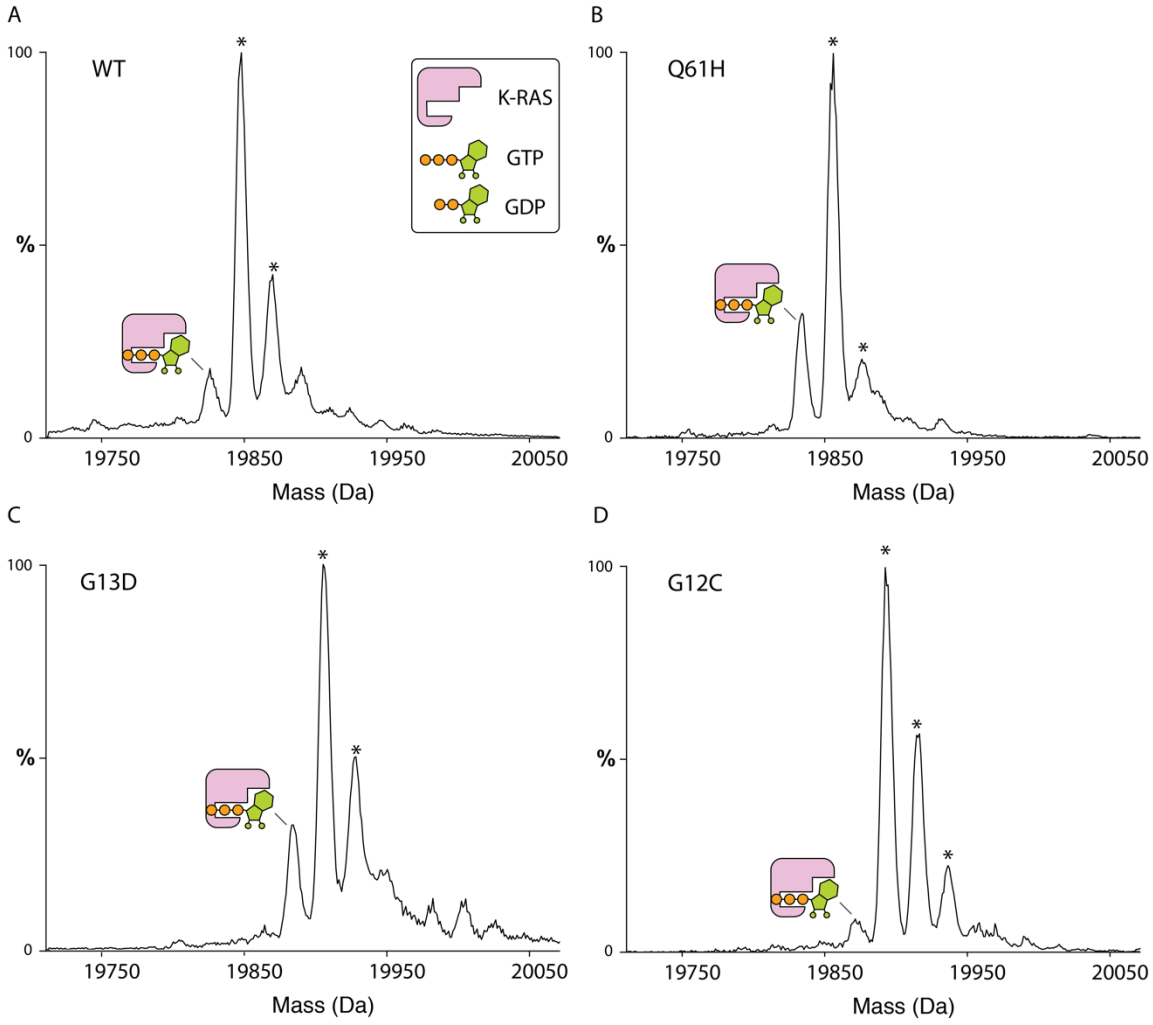

Figure 2.3. Deconvolution of native mass spectra for KRAS (A) WT, (B) Q61H, (C) G13D and (D) G12C loaded with GTP. Asterisk represents bound sodium or magnesium adducts.

KRAS•GTP bound to a single magnesium is the most abundant species for the GTP bound enzyme. The previously bound adducts in the "as isolated" samples are completely removed. The rotationally averaged collision cross section (CCS) of KRAS and mutants were measured using an ion mobility mass spectrometer.

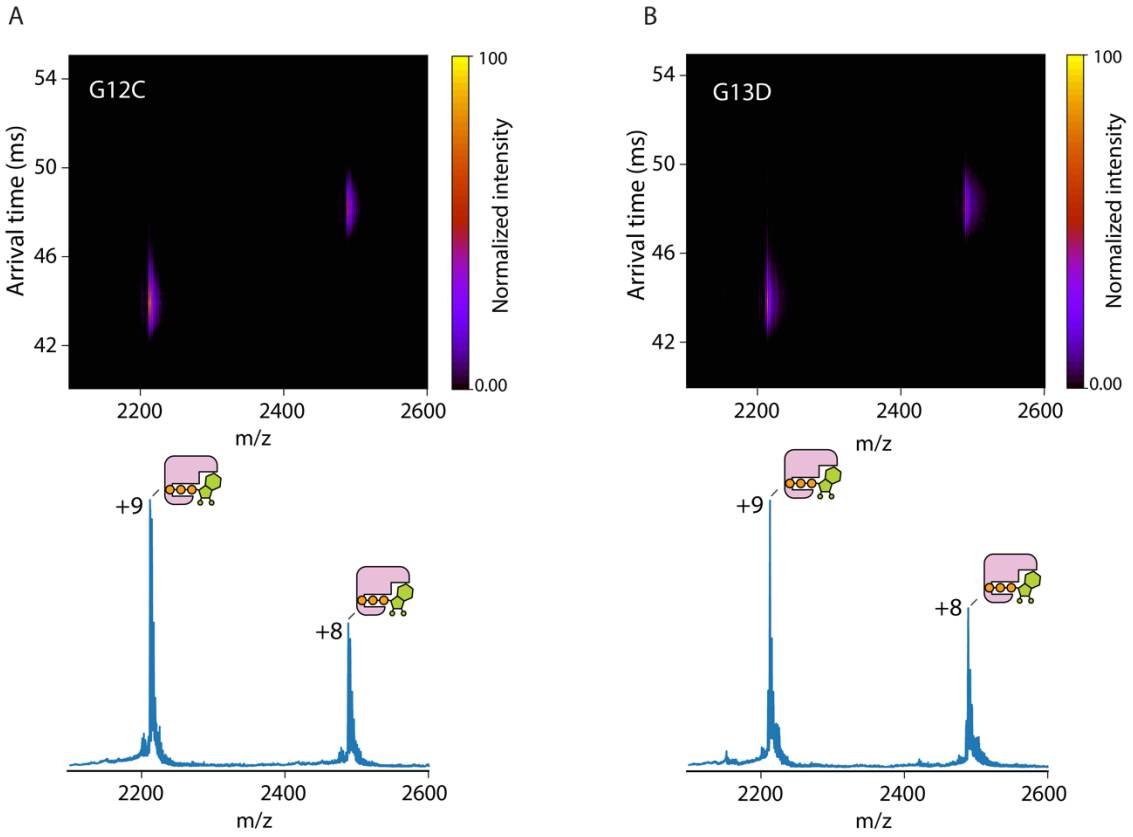

Figure 2.4. 2D Ion mobility mass spectra of KRAS (A) G12C and (B) G13D. All mutants were loaded with GTP.

Figure 2.5 shows the mass spectrum of KRAS and its representative ion mobility mass spectrum. The ion mobility mass spectra for G13D and G12C and arrival time distributions (ATD) for KRAS•GTP and mutants are shown in supporting information (Figure 2.3 and 2.6).

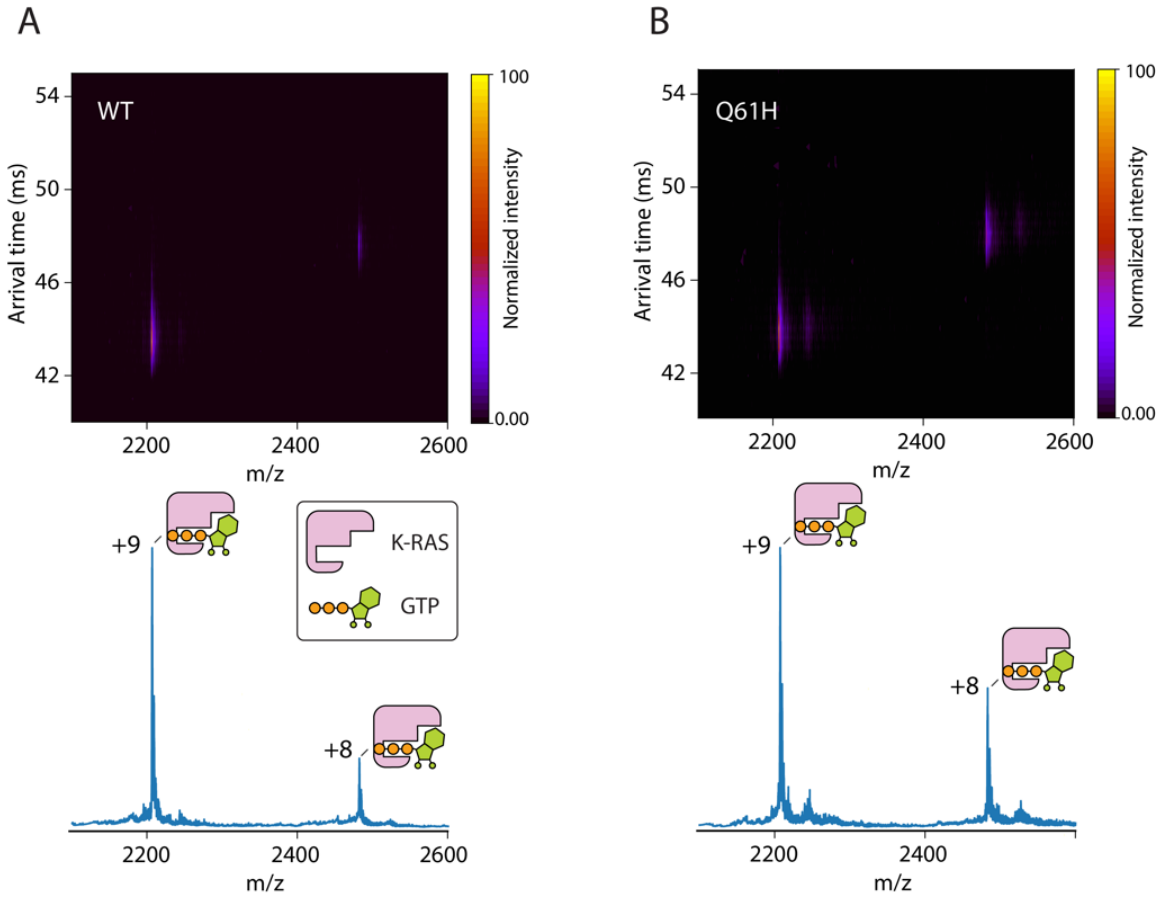

Figure 2.5 Ion mobility mass spectra of KRAS and Q61H mutant. (A) KRAS and (B) $KRAS^{Q61H}$ loaded with GTP. The mass spectrum is shown at the bottom.

The CCS values for KRAS and mutants bound to GTP are largely similar with the exception of $KRAS^{Q61H}$ (Figure 2.5B), which has smaller CCS implying that protein complex is more compact (Table 2.5).

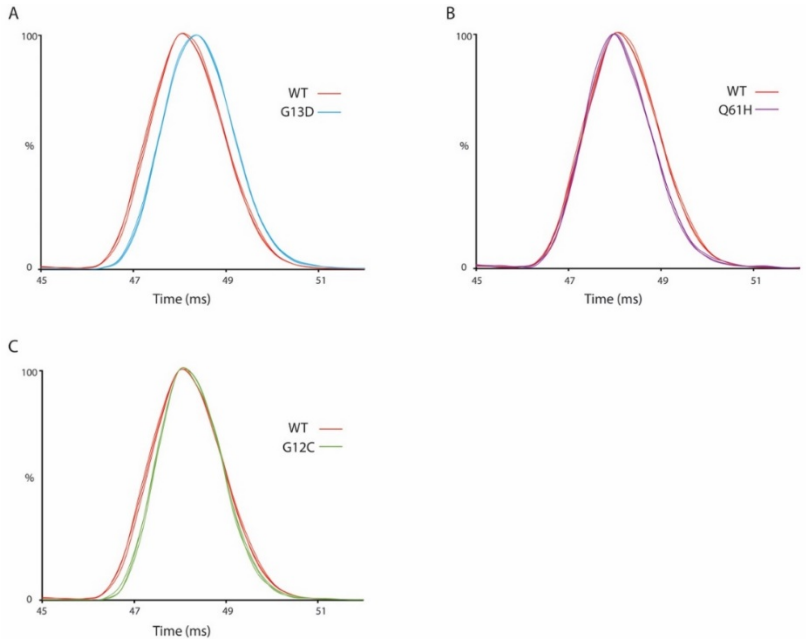

Figure 2.6. Comparison of arrival time distributions (ATD) of KRAS and mutants bound to GTP. ATD are shown for the 8^{+} charge state and repeated measurements overlaid.

Table 2.5. Collision cross section (CCS) values for the 8+ charge state of KRAS and mutants bound to GTP. Reported are the mean and standard deviation for the centroid CCS values (n = 3).

Protein	CCS (Å^2)
KRAS	1932.3 ± 1.1
$KRAS^{G12C}$	1937.7 ± 2.8
$KRAS^{G13D}$	1939.5 ± 1.3
$KRAS^{Q61H}$	1921.7 ± 2.9

2.3.3. Intrinsic GTPase activity of KRAS and mutants

To monitor the intrinsic GTPase activity, the molecular weight of KRAS and oncogenic mutants loaded with GTP were monitored over time using native mass spectrometry (Figure 2.7). At the start of the reaction the proteins are predominantly loaded with GTP (Figure 2.7A and 2.3). A number of adducts consistent with the molecular weight of magnesium or sodium are present and

these adducts were accounted for when deconvoluting mass spectra. After 360 minutes of incubation at 25 °C, the hydrolysis of GTP to GDP and inorganic phosphate by KRAS is evident by loss in mass from KRAS•GTP giving rise to a signal for KRAS bound to GDP (Figure 2.7A). The theoretical monoisotopic mass for HPO_3^- (80.0 Da) and the observed measured difference in mass as a result of hydrolysis is 80.9 Da. Notably, the loss in mass in the KRAS•GTP corresponds to HPO_3^- but this leaves the enzyme as inorganic phosphate (PO_4^{2-}). The hydrolysis of GTP nearly reaches completion after 1,260 minutes and the predominate signal is for KRAS bound to GDP. The concentration of KRAS bound to GDP and GTP, including the species adducted with magnesium or sodium, were determined from deconvolution of mass spectra data and fit to a first order rate constant model using KinTek Explorer Software(131, 132) to determine the intrinsic rate of GTP hydrolysis ($k_{hyd,GTP}$) (Figure 2.7B). Figure 2.7B shows the fit of this model to the data. The $k_{hyd,GTP}$ for KRAS at 25 °C in 200 mM ammonium acetate (pH 7.4) is 2.42 x 10^{-3} per minute.

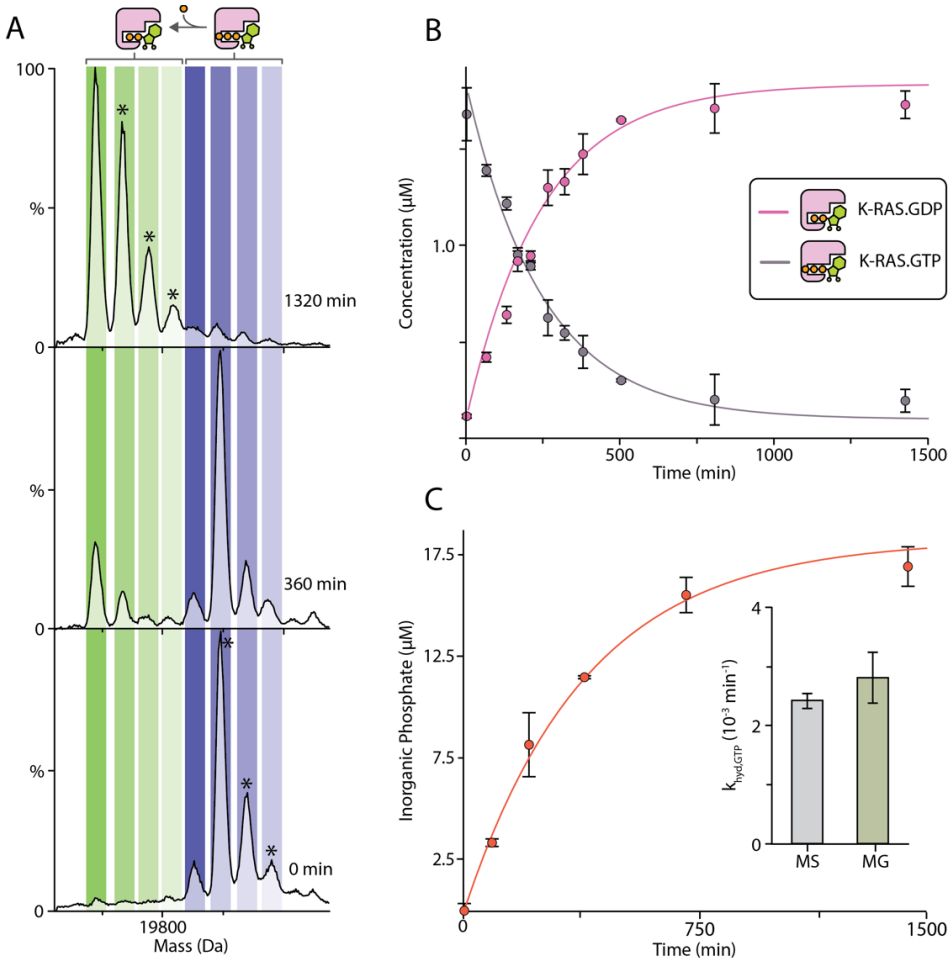

Figure 2.7. Determination of GTP hydrolysis rate ($k_{hyd,GTP}$) for KRAS. (A) Representative native mass spectra recorded at different time points for KRAS (2 μM) loaded with GTP incubated at 25 °C. The abundance of KRAS bound to GDP increases as GTP is hydrolyzed. Asterisk denotes species with bound sodium or magnesium adducts. (B) The concentration of KRAS bound to GDP and GTP was determined from deconvolution of native MS data (dots) and fit to first order rate constant model (solid lines) using KinTek Explorer Software.(131, 132) (C) Plot of inorganic phosphate concentration determined for KRAS•GTP (20 μM) using a malachite green assay as a function of time (dots) and fit to a first order rate constant model (solid lines). The inset shows the rate constants determined by native MS and malachite green (MG) assay, which are statistically similar (student's t-test, two tail, $p = 0.29$). Reported are the mean and standard deviation ($n = 3$).

To validate the $k_{hyd,GTP}$ value determined by native MS, an established solution assay was used to monitor the intrinsic GTPase activity of KRAS.(133, 134) The concentration of inorganic phosphate was quantified over time for KRAS loaded with GTP at 25 °C and $k_{hyd,GTP}$ was determined as done for the native MS data (Figure 2.7C). The $k_{hyd,GTP}$ determined from the two

techniques are statistically indistinguishable. These results corroborate the native MS derived values and indicate that GDP remains bound to KRAS after inorganic phosphate is released.

In a similar fashion to the wild-type protein, the intrinsic GTPase activity of KRAS oncogenic mutants was determined by native MS. Again, the hydrolysis of GTP by KRAS mutants is monitored directly by the appearance and decrease of signals corresponding to the protein bound to GDP and GTP, respectively (Figure 2.8A).

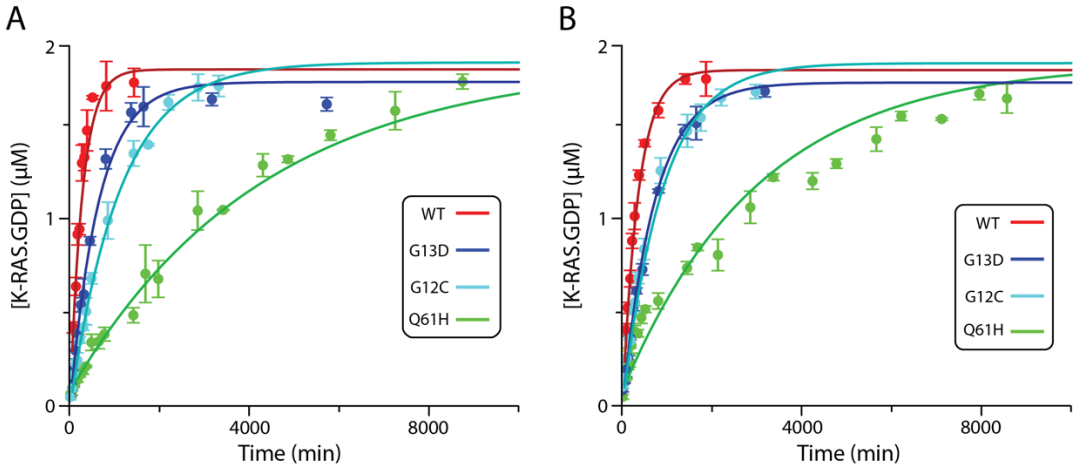

Figure 2.8. Kinetics of intrinsic GTPase activity for KRAS and mutants. (A) Protein samples loaded with (A) GTP or (B) dGTP were incubated at 25 °C and hydrolysis monitored by native MS. Reported are the mean and standard deviation (n = 3).

In general, the $k_{hyd,GTP}$ were lower for the oncogenic mutants studied compared to the WT protein (Figure 2.9A and Table 2.8). $KRAS^{Q61H}$ has the smallest $k_{hyd,GTP}$ compared to the other mutants, nearly tenfold less than that of the WT protein. The mutant proteins have a lower hydrolysis rate than WT but differ among themselves.

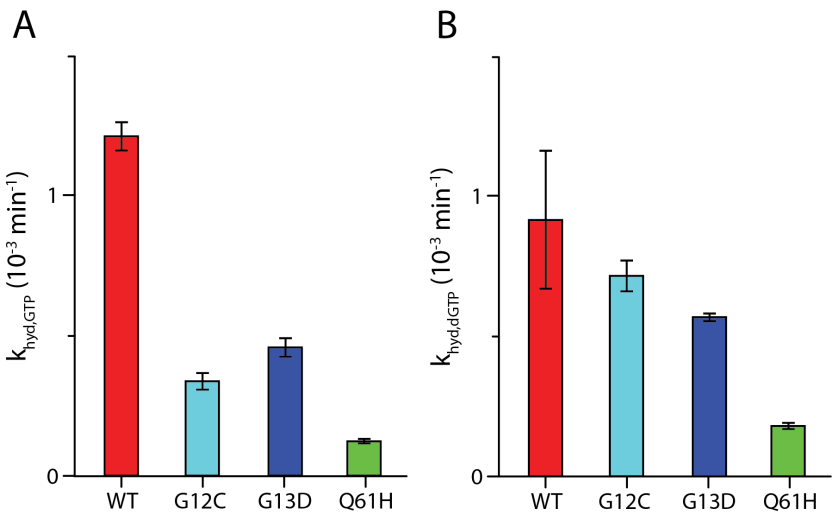

Figure 2.9. The rate of intrinsic GTP hydrolysis for KRAS and mutants loaded with (A) GTP or (B) dGTP. Reported are the mean and standard deviation (n = 3).

Table 2.6. GTP and dGTP intrinsic hydrolysis rates (x10^{-3} min^{-1}) at 25 °C.
Reported are the mean and standard deviation (*n* = 3), and *p*-value from the two-tailed Student's t-test comparing $k_{hyd,GTP}$ and $k_{hyd,dGTP}$.

Protein	$k_{hyd,GTP}$ ± Std	$k_{hyd,dGTP}$ ± Std	$k_{hyd,dGTP}/k_{hyd,GTP}$ ± Relative uncertainty	*p*-value
WT	2.42 ± 0.1	1.91 ± 0.52	0.79 ± 0.27	0.2409
G12C	0.68 ± 0.06	1.5 ± 0.11	2.20 ± 0.11	0.0008
G13D	0.92 ± 0.06	1.19 ± 0.03	1.29 ± 0.07	0.0044
Q61H	0.25 ± 0.01	0.38 ± 0.02	1.52 ± 0.06	0.0013

2.3.4. Intrinsic hydrolysis of dGTP by KRAS and oncogenic mutants

Inspired by the observation of dGDP and dGTP bound to the "as-isolated" proteins, we loaded KRAS and mutants with dGTP and measured the intrinsic hydrolysis (Figure 2.10). For KRAS, no statistically significant difference was observed for the rate of dGTP hydrolysis ($k_{hyd,dGTP}$) compared to $k_{hyd,GTP}$ (Figure 2.8B, Figure 2.9B and Table 2.8). In contRASt, $k_{hyd,dGTP}$ for

$KRAS^{G12C}$, $KRAS^{G13D}$, and $KRAS^{Q61H}$ differed from the rates measured for GTP (Figure 2.9B and Table 2.8). Interestingly, the ratio of $k_{hyd,dGTP}$ to $k_{hyd,GTP}$ indicates that these three mutants (G12C, G13D, and Q61H) hydrolyze dGTP at a higher rate, more than twofold for $KRAS^{G12C}$. In other words, the half-life for these three mutants are much longer for the enzyme bound to GTP compared to dGTP. These results indicate that these oncogenic mutants preferably hydrolyze the 2'-deoxy form of GTP.

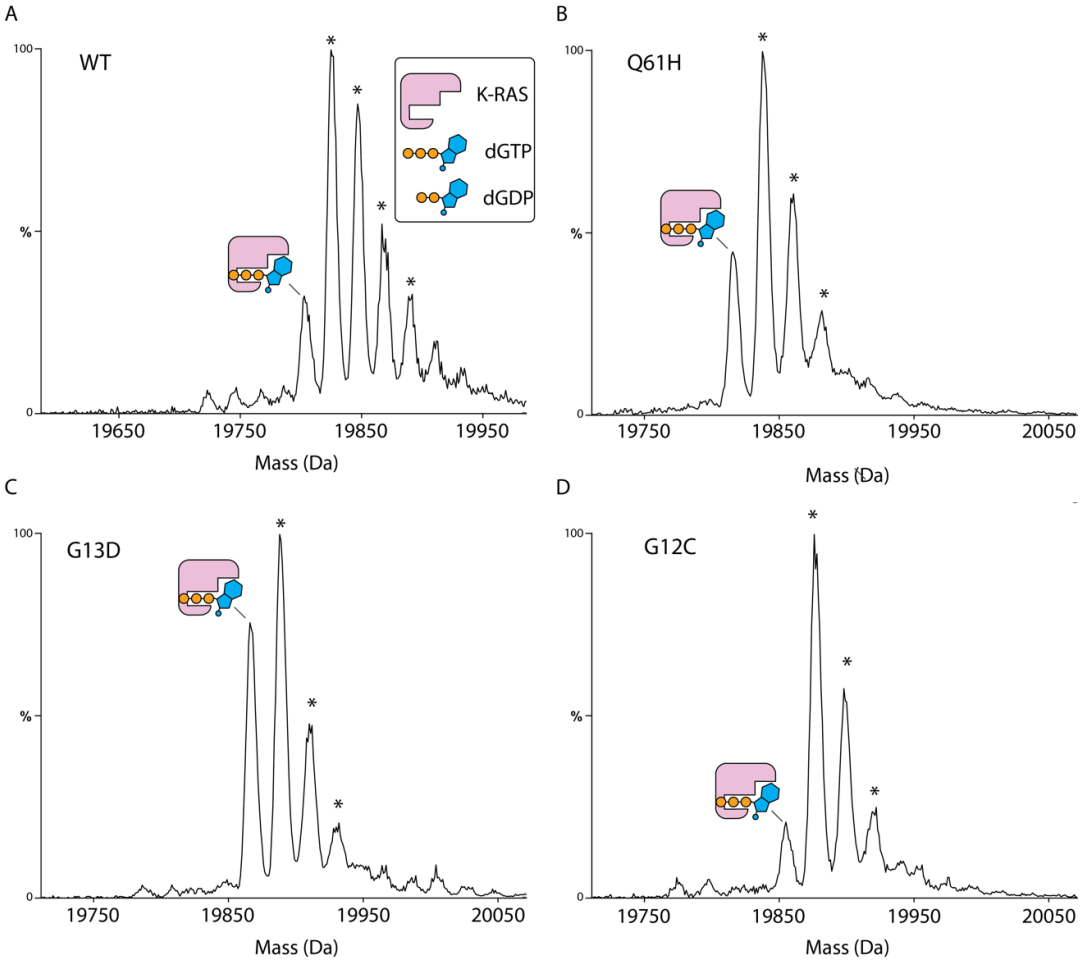

Figure 2.10. Deconvolution of native mass spectra for KRAS (A) WT, (B) Q61H, (C) G13D and (D) G12C loaded with dGTP. Asterisk represents sodium or magnesium bound adducts.

2.3.5. Activation energetics of intrinsic GTPase activity for KRAS and oncogenic mutants

To determine the energetic barriers of intrinsic GTPase activity, the hydrolysis of GTP by KRAS and mutants incubated at three additional temperatures (10, 30, and 37 °C) was monitored by native MS. The $k_{hyd,GTP}$ were determined for the different temperatures, which increased with increasing temperature (Figure 2.11 and Figure 2.12).

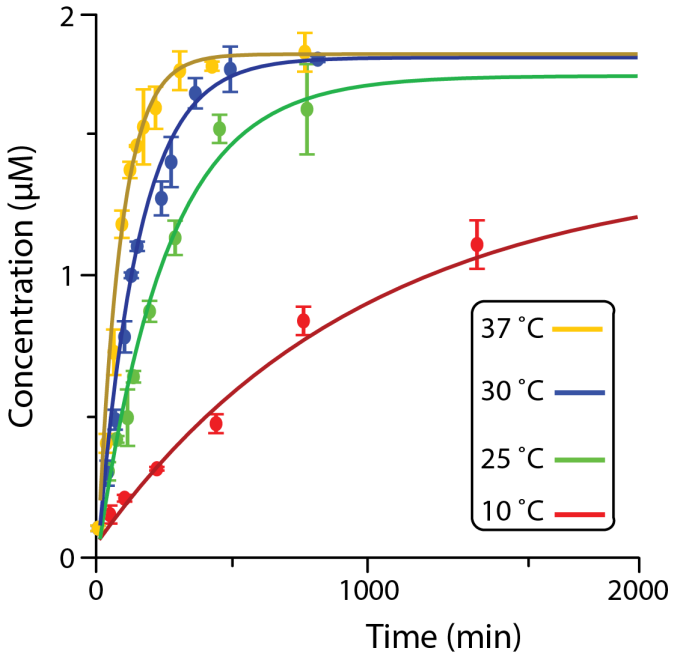

Figure 2.11. Temperature dependence of intrinsic GTPase activity of KRAS. Protein samples were incubated at four different temperatures (10, 25, 30 and 37 °C) and the intrinsic hydrolysis was monitored using native MS. Reported are the mean and standard deviation (n = 3).

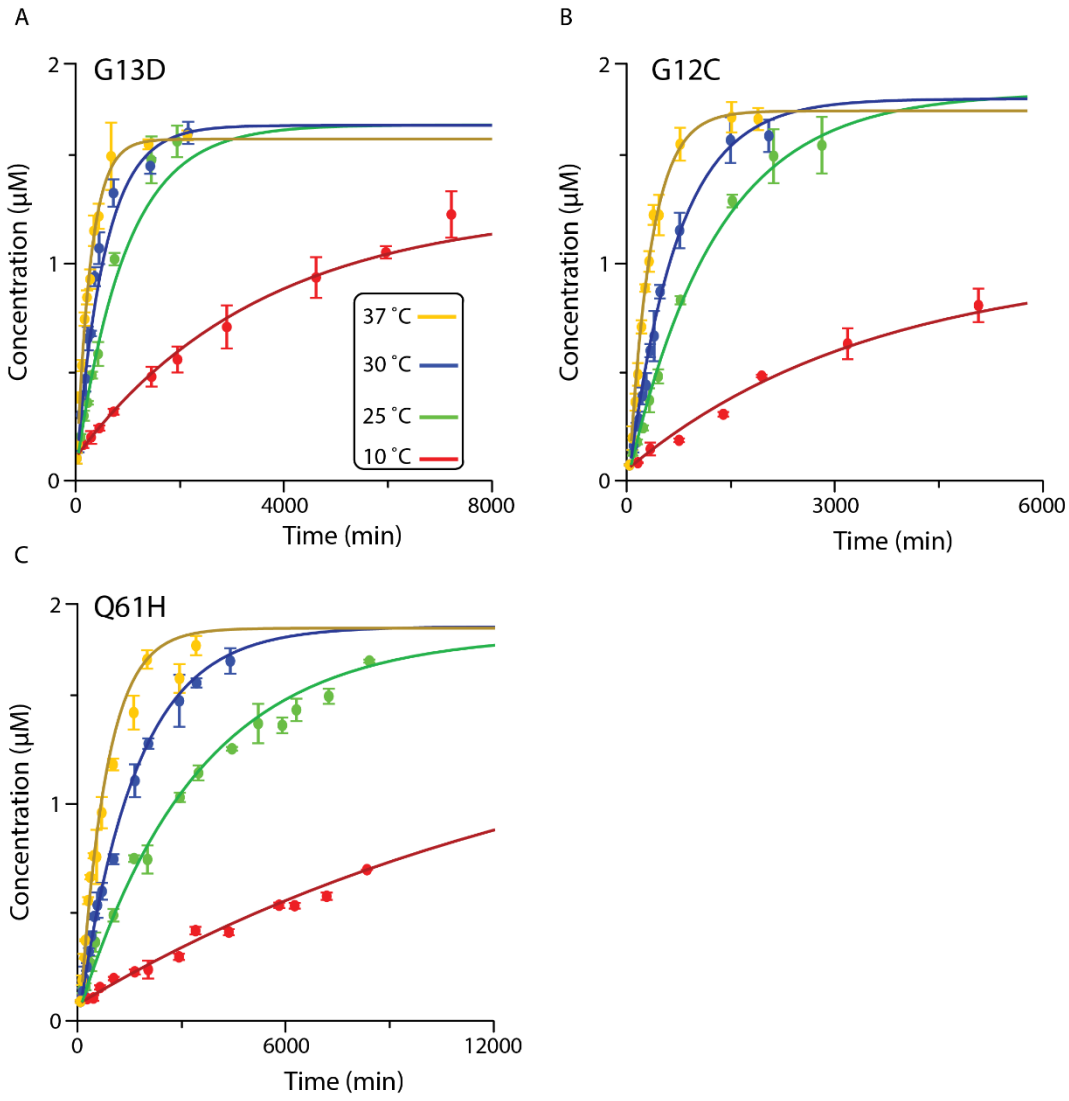

Figure 2.12. The temperature dependence of intrinsic GTP hydrolysis of KRAS (A) G13D, (B) G12C and (C) Q61H.

The $k_{hyd,GTP}$ values at different temperatures were used for Eyring analysis (130), where the natural logarithm of $k_{hyd,GTP}$ divided by temperature is plotted against the reciprocal temperature (Figure 2.13).

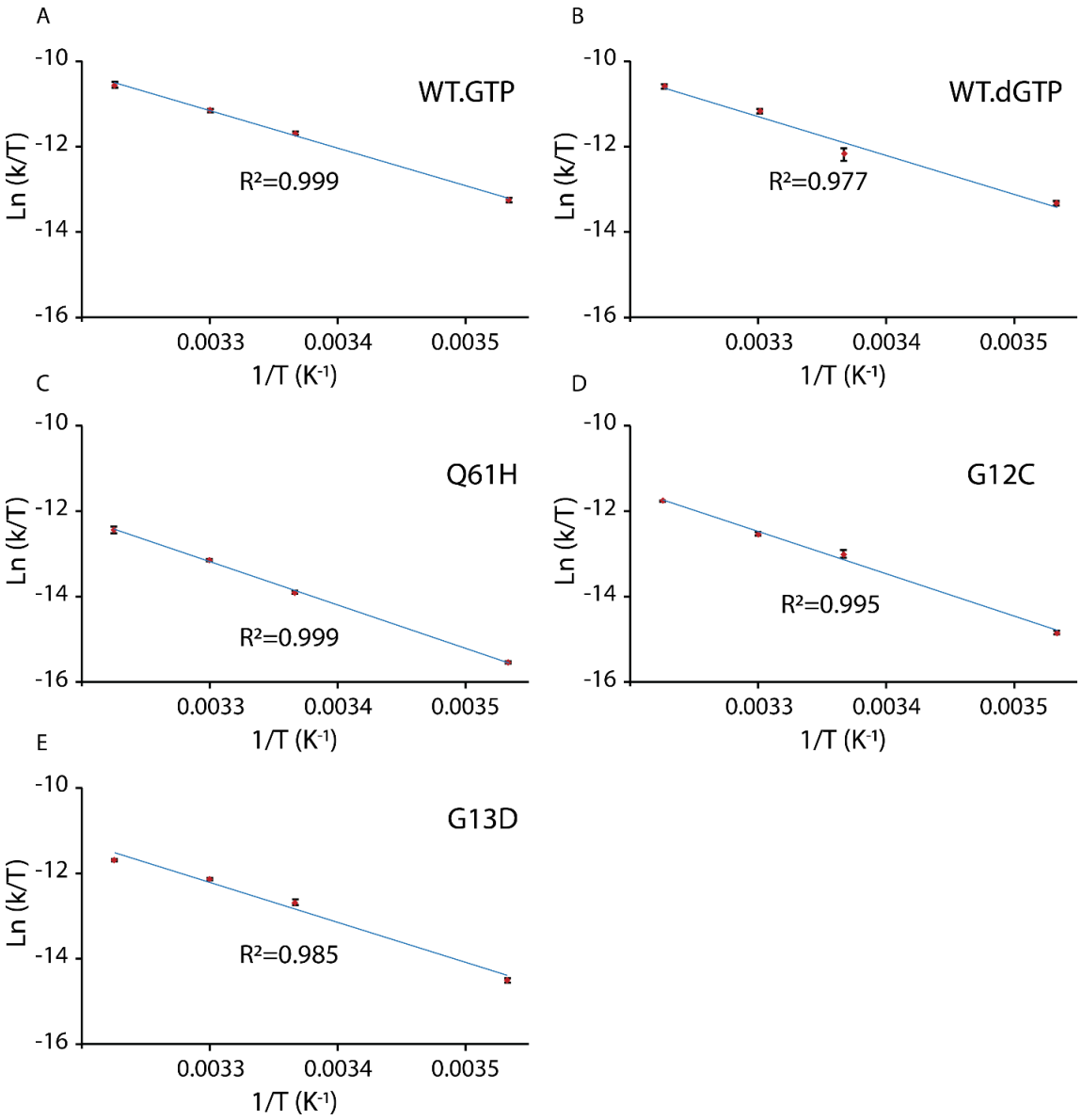

Figure 2.13. Eyring plots generated for KRAS (A) WT•GTP, (B) WT•dGTP, (C) Q61H•GTP, (D) G12C•GTP and (E) G13D•GTP. All data shown are the mean and standard deviation (n=3).

The data were fit to the Erying equation to determine the transition state enthalpy ($\Delta H^{\ddagger}$) and entropy ($\Delta S^{\ddagger}$) (Table 3 and Figure 2.14).

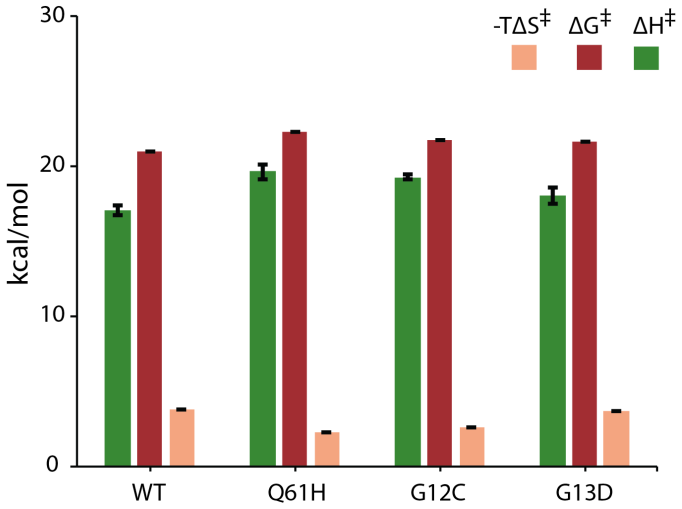

Figure 2.14. Enthalpy ($\Delta H^{\ddagger}$), entropy ($\Delta S^{\ddagger}$) and change in Gibbs free energy ($\Delta G^{\ddagger}$) of activation determined by Eyring analysis (T=298 K). Reported are the mean and standard deviation (n = 3).

The thermodynamic parameters for KRAS derived from Eyring analysis is $\Delta H^{\ddagger}$= 17 kcal/mol, $T\Delta S^{\ddagger}$= -3.9 kcal/mol (T = 298 K) and $\Delta G^{\ddagger}$= 21 kcal/mol. For all proteins studied, the barrier of the transition state is dominated by a large positive $\Delta H^{\ddagger}$, and to lesser extent by a small unfavorable contribution from $\Delta S^{\ddagger}$. Interestingly, the KRAS oncogenic mutants have larger $\Delta H^{\ddagger}$ compared to WT, explaining the reduction in $k_{hyd,GTP}$ (Table 2.9).

Table 2.7. Transition state thermodynamics for the intrinsic GTPase activity of KRAS and oncogenic mutants. $\Delta G^{\ddagger}$ is calculated directly from enthalpy and entropy at a temperature of 25 °C. Reported are the mean and standard deviation of three replicates. (n = 3).

Protein	$\Delta H^{\ddagger}$ (kcal/mol)	$\Delta S^{\ddagger}$(kcal/mol)	$\Delta G^{\ddagger}$(kcal/mol)	$\Delta\Delta S^{\ddagger}$(kcal/mol)	$\Delta\Delta H^{\ddagger}$(kcal/mol)
WT	17.0 ± 0.3	-0.0133 ±0.0011	20.9±0.01		
G12C	19.3±0.1	-0.0084 ±0.0005	21.8±0.01	0.0049 ±0.0012	2.3±0.4
G13D	18.0±0.5	-0.0119 ±0.0018	21.6±0.02	0.0014 ±0.0021	1.0±0.6
Q61H	19.6±0.5	-0.0076 ±0.0014	22.3±0.02	0.0058 ±0.0018	2.6±0.6

The $\Delta\Delta H^{\ddagger}$ ($\Delta H^{\ddagger}_{mutant}$ - $\Delta H^{\ddagger}_{WT}$) depends on the mutant but ranges from 1.0 to 2.6 kcal/mol. In contRASt, the $\Delta S^{\ddagger}$ term becomes more favorable for $KRAS^{G12C}$ and $KRAS^{Q61H}$. Interestingly, the activation energetic for $KRAS^{G13D}$ was similar to the WT protein. Moreover, activation energetics of KRAS hydrolyzing dGTP are similar to those determined for the enzyme loaded with GTP (Figure 2.13B and Table 2.10).

Table 2.8. Thermodynamics of intrinsic GTPase activity for KRAS loaded with dGTP.

Protein	$\Delta S^{\ddagger}$ (kcal/mol)	$\Delta H^{\ddagger}$ (kcal/mol)	$\Delta G^{\ddagger}$ (kcal/mol)
$KRAS^{WT}$.dGTP	-0.0122 ± 0.0009	17.4 ± 0.3	21.06 ± 0.04

2.4. Discussion

2.4.1. Native mass spectra of KRAS and mutants

Native mass spectra of KRAS and mutants reveal heterogeneity in guanosine nucleotides bound to the enzyme. The data show binding of 2'-deoxy and 2'-hydroxy forms of GDP and GTP. Binding of 2'-deoxy guanosine nucleotides has been previously reported.(106) KRAS and mutants were expressed and purified from *E. coli*, where the concentration is 18-fold more abundant for GTP compared to dGTP.(135) Interestingly, the ratio of GDP to dGDP is 4 for KRAS, considerably less than the ratio of the nucleotide pool in the expression host. While the abundance of the GTP and dGTP bound nucleotides are almost similar for KRAS and $KRAS^{G13D}$, $KRAS^{G12C}$ has more dGTP bound implying that the affinity for this nucleotide might be higher. Another interesting observation is the abundance of bound adduct with a larger mass than GTP for $KRAS^{G13D}$ (Figure 2.2B). The observed adduct has a mass difference about +133 Da from GDP which is consistent with the mass of a ribosyl group. Since this adduct was not observed after loading $KRAS^{G13D}$ with GTP or dGTP,

it indicates the molecule is bound non-covalently and does not have any effect on GTP hydrolysis. Identification of this ligand and its biological relevance on G13D function warrants further investigation. Native MS results reveal intrinsic differences of KRAS and variants implying unique biochemical binding properties.

2.4.2. Ion mobility-mass spectrometry measurements

Native ion mobility measurements on KRAS and oncogenic mutants indicate that a native-like structure is preserved in the ion mobility mass spectrometer. An NMR study suggests that H-RAS bound to a non-hydrolyzable analog of GTP (GppNHp) populates active and inactive conformations that interconvert on the millisecond time scale (136-138). Moreover, molecular dynamic simulations of oncogenic mutants, including G12D, G13D and Q61H, suggest that these proteins mainly populate an active conformation whereas G12C behaves similarly to KRAS populating two conformations.(139) The ATD for KRAS and mutants did not exhibit mobility profiles with multiple peaks. The centroid CCS values show differences between WT and mutants. For example, the CCS values for $KRAS^{G12C}$ and $KRAS^{G13D}$ bound to GTP are larger than WT (Figure 2.6A and C). The CCS for $KRAS^{Q61H}$ bound to GTP is smaller compared to the other proteins indicating a more compact conformation which is also evident from the width of the ATD (Figure 2.6B and Table 1). From X-ray crystallography studies, the H61 of $KRAS^{Q61H}$ is less exposed to solvent due to formation of hydrophobic cluster above the complex of nucleotide and water.(140) This is consistent with the smaller CCS measured for this oncogenic mutant. These results show that native IM-MS can be informative for structural changes induced by mutation, and the development of higher resolution IM-MS instruments(141, 142) has great potential to capture different conformations of KRAS that have been observed by NMR and X-ray crystallography.

2.4.3. Monitoring GTPase activity by high resolution native MS

As revealed by high-resolution native mass spectra, both 2'-deoxy and 2'-hydroxy forms of guanosine nucleotides were bound in the "as isolated" samples prompting us to determine intrinsic dGTPase activity. Several factors can impact the rate of hydrolysis including temperature, buffer, ionic strength, pH and the concentration of divalent metal ion, magnesium. (143) The intrinsic GTP hydrolysis activity for KRAS is consistent with other reports using NMR and radioactive methods.(21, 144) Moreover, MS derived rates are in direct agreement with those determined by a solution-based assay.

Intrinsic GTPase activity for oncogenic mutants exhibit differences in hydrolysis rates of dGTP compared to GTP. However, no difference in hydrolysis rates of dGTP and GTP was observed for KRAS. For $KRAS^{Q61H}$, $KRAS^{G12C}$ and $KRAS^{G13D}$ the rate of dGTP hydrolysis was higher than that for GTP. From atomic structures of KRAS and mutants, the ribose of the bound nucleotide is in 2'-endo conformation, and the 2'-hydroxyl group forms weak hydrogen bonds with the side chain of Asp30 and the carbonyl group of Val29.(22) When dGTP is replaced with GTP, these hydrogen bonds are lost which probably leads to reordering of nucleotide and subsequently enhance enzyme activity.

RAS oncogenes have the ability to reprogram the metabolic process in cancer cells.(145) It has also been established that imbalances in deoxyribonucleotide triphosphate (dNTP) pool is directly associated with different diseases including diabetes, obesity and cancer due to enhanced mutagenesis which causes genomic instability.(146) The relationship of the dNTP pool and our observation of higher dGTP intrinsic hydrolysis rates for oncogenic mutants compared to the wild-type protein warrants further investigation.

2.4.4. Activation energetics of intrinsic GTPase activity

Activation energetics was determined for the intrinsic GTPase activity of KRAS and mutants providing insight into the barriers of the transition state. The values determined for GTPase activity of KRAS are in excellent agreement with FT-IR data (110) ($\Delta H^{\ddagger}$= 19.8 kcal/mol and $T\Delta S^{\ddagger}$= -2.3 kcal/mol) and MD simulations ($\Delta H^{\ddagger}$= 17.4 kcal/mol and $T\Delta S^{\ddagger}$= -4 kcal/mol).(147) The observed small entropic effects of KRAS catalyzed hydrolysis of GTP is consistent with MD simulations that showed $\Delta\Delta S^{\ddagger}$ ($\Delta S^{\ddagger}_{enzyme}$-$\Delta S^{\ddagger}_{water}$) has a small contribution to the catalysis since reactants do not lose their entire translational and rotational motion when they are bound to enzyme.(148) The large enthalpic barrier is also consistent with Warshel *et al.* studies that showed less free energy needed to orient dipoles at the active site of an enzyme compared to uncatalyzed reactions in water since the active site of the protein includes the ionized residues, polar groups and water molecules.(149) This highly polar and reorganized active site of the enzyme suggests that the enthalpic effects have more contributions in catalysis and the small reorganization energy is paid during enzyme folding.(148, 150) There is a gain in enthalpy for all of the oncogenic mutants studied ($\Delta\Delta H^{\ddagger}$) and a small increase in entropy ($\Delta\Delta S^{\ddagger}$) for the transition state of intrinsic GTPase activity. The value for $\Delta\Delta H^{\ddagger}$ is higher for $KRAS^{Q61H}$ explaining why the hydrolysis rate for this mutant is much slower followed by $KRAS^{G12C}$ and $KRAS^{G13D}$. The activation energetics for KRAS and oncogenic mutants explains their different rates of GTP hydrolysis.

In summary, high-resolution native MS was used to determine the kinetics and thermodynamics of intrinsic GTP hydrolysis of KRAS and mutants. Native MS is a rapid and sensitive (minimal sample consumption) technique that revealed heterogeneity of the nucleotide bound to the “as isolated” proteins. For oncogenic mutants, the rates of hydrolysis of dGTP were faster than GTP hydrolysis. This result implies that the mutants bound to dGTP spend less time in

an active state. Moreover, activation energetics reveals the barrier of the transition state is dominated by enthalpy and to a much lesser extent by entropy. The reduction in intrinsic hydrolysis for oncogenic mutants is due to an increase in the enthalpic barrier.

3. MOLECULAR ASSEMBLIES OF THE CATALYTIC DOMAIN OF SOS WITH KRAS AND ONCOGENIC MUTANTS *

3.1. Introduction

RAS, a member of the small G-protein family, represents important signaling molecules with diverse cellular roles, such as cell differentiation and proliferation.(6, 85, 102, 151) Different isoforms of RAS (HRAS, KRAS, and NRAS) have high overall sequence identity and are the most commonly mutated of all discovered oncogenes (92, 96). Of the three RAS isoforms, KRAS is the most frequently mutated isoform in cancers, such as pancreatic cancer (70-90%), colon cancer (30-50%), and lung cancer (20-30%) (7, 101). RAS proteins regulate cell signaling pathways by cycling between an inactive, GDP-bound and active, GTP-bound states that is accompanied by remodeling of three key regions within RAS: p-loop (residues 10-17); switch I (residues 30-38), and switch II (residues 60-76) (23, 86, 91).

As RAS proteins possess slow guanine nucleotide exchange rates, their activation is regulated by guanine nucleotide exchange factors (GEFs) that reload RAS with GTP (4, 26). The multidomain protein, Son of Sevenless (SOS) is a GEF with the cdc25 and RAS exchanger motif domains representing the minimal, functionally-competent unit, termed SOS^{cat} (152). Structural studies have revealed two RAS binding sites to SOS^{cat}, leading to the discovery that binding of RAS-GTP at the distal (or allosteric) site allosterically modulates SOS^{cat} activity, which markedly increases the nucleotide exchange rate at the active site (152, 153). In addition, the degree of this

* Reprinted with permission from Moghadamchargari, Z.; Shirzadeh, M.; Liu, C.; Schrecke, S.; Packianathan, C.; Russell, D. H.; Zhao, M.; and Laganowsky, A. Molecular assemblies of the catalytic domain with SOS and KRAS and oncogenic mutants. *PNAS,* **2021***,* 118(12).

allosteric modulation greatly depends on the nucleotide bound state of RAS (152, 154, 155). Moreover, SOS is conformationally

dynamic and binding of RAS at the allosteric site appears to shift the population to active conformation(s) of SOS (156). In addition, SOS^{cat} samples a broad range of turnover rates by fluctuating between distinct, long-lived functional states (157). Despite these advances, the nucleotide specificity of RAS bound to the active and allosteric sites of SOS and assembly with RAS, including oncogenic mutants, at the molecular level is poorly understood.

Targeting oncogenic RAS mutants presents significant challenges because of their relatively smooth surface that lacks potentially druggable pockets (92). Nevertheless, the discovery of KRAS inhibitors, particularly those that form irreversible covalent bonds with Cys-12, comprises one of the most active areas of cancer research (92, 158). As there are few windows of opportunity to specifically target RAS mutants,(92) apart from covalent binding to Cys-12, other approaches have also been explored, such as designing molecules to disrupt RAS•SOS interactions thereby preventing activation of RAS (158). An increasing number of small molecule disruptors and peptide mimetics have been designed to disrupt the RAS•SOS interaction (159). Potent small molecule disruptors have recently been discovered that inhibit the formation of the RAS•SOS complex and demonstrate antiproliferative activity, representing a viable approach for targeting RAS-driven tumors (160, 161). These results highlight the therapeutic importance of disrupting the interaction between RAS and SOS.

Over the past three decades, native ion mobility-mass spectrometry (IM-MS) has evolved as a powerful analytical technique to investigate protein complexes and their interaction with other molecules (112, 123, 162). In native MS, biological samples in aqueous ammonium acetate are ionized using nanoelectrospray ionization and introduced into a mass spectrometer tuned to

preserve non-covalent interactions and structure (36, 112). Native IM-MS can provide information on protein complexes, such as subunit stoichiometry and topology (62), and, unlike other biophysical techniques, resolve individual ligand-binding events (163). In combination with an apparatus to control temperature, native MS can be used to determine equilibrium binding constants and thermodynamics for protein-ligand and protein-protein that are in direct agreement with traditional biophysical approaches, such as isothermal calorimetry (117, 164-168). Recently, native MS has been employed to determine transition state thermodynamics for the intrinsic GTPase activity of KRAS and several oncogenic mutants (169). Notably, intrinsic GTPase activity rates determined using traditional solution-based assays mirrored those obtained using native MS (169).

Although the interaction of RAS and SOS has been the subject of numerous studies, the interaction of oncogenic RAS mutants with SOS remains poorly described. To better understand the role of these interactions in cancer, native IM-MS is used to characterize the molecular assemblies formed between SOS^{cat} and mutants of KRAS associated with cancer. IM spectrometry shows conformational heterogeneity of SOS^{cat} with specific conformers engaging KRAS. Three selected oncogenic mutants of KRAS form distinct molecular assemblies with SOS^{cat}, such as $KRAS^{G13D}$ forming exclusively a ternary complex with SOS^{cat}. The cryo-EM structure of the $KRAS^{G13D}$•SOS^{cat} complex provides insight into the mechanism for the higher affinity of $KRAS^{G13D}$ for SOS^{cat}. $KRAS^{G13D}$-GTP also allosterically modulates the activity of SOS^{cat} more than the wild-type protein. In addition, the recent inhibitors developed to disrupt the KRAS•SOS^{cat} complex, BAY-293 and BI-3406, cannot dissociate $KRAS^{G13D}$•SOS^{cat} complexes. Other small molecules, such as ARS-1620 and Kobee0065, display a range of efficacies in disrupting complexes formed between KRAS mutants and SOS^{cat}.

3.2. Methods

3.2.1. Protein expression and purification

The KRAS4B (residues 1-169) was expressed and purified as previously described.(169) In brief, the KRAS4B (referred to as KRAS) expression construct including an N-terminal TEV protease cleavable His_6 tag was transformed into Lemo21-(DE3) *E. coli* (New England Biolabs) and grown in LB medium supplemented with 50 μg/mL kanamycin. Protein expression was induced with 500 μM IPTG and cells were grown at 18 °C overnight. The cells were harvested and stored at -80 °C. Cell pellets were thawed on ice and resuspended in buffer A (500 mM NaCl, 20 mM Tris pH 7.4) supplemented with a complete protease inhibitor tablet (Roche) and 5 mM β-mercaptoethanol (β-ME). The cell suspension was lysed by a microfluidizer (Microfluidics M-110P) at 20000 psi, and was clarified by centrifugation at 30000g for 30 minutes. All purification steps were performed at 4 °C. The clarified lysate was loaded onto a 5 mL HisTrap HP column (GE Healthcare) pre-equilibrated in buffer A. The protein was eluted with buffer A containing 500 mM imidazole. The fractions containing protein were pooled and desalted using a HiPrep 26/10 desalting column (GE Healthcare) equilibrated in buffer A. The desalted protein was then digested with TEV protease at 4 °C and incubated overnight to remove the N-terminal affinity tag. The proteins were passed over a 5 mL HisTrap HP column equilibrated with buffer A, and flow-through containing tag-less protein was collected. The flow-through was further diluted and loaded onto a 5 mL HiTrap Q HP column (GE Healthcare) equilibrated with buffer B (50 mM NaCl and 20 mM Tris pH 8), and eluted with a linear gradient from 0-1000 mM NaCl over 5 column volumes. The eluted protein was concentrated and subjected to size exclusion chromatography using a Highload 16/600 Superdex 75 pg column (GE Healthcare) equilibrated in buffer C (150 mM sodium chloride, 5 mM β-ME, 20% glycerol, and 20 mM Tris pH 7.4). Peak fractions containing protein were pooled,

concentrated using a centrifugal concentrator (Millipore, 10K molecular weight cutoff (MWCO)), flash-frozen using liquid nitrogen, and stored at −80 °C.

The SOS^{cat} (human SOS1, residues 558-1049, Uniprot Q07889) plasmid for expression in *E. coli* was a kind gift from Prof. John Kuriyan (University of California, Berkeley). SOS^{cat} was expressed and purified as previously described.(152) In detail, the expression construct includes an N-terminal TEV protease cleavable His_6 tag was transformed into Rosetta 2 DE3 cells (Novagen) and grown in LB medium supplemented with 100 μg/mL ampicillin and 34 μg/mL chloramphenicol. The expression and purification of SOS^{cat} was carried out in a similar fashion as KRAS. All mutations were generated using the Q5 site-directed mutagenesis kit (New England Biolabs) following the manufacturer's protocol.

The KRAS.SOS^{cat} complex was formed by incubation of the two proteins with three-fold molar excess of KRAS-GTP in the presence of 2 mM EDTA at 4 °C overnight. The complex was loaded into a Highload 16/600 Superdex 75 pg column equilibrated with buffer C. The fractions containing the KRAS•SOS^{cat} complex were pooled and concentrated and analyzed using Synapt G1 mass spectrometry under native conditions.

3.2.2. Loading of KRAS and mutants with nucleotides

KRAS and three oncogenic mutants studied here (G13D, Q61H and G12C) were loaded with either GTP or GDP to monitor the assembly with SOS^{cat}. The nucleotide exchange assay was carried out as described elsewhere.(169) In brief, KRAS and oncogenic mutants were incubated with 30 molar excess ratio of either GDP or GTP in the presence of 10 mM EDTA for 3 hours at 4 °C. The reaction mixture was then supplemented with 10 mM $MgCl_2$ and incubated for 30 minutes at 4 °C. Excess nucleotide, $MgCl_2$ and EDTA were removed using a Micro Bio-Spin 6 desalting column

(Bio-Rad). The procedure of nucleotide exchange was repeated until full exchange of GDP or GTP was complete as determined by native MS measurements.

3.2.3. Nucleotide exchange assay

To monitor the nucleotide exchange rate, KRAS was loaded with B-GDP as explained above, and the excess of B-GDP was removed by HiTrap HP desalting column (GE Healthcare). SOS^{cat} (1 μM) was mixed with KRAS-B-GDP (1 μM) at 1:1 molar ratio and incubated in ice for 10 minutes. The SOS^{cat}-mediated nucleotide exchange was initiated by addition of excess 200 μM unlabeled GTP. In order to study the effect of allosteric KRAS on nucleotide exchange rate, $KRAS^{G13D}$-GTP, $KRAS^{WT}$-GTP and $KRAS^{Q61H}$-GTP were mixed separately with 200 μM GTP and added to the mixture of SOS^{cat} and KRAS-B-GDP and fluorescence (excitation 466.5 nm and emission 512-520 nm) was measured. The final reaction contains 0.5 μM SOS^{cat}, 0.5 μM KRAS-B-GDP, 200 μM GTP and 1.5 μM of allosteric KRAS-GTP, $KRAS^{G13D}$-GTP or $KRAS^{Q61H}$-GTP. The nucleotide exchange rate was monitored by a change in fluorescence over time using a Clariostar (BMG labtech) plate reader. The qualitative rate constants were obtained by fitting the data to a single exponential equation.

3.2.4. Inhibitor binding assay

Inhibitors were purchased from Tocris Bioscience (Kobe0065, cat no:5475, BAY-293, cat no:6857), Chemietek (ARS1620, cat no: CT-ARS1620) and TargetMol (BI-3406, cat no: T12979). To confirm the specificity of ARS-1620 for inactive state of $KRAS^{G12C}$, 10 μM ARS-1620 was mixed with 3 μM $KRAS^{G12C}$-GDP or $KRAS^{G12C}$-GTP and native mass spectra was collected (Fig. S8). In order to study the ability of ARS-1620 to disrupt the $KRAS^{G12C}$ complexed with SOS^{cat}, 10 μM ARS-1620 was added to pre-incubated complex (1 μM SOS^{cat} mixed with 3 μM $KRAS^{G12C}$-GDP or $KRAS^{G12C}$-GTP incubated for five minutes) and the mixture was incubated for another 60

minutes in ice and native mass spectra were recorded. Similar experiments were carried out to test the ability of BAY-293 and Kobe0065 to disrupt binary and ternary complexes of SOS^{cat} and KRAS, $KRAS^{G13D}$ and $KRAS^{G12C}$. 2.5 μM BAY-293 was added to pre-incubated mixtures of 1 μM SOS^{cat} and 3 μM of KRAS-GTP or $KRAS^{G13D}$-GTP and incubated in ice for 60 minutes and subsequent native mass spectrum was recorded. Similar experiments were performed with BAY-293 on SOS^{W729E} complexes with KRAS-GDP and $KRAS^{G13D}$-GDP. Mass spectra of 2.5 μM Kobe0065 added to pre-incubated mixtures of 1 μM SOS^{cat} and 3 μM KRAS-GTP or $KRAS^{G13D}$-GTP were also recorded.

3.2.5. Inorganic phosphate assay

The phosphate concentration of KRAS alone and in the presence of SOS^{cat} was measured using a malachite green assay.(128) In brief, malachite green reagent (1 mg/mL malachite green, 100 mg/ mL ammonium molybdate, and 0.01% Triton X-100 in 50 mL of 1 M hydrochloric acid) was prepared as described previously.(129) KRAS-GTP was mixed with SOS^{cat} and incubated for 5 minutes on ice. To determine the phosphate concentrations of complex mixture and control solutions (KRAS-GTP and SOS^{cat} alone), 40 μl malachite green reagent was added individually to 10 μl of control solution or complex mixture and incubated for 15 minutes at room temperature. Absorbance was measured at 650 nm using a Clariostar (BMG labtech) plate reader and subtracted from buffer. A standard curve was generated by serial dilutions of 1 mM dipotassium phosphate. All measurements were done in triplicate, and solutions were made using OmniTrace Ultra water (Sigma-Aldrich) to minimize background phosphate.

3.2.6. Sample preparation to monitor the assembly of the complex via native MS analysis

In order to obtain mass spectra of KRAS or mutants (loaded with GDP or GTP) complexed with SOS^{cat} or SOS^{W729E}, KRAS, SOS^{cat} and SOS^{W729E} were separately buffer exchanged into 100 mM

ammonium acetate (pH 7.4) using a Micro BioSpin 6 column (Bio-Rad). The GTP or GDP loaded KRAS was mixed with SOS^{cat} or SOS^{W729E} at 3:1 molar ratio in ammonium acetate and immediately analyzed using native MS. For BODIPY-GTP and Mant-GTPγS experiments, 2 and 5 μM of the fluorophore analogs were added to the preformed mixture of SOS^{cat} and KRAS-GTP, respectively (Fig 3.1D) and was immediately analyzed using native MS.

3.2.7. Native mass spectrometry

Protein samples were introduced into an Exactive Plus with extended mass range (EMR) Orbitrap MS (Thermo Fisher Scientific, San Jose, CA). Samples were loaded into pulled borosilicate glass capillaries prepared in-house, and electrosprayed into the instrument with the voltage applied using a platinum wire directly inserted into the solution. Instrument parameters (Table 3.1) were tuned to minimize gas phase activation and to preserve non-covalent interactions between KRAS and SOS^{cat} or SOS^{W729E}. All of the measurements were taken in triplicate and repeated on different days. The mole fractions of free SOS^{cat}, binary and ternary complexes were determined using Unidec software (125) for all triplicates and average values were used for circle graphs.

Table 3.1. Tuned instrument parameters used for monitoring the assembly of KRAS and mutants with SOS^{cat} or SOS^{W729E} using an orbitrap mass spectrometer.

Instrument Parameters	
m/z range	1000-8000
Resolution	8000
In-source collision energy dissociation (V)	100
Collision energy	10
Source temperature (°C)	100
Capillary voltage (KV)	1.5
Source DC offset (V)	25
Injection flatapole lens(V)	18
Inter flatapole DC (V)	4
Bent flatapole DC (V)	5
Transfer multipole DC (V)	2
Pressure (mbar)	3×10^{-10}

3.2.8. Native Ion mobility mass spectrometry

The solution dynamics and conformational heterogeneity of SOS^{cat} in the presence and absence of KRAS was analyzed using an Agilent 6560 ion mobility Q-TOF mass spectrometer (Agilent Technologies, Santa Clara, CA). A home-built nano-electrospray ionization source was used to generate native-like ions to preserve non-covalent interactions and pulsed into the drift tube filled with nitrogen gas for ion mobility measurements. To determine the first-principle CCS calculations,(170) the arrival time distributions were plotted as a function of drift voltage to determine the time ions spend outside the drift tube. CCS was calculated using the Mason-Schamp equation(171) with the following instrumental parameters: pressure (~3.915 torr), temperature (24.5 °C) and drift length (78 cm). Instrumental settings are provided in Table 3.2 and 3.3.

Table 3.2. Instrument tuning parameters for settings for Agilent 6560.

Instrument Parameters	
Capillary voltage (V)	1000-2000
Drying gas temperature (℃)	200
Drying gas flow (L/min)	1.5
Fragmentor (V)	400
High Pressure funnel delta (V)	150
High Pressure Funnel RF (V)	200
Trap funnel delta (V)	180
Trap funnel RF (V)	200
Trap Funnel Exit (V)	10

Table 3.3. Drift Tube Settings for Stepped Field Experiments in Positive Ion Mode on the Agilent 6560.

Sequence	Time (min)	Drift Tube Entrance (V)	Drift Tube Exit (V)	Rear Funnel Entrance (V)	Rear Funnel Exit (V)
1	0.0 – 0.5	1074	224	217.5	45
2	0.5 – 1.0	1174	224	217.5	45
3	1.0 – 1.5	1274	224	217.5	45
4	1.5 – 2.0	1374	224	217.5	45
5	2.0 – 2.5	1474	224	217.5	45
6	2.5 – 3.0	1574	224	217.5	45
7	3.0 – 3.5	1674	224	217.5	45

3.2.9. Collision-induced and Surface-induced dissociation experiments

Collision-induced dissociation experiments were performed on Synapt G1 (Waters). The ternary complexes of KRAS or $KRAS^{G12C}$ with SOS^{cat} were mass isolated in the quadrupole and activated inside the trap region. The instrument parameters were set to a capillary voltage 1.8 kV, sampling cone 50 V, extraction cone 5 V, low mass resolution 3.5, trap collision energy 100 V, transfer collision energy 10 V, Trap gas flow 2 ml/min and source temperature of 90 °C. For SID experiments, samples were analyzed using Synapt G2 (Waters) tuned to maximize signal while preserving non-covalent interactions. Some parameters include capillary voltage 1.2 kV, sampling cone 20 V, extraction cone 1 V, trap gas flow 4 ml/min, He flow 120 ml/min, IMS (N_2) flow 60 ml/min and source temperature of 30 °C. For mass selection of all charge states of ternary complex, the quad profile was set to manual range = 6000 m/z. SID design and surface modification has been previously described (172).

3.2.10. Cryo-electron microscopy

To obtain the ternary complex of $KRAS^{G13D}$ and SOS^{cat}, first $KRAS^{G13D}$ was loaded with GppNp (Guanosine 5'-[β,γ-imido] triphosphate trisodium) and excess nucleotide was removed by HiTrap desalting (5ml, GE) column and concentrated to 15 mg/ml. The complex was formed by incubation of 3-fold molar excess of $KRAS^{G13D}$-GppNp with SOS^{cat} for 1 hour in ice followed by size-exclusion chromatography to purify the complex to homogeneity.

3.2.10.1. Data collection for single-particle cryo-EM

The $KRAS^{G13D}$•SOS^{cat}•$KRAS^{G13D}$-GppNp complex was concentrated to 8.6 mg/mL for cryo-EM grid preparation. To reduce protein aggregation, 0.5% fluorinated octyl maltoside (Anatrace) was added to the samples to a final concentration of 0.05% prior to freezing. Sample vitrification was performed using a Vitrobot Mark IV (Thermo Fisher) operating at 8 ^{o}C and 100% humidity. A

total of 3.5 μL of the sample was applied to holey carbon grids (Quantifoil 200 mesh Cu 1.2/1.3) glow-discharged for 30 seconds. The grids were blotted for 1 second at a blotting force of 1 using standard Vitrobot filter paper (Ted Pella, 47000-100), and then plunged into liquid ethane.

Frozen grids were shipped to the National Center for Cryo-EM Access and Training (NCCAT) for data collection. The dataset was acquired as movie stacks with a Titan Krios electron microscope operating at 300 kV, equipped with a K3 direct detector camera. Images were recorded at a magnification of 105,000x at super-resolution counting mode by image shift. The total exposure time was set to 2.5 s with a frame recorded every 0.05 s, resulting in 50 frames in a single stack with a total exposure around 65 electrons/Å^2. The defocus range was set at -0.8 to -2.5 μm. See Table 3.4 for the details.

3.2.10.2. Image processing

Stack images were subjected to beam-induced motion correction by MotionCor2.(173) CTF parameters for each micrograph were determined by CTFFIND4.(174) The following particle selection, two- and three-dimensional classifications, three-dimensional refinement, and post-processing were performed in RELION-3.1.(175) The detailed data processing flow is shown in Fig 3.15. Briefly, particles were selected by automatic picking, using the 2D templates generated from ~2,000 manually picked particles. Contamination and poorly-aligned classes were disposed after 2D classification. 2,294,620 particles were selected for the initial 3D classification using a previously reported HRAS•SOS^{cat}•HRAS-GDP complex (PDB 1XD2) as a reference model, followed by 3D refinement, post-processing, CTF refinement, and Bayesian polishing performed on the best class. The final map for the KRAS^{G13D}•SOS complex was resolved at 3.47 Å.

3.2.10.3. Model Building, Refinement, and Validation

Previously reported H-RAS•SOS^{cat}•H-RAS-GDP complex structure (PDB 1XD2) was docked into the cryo-EM map as a rigid body using Chimera(176) HRAS-GTP bound at the allosteric site was replaced by aligning the KRAS^{G13D} bound to GppNp (PDB 6E6F) in Coot.(177) In a similar fashion, the H-RAS molecule bound at the active site was replaced by aligning KRAS^{G12C} (PDB 6EPL) followed by mutation of residues to match the KRAS^{G13D} sequence in Coot. After these operations, the model was manually refined using Coot(177) followed by one round of real-space refinement using Phenix(178) with secondary-structure and Ramachandran restraints. Geometry outliers were manually fixed in Coot. The statistics of the final round of model refinement and the model geometry are shown in Table 3.5.

Table 3.4. Statistics of cryo-EM data collection and processing

	$KRAS^{G13D}$•SOS^{cat}•KRAS-GppNp
Microscope	Krios (NCCAT)
Magnification	105,000
Voltage (kV)	300
Spherical aberration (mm)	2.7
Detector	K3
Camera mode	Super resolution counting
Exposure rate (e^-/pixel/s)	30
Total exposure ($e^-/Å^2$)	65
Defocus range (μm)	-0.8 to -2.5
Pixel size (Å)	0.5325 (1.065 physical)
Mode of data collection	Image shift
Energy filter	30 eV slit
Software for data collection	Leginon
Number of micrographs	5,202
Symmetry imposed	C1
Box size (pixel)	192
Initial particle images (no.)	5,749,548
Particle images for 3D (no.)	2,294,620
Final particle images (no.)	1,021,288
Map resolution, unmasked (Å)	3.85
Map resolution, masked (Å)	3.47
B-factor used for sharpening ($Å^2$)	-162
EMD code	EMD-22857
PDB code	7KFZ

Table 3.5. Statistics of cryo-EM refinement and geometry.

	Model	
Composition (#)		
Chains	3	
Atoms	6588 (Hydrogens: 0)	
Residues	Protein: 803 Nucleotide: 0	
Water	0	
Ligands	GppNp: 1, Mg^{2+}: 1	
Bonds (RMSD)		
Length (Å) (# > 4σ)	0.005 (0)	
Angles (°) (# > 4σ)	0.562 (0)	
MolProbity score	1.35	
Clash score	6.33	
Ramachandran plot (%)		
Outliers	0.00	
Allowed	2.02	
Favored	97.98	
Rama-Z (Ramachandran plot Z-score, RMSD)		
whole (N = 791)	0.05 (0.27)	
helix (N = 64)	0.13 (0.68)	
sheet (N = 43)	0.71 (0.66)	
loop (N = 684)	0.13 (0.22)	
Rotamer outliers (%)	0.00	
Cβ outliers (%)	0.00	
Peptide plane (%)		
Cis proline/general	2.5/0.0	
Twisted proline/general	0.0/0.0	
CaBLAM outliers (%)	0.13	
ADP (B-factors)		
Iso/Aniso (#)	6588/0	
min/max/mean		
Protein	21.61/141.57/50.14	
Ligand	41.29/49.62/49.37	
Data		
Box		
Lengths (Å)	73.48, 100.11, 124.61	
Angles (°)	90.00, 90.00, 90.00	
Supplied Resolution (Å)	3.5	
Resolution Estimates (Å)	Masked	
d FSC (half maps; 0.143)	3.5	
d 99 (full/half1/half2)	6.4/3.3/3.4	
d model	4.1	
d FSC model (0/0.143/0.5)	3.0/3.1/3.4	
Map min/max/mean	-0.14/0.24/0.00	
Model vs. Data		
CC (mask)	0.85	
CC (box)	0.74	
CC (peaks)	0.72	
CC (volume)	0.83	
Mean CC for ligands	0.92	

3.3. Results

3.3.1. Conformational dynamics of SOS^{cat} and conformational selection of KRAS

To investigate the interaction between SOS and RAS, we selected SOS^{cat}, which can bind up to two RAS molecules, and KRAS due to its importance in cancer.(7, 101) The KRAS•SOS^{cat} complex purified following methods established for structural studies (152, 153) was subjected to native IM-MS analysis, a biophysical technique that has recently monitored the intrinsic GTPase activity of KRAS (169). The native mass spectrum of the purified complex revealed an equilibrium of molecular species (**Fig 3.1A**).

The KRAS•SOS^{cat} complexes contained a nucleotide-free KRAS and the ternary complex, KRAS•SOS^{cat}•KRAS-GTP-Mg^{2+} (active site•SOS^{cat}•allosteric site), comprised of one KRAS and KRAS bound to GTP. Based on previous NMR and spectroscopic results showing the low affinity of KRAS-GTP to the active site (153, 154), we presume KRAS-GTP is bound to the allosteric site of SOS^{cat}. The stoichiometry of this ternary complex is consistent with crystal structures (152). Ion mobility measurements, which report on the rotationally averaged collision cross-section (CCS), show the existence of different conformers populated by SOS^{cat}, which could be modeled with a minimum of three different Gaussian distributions (**Fig 3.1B, Fig 3.2 and Table 3.6**). A similar analysis of SOS^{cat} but in the absence of KRAS (**Fig 3.1C and Fig 3.2**) revealed a marked increase in the most compact conformers, which are depleted when KRAS is present (**Fig 3.1B**).

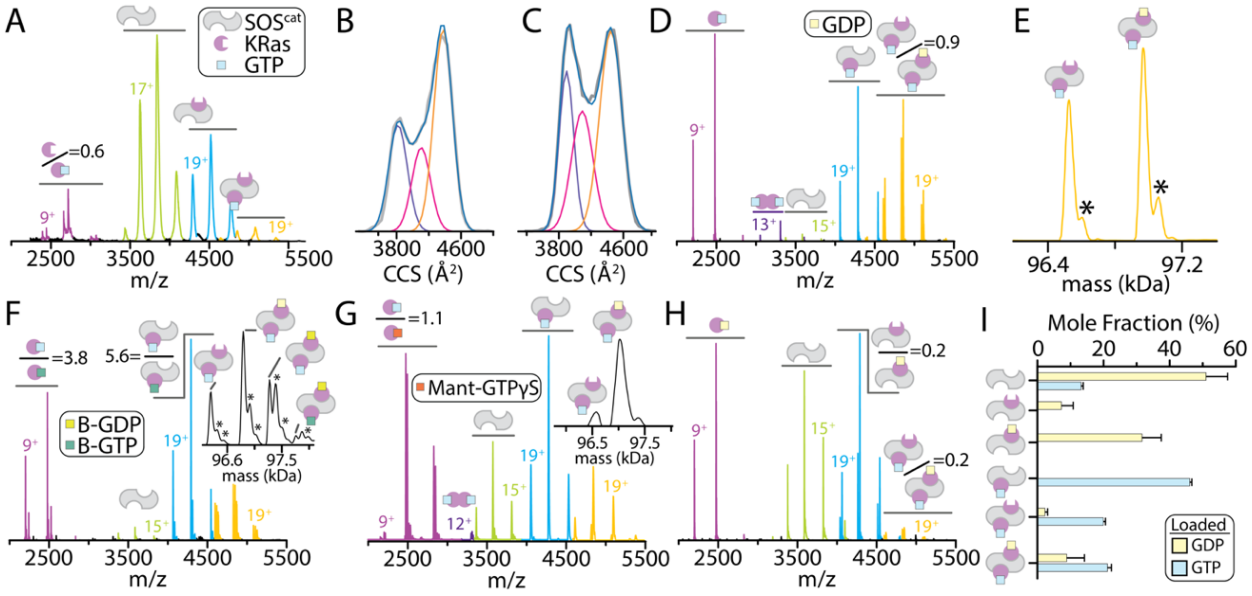

Figure 3.1. Conformational dynamics and molecular assemblies of SOS^{cat} and KRAS. (A) Native mass spectrum of 2 μM KRAS•SOS^{cat} complex purified by size exclusion chromatography. Mass spectral peaks corresponding to KRAS, SOS^{cat}, binary and ternary complexes are colored purple, chartreuse, cyan, and orange, respectively. (B) Collision cross section (CCS) distribution for the 16$^+$ ion of SOS^{cat} (blue lines). Regression (R^2 = 1.0) of three Gaussian peaks (purple, pink and orange lines) and their sum (grey line). (C) CCS profile for the 16$^+$ ion of SOS^{cat} recorded in the absence of KRAS. Shown as described in B. (D) Mass spectrum of 2 μM SOS^{cat} and 6 μM KRAS-GTP recorded immediately after mixing. (E) Deconvolution of mass spectrum in panel D and selected mass range corresponding to ternary complexes. Inorganic phosphate adducts are denoted by an asterisk. (F-G) Mass spectrum for the mixture described in D with the addition of (F) 2 μM BODIPY modified GTP (B-GTP) and (G) 5 μM Mant-GTP***γ***S. (H) Mass spectrum of 2 μM SOS^{cat} and 6 μM KRAS-GDP recorded immediately after mixing. (I) Plot of the mole fraction of SOS^{cat} complexes determined from deconvolution of mass spectra. Reported are the mean and standard deviation (n = 3). Mass spectra shown in panels D-H were acquired on an Exactive plus EMR Orbitrap mass analyzer. KRAS bound at active and allosteric sites are shown at top right and bottom left of the cartoon, respectively.

Table 3.6. CCS values for different conformers of SOS^{cat} determined from first-principle measurements. Reported are the mean and standard deviation (n = 3).

Conformer	CCS (Å, z = 16$^+$)	CCS (Å, z = 17$^+$)
1	3840 ± 20	3915 ± 22
2	4095± 21	4195 ± 5
3	4378 ± 2	4464 ± 10

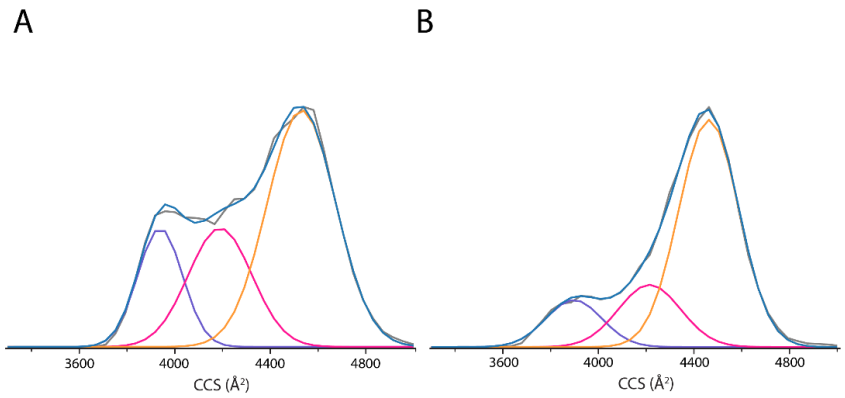

Figure 3.2. Conformational dynamics of SOS^{cat} captured by ion mobility spectrometry. Collision cross section plots (blue lines) of SOS^{cat} for 17^{+} charge state in the (A) absence and (B) presence of KRAS. Regression (R^2 = 1.0) of three Gaussian peaks (purple, pink and orange lines) and their sum (grey lines).

The lack of SOS^{cat} repopulating these conformers in the presence of KRAS is entirely consistent with the reported long-lived interconverting dynamical states of SOS^{cat} (156, 157). In another words, the observed depletion in SOS^{cat} conformers that preferentially engage KRAS could only happen if the different conformers have slow interconverting rates and long-lived states, which do not repopulate or equilibrate on the time scale of the experiment, hence their observed depletion in abundance. These findings provide additional evidence of conformational dynamics of SOS^{cat} and conformational selection for binding KRAS.

3.3.2. Molecular assemblies of KRAS-GTP and SOS^{cat}

To better understand the molecular assemblies of KRAS with SOS^{cat} in the presence of unmodified nucleotides, we conducted studies using a higher-resolution mass spectrometer (163). We first mixed SOS^{cat} with a three-fold molar excess of KRAS loaded with GTP (KRAS-GTP) (**Fig 3.3**).

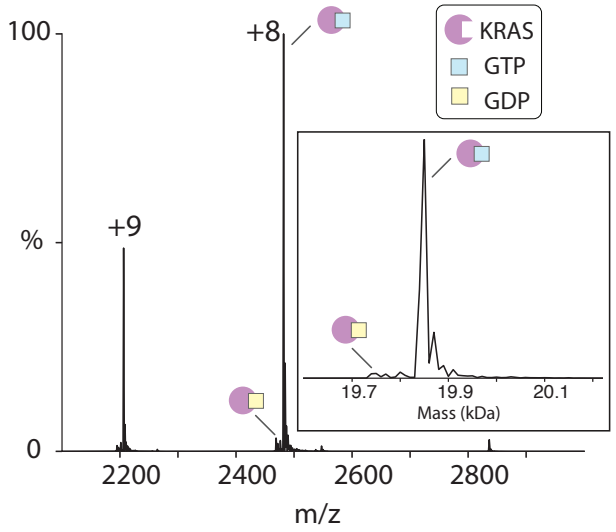

Figure 3.3. The low *m/z* region of the mass spectrum of KRAS-GTP complexed with SOS^{cat}. Deconvolution of the mass spectrum shows KRAS is predominantly loaded with GTP.The mass spectrum recorded immediately after mixing shows the presence of monomeric and dimeric KRAS bound to GTP, and a single binary complex composed of SOS^{cat}•KRAS-GTP-Mg^{2+} (**Fig 3.1D and I**). In addition, two ternary complexes of near equal abundance were measured corresponding to KRAS•SOS^{cat}•KRAS-GTP-$Mg^{2+}$$(GDP)_{0-1}$ (**Fig 3.1E**). The measured molecular weight of these complexes and of the proteins alone are in good agreement with theoretical values (**Table 3.7**). Notably, these molecular species were not resolved in the lower-resolution mass spectrum (**Fig 3.1A**). KRAS bound to GTP dominates the binary and ternary complexes, a result that is consistent with the higher affinity of KRAS-GTP to the allosteric site (153, 154). These findings capture an equilibrium of molecular assemblies formed between KRAS and SOS^{cat} that would be difficult to render using other biophysical techniques.

Table 3.7. Theoretical and measured masses for molecular assemblies of SOS^{cat} and KRAS and oncogenic mutants. The asterisk denotes Na^+ or Mg^{2+} adducts.

Detected ion	*Measured mass (Da)*	*Theoretical mass (Da)*	*Δ Da*
SOS^{cat}	57366.20	57369.84	3.64
SOS^{W729E}	57316.24	57312.74	3.5
$KRAS^{WT}$-GDP	19746.48	19746.00	0.48
$KRAS^{WT}$-GTP	19828.96	19825.98	2.98
SOS^{cat}•KRAS-GTP-Mg^{2+}	77222.31	77218.82	3.49
KRAS•SOS^{cat}•KRAS-GTP-Mg^{2+}	96530.23	96521.62	8.61
KRAS•SOS^{cat}•KRAS-GTP-Mg^{2+}-$H_2PO_4^-$	96612.12	96618.61	6.49
KRAS•SOS^{cat}•KRAS-GTP-$Mg^{2+}$$(GDP)_1$	96972.20	96964.82	7.38
KRAS•SOS^{cat}•KRAS-GTP-Mg^{2+}-$H_2PO_4^-$$(GDP)_1$	97060.15	97061.81	1.66
KRAS•SOS^{cat}	76673.41	76672.64	0.77
KRAS-GDP•SOS^{cat}	77117.63	77115.84	1.79
KRAS•SOS^{W729E}	76622.94	76615.54	7.4
KRAS-GDP•SOS^{W729E}	77064.33	77058.74	5.59
KRAS•SOS^{W729E}•KRAS-GTP-Mg^{2+}	96474.60	96464.52	10.08
KRAS•SOS^{W729E}•KRAS-GTP-$Mg^{2+}$$(GDP)_1$	96915.22	96907.72	7.5
SOS^{cat}•KRAS-B-GTP-Mg^{2+}	77582.43	77578.19	4.24
KRAS•SOS^{cat}•KRAS-GTP. $Mg^{2+}$$(B\text{-}GDP)_1$	97332.87	97324.00	8.87
KRAS•SOS^{cat}•KRAS-GTP-Mg^{2+}-$H_2PO_4^-$$(B\text{-}GDP)_1$	97413.92	97420.99	7.07
KRAS•SOS^{cat}•KRAS-B-GTP. $Mg^{2+}$$(B\text{-}GDP)_1$	97693.44	97683.37	10.07
$KRAS^{G13D}$•SOS^{cat}•$KRAS^{G13D}$-GTP-Mg^{2+}	96641.72	96639.84	1.88
$KRAS^{G13D}$•SOS^{cat}	76731.74	76731.84	0.1
$KRAS^{G13D}$•$SOS^{cat}$$(GDP)_1$	77179.58	77174.84	4.74
$KRAS^{G13D}$•SOS^{cat}•$KRAS^{G13D}$-GDP*	96555.17	96536.84	18.33
$KRAS^{G13D}$•SOS^{cat}•$KRAS^{G13D}$-GDP$(GDP)_1$*	96999.91	96979.84	20.07
$KRAS^{G13D}$•SOS^{W729E}	76674.91	76674.74	0.17
$KRAS^{G13D}$•SOS^{W729E}•$KRAS^{G13D}$-GTP-Mg^{2+}	96589.25	96582.74	6.51
$KRAS^{G13D}$•SOS^{W729E}	76671.86	76674.74	2.88
$KRAS^{G13D}$•$SOS^{W729E}$$(GDP)_1$	77117.28	77117.74	0.46
SOS^{cat}•$KRAS^{G12C}$-GTP-Mg^{2+}	77268.65	77263.84	4.81
$KRAS^{G12C}$•SOS^{cat}•$KRAS^{G12C}$-GTP-Mg^{2+}	96612.72	96611.84	0.88
$KRAS^{G12C}$•SOS^{cat}•$KRAS^{G12C}$-GTP-$Mg^{2+}$$(GDP)_1$	97056.77	97054.84	1.93
$KRAS^{G12C}$•SOS^{cat}	76721.45	76717.84	3.61
$KRAS^{G12C}$-GDP•SOS^{cat}	77167.11	77160.84	6.27
$KRAS^{G12C}$•SOS^{W729E}	76664.43	76660.74	3.69
$KRAS^{G12C}$-GDP•SOS^{W729E}	77111.28	77103.74	7.54
SOS^{W729E}•$KRAS^{G12C}$-GTP-Mg^{2+}	77205.00	77206.74	1.74
SOS^{cat}• $KRAS^{Q61H}$-GTP-Mg^{2+}	77225.82	77228.83	3.01
$KRAS^{Q61H}$-GDP•SOS^{cat}	77134.22	77125.83	8.39
SOS^{W729E}•$KRAS^{Q61H}$-GTP- Mg^{2+}	77178.71	77171.73	6.98

3.3.3. SOS^{cat} stimulates KRAS GTPase activity

Despite addition of KRAS-GTP to SOS^{cat}, an additional peak corresponding to KRAS•SOS^{cat} •KRAS-GTP-$Mg^{2+}$$(GDP)_1$ was detected with a measured mass (96972.2 ± 2.3 Da) in close agreement with the calculated mass (96964.8 Da) (**Table 3.7**). Mass selection of this ternary complex in the quadrupole followed by collision-induced dissociation (CID) further corroborates this assignment (**Fig 3.4**).

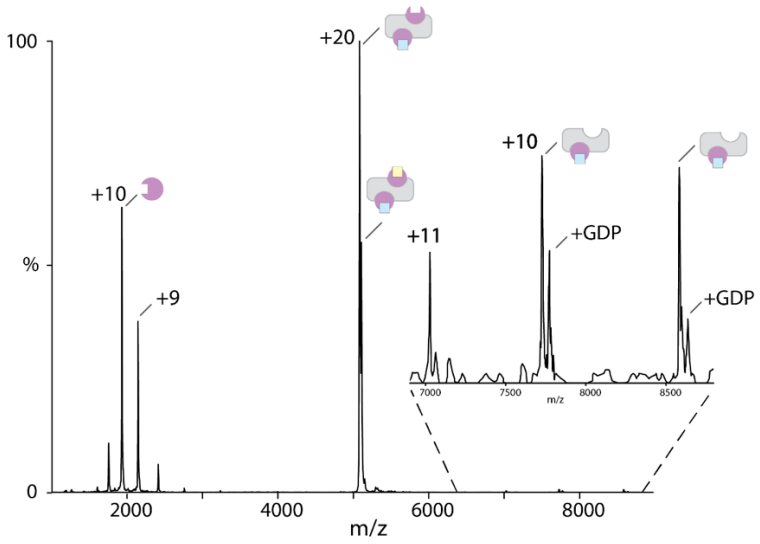

Figure 3.4. Mass spectrum of the ternary KRAS•SOS^{cat} •KRAS-GTP.$Mg^{2+}$$(GDP)_1$ complex post collisional activation. The 20^+ charge state of ternary complex was isolated and subsequently activated in the collision cell. The peaks at low *m/z* range correspond to KRAS apo and those in higher *m/z* range represent SOS^{cat}•KRAS-GTP-Mg^{2+} with a peak corresponding to bound GDP.

In addition, surface-induced dissociation (SID) of the isolated ternary complex resulted in dissociation of KRAS and KRAS-GTP from the complex (**Fig 3.5**). Notably, KRAS was loaded with GTP (~98%) (**Fig 3.3**) and the slow intrinsic GTP hydrolysis of KRAS in the absence of SOS^{cat} cannot account for the perplexing abundance of GDP.

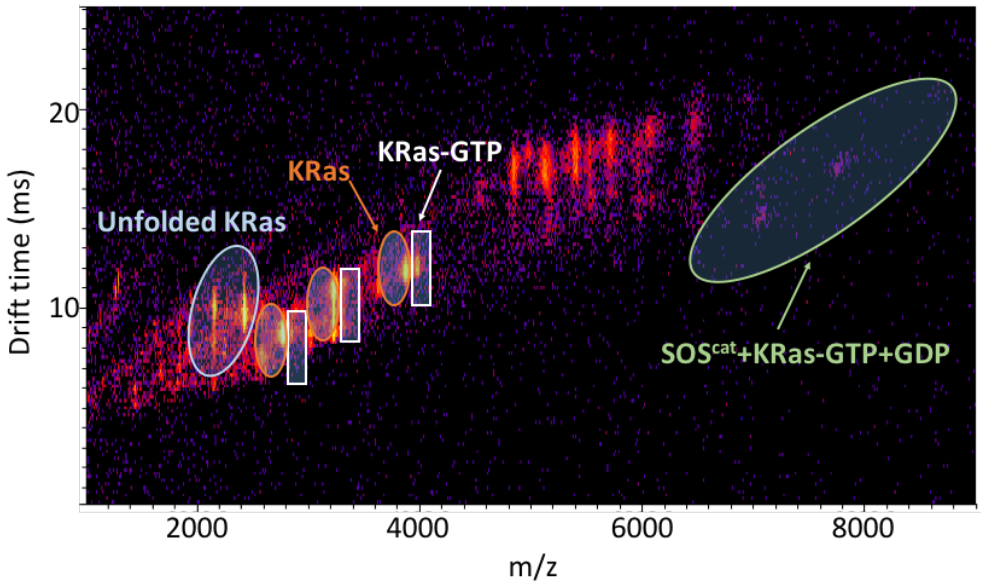

Figure 3.5. Surface-induced dissociation of the KRAS•SOS^{cat} •KRAS-GTP.Mg^{2+}(GDP) complex. The charge state distribution of ternary complex was selected in quadruple prior to surface induced dissociation. The dissociated species are labeled.

The appearance of GDP is most likely due to the GTPase activity of KRAS but stimulated by SOS^{cat}, which would result in production of GDP and inorganic phosphate ($H_2PO_4^-$). In crystal structures (152), phosphate is bound to ternary complexes and accordingly here phosphate adducts are observed on the complex with a measured mass of 97060.2 ± 2.1 Da compared to the theoretical mass of 97061.8 Da (**Fig 3.1E**). Moreover, incubation of a mixture of KRAS-GTP and SOS^{cat} overnight resulted in nearly two-fold greater levels of KRAS bound to GDP compared to the control solution containing only KRAS-GTP (**Fig 3.6**).

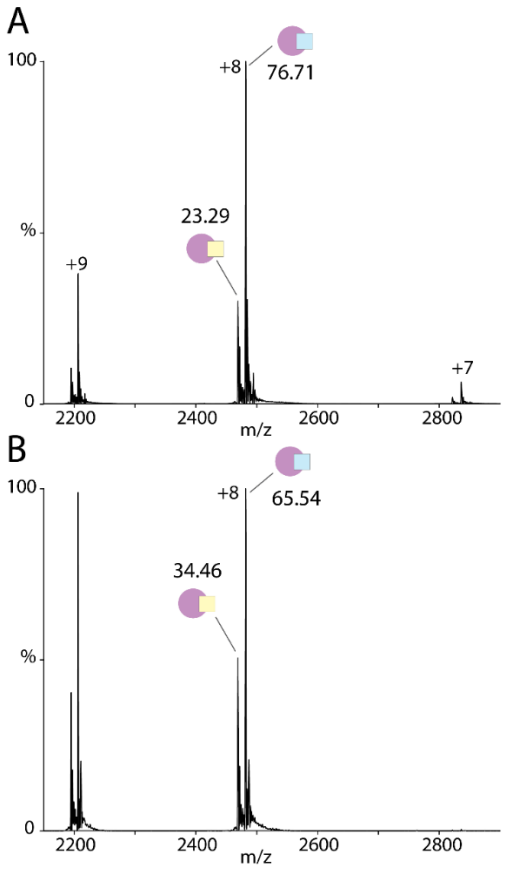

Figure 3.6. Native mass spectra of (A) KRAS-GTP and (B) KRAS-GTP in the presence of SOS^{cat} incubated at 4 °C for 22 hours. The mole fractions of KRAS bound GDP and GTP were determined after deconvoluting the mass spectra using Unidec (125). The low *m/z* range mass spectra show higher abundance of KRAS bound GDP for KRAS-GTP complexed with SOS^{cat} compared to KRAS-GTP alone shown in A.

An inorganic phosphate assay also corroborated these findings with higher phosphate concentration when KRAS-GTP is in the presence of SOS^{cat} compared to the control KRAS-GTP solution (**Table 3.8**). Taken together, these results indicate a role of SOS in stimulating the GTPase activity of KRAS.

Table 3.8. Inorganic phosphate (P_i) concentrations measured by malachite green assay for KRAS-GTP, SOS^{cat} and KRAS-GTP in complex with SOS^{cat}. Reported are the mean and standard deviation (n = 3).

	$[P_i]$ (μM)	
Complex	37.64 ± 0.79	-
KRAS-GTP	16.05 ± 0.87	-
SOS^{cat}	7.36 ± 0.28	-
$[P_i]'_{complex} = [P_i]_{complex} - [P_i]_{SOS^{cat}}$	30.28 ± 0.84	-
$[P_i]'_{complex}/[P_i]_{KRAS-GTP}$	-	1.88 ± 0.11

Additional evidence for stimulation of KRAS GTPase activity is offered by the use of GTP analogs. First, a BODIPY modified GTP (B-GTP) analog was added to an incubated mixture of KRAS-GTP and SOS^{cat} followed by recording the native mass spectrum. Multiple species are observed along with adducts corresponding to inorganic phosphate and B-GDP only bound to KRAS in complex with SOS^{cat} (**Fig 3.1F**). Interestingly, the lower abundance of KRAS•SOS^{cat} •KRAS-B-GTP.Mg^{2+}(B-GDP)$_1$ compared to KRAS•SOS^{cat} •KRAS-GTP-Mg^{2+}(B-GDP)$_1$ suggests the allosteric binding site is less dynamic than the active site (**Fig 3.1F, inset**). Next, the non-hydrolyzable GTP analog, Mant-GTPγS, was added to the incubated mixture of SOS^{cat} and KRAS-GTP. The native mass spectrum shows no detectable signal corresponding to hydrolyzed Mant-GDP, and Mant-GTPγS is only bound to free KRAS (**Fig 3.1G**). These findings show various molecular assemblies of KRAS and SOS^{cat} but also report that SOS^{cat} can stimulate of KRAS GTPase activity, a characteristic feature of GTPase activating proteins (GAPs) (151).

3.3.4. Molecular assemblies of KRAS-GDP and SOS^{cat}

As the degree of allosteric modulation of SOS^{cat} greatly depends on the nucleotide bound state of RAS (152, 154), KRAS was loaded with GDP (KRAS-GDP) prior to mixing with SOS^{cat}. The

native mass spectrum for this mixture is dominated by two binary complexes with the majority (~80%) bound to GDP (**Fig 3.1H and I**). In addition, there are low abundant signals corresponding to KRAS•SOS^{cat} •KRAS-GTP-$Mg^{2+}$$(GDP)_{0-1}$ that stem from a small fraction of KRAS-GTP not loaded with GDP (**Fig 3.7**), underscoring the sensitivity of our measurements. KRAS-GTP promotes the formation of a ternary complex, which is in accord with previous studies (152, 154).

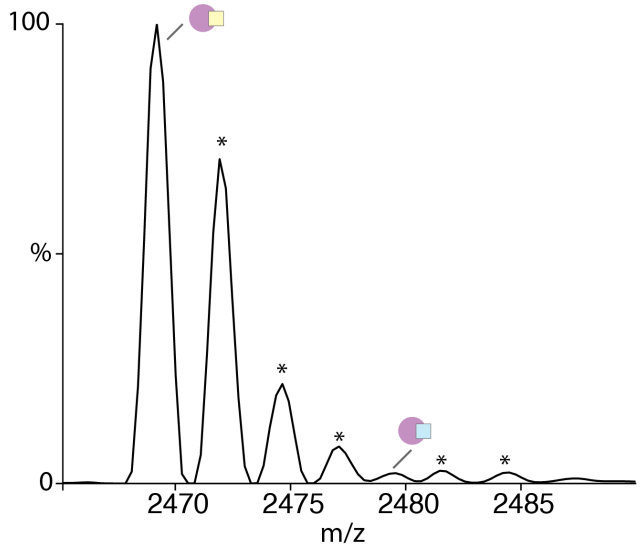

Figure 3.7. KRAS loaded with GDP shows the presence of a negligible fraction of GTP. Shown is a zoom of the 8^+ charge state with magnesium or sodium bound adducts denoted by an asterisk.

3.3.5. Molecular assemblies of SOS^{cat} and KRAS oncogenic mutants

Three oncogenic mutants of KRAS were selected based on their high occurrence in some cancers (Q61H, G13D, and G12C) (96). The mutant proteins were first loaded with GTP and mixed with SOS^{cat} immediately before native MS analysis. The mass spectrum for KRAS^{Q61H} and SOS^{cat} mixture showed a higher abundance of dimeric KRAS^{Q61H} with each bound to GTP and no detectable ternary complex (**Fig 3.8A and D**).

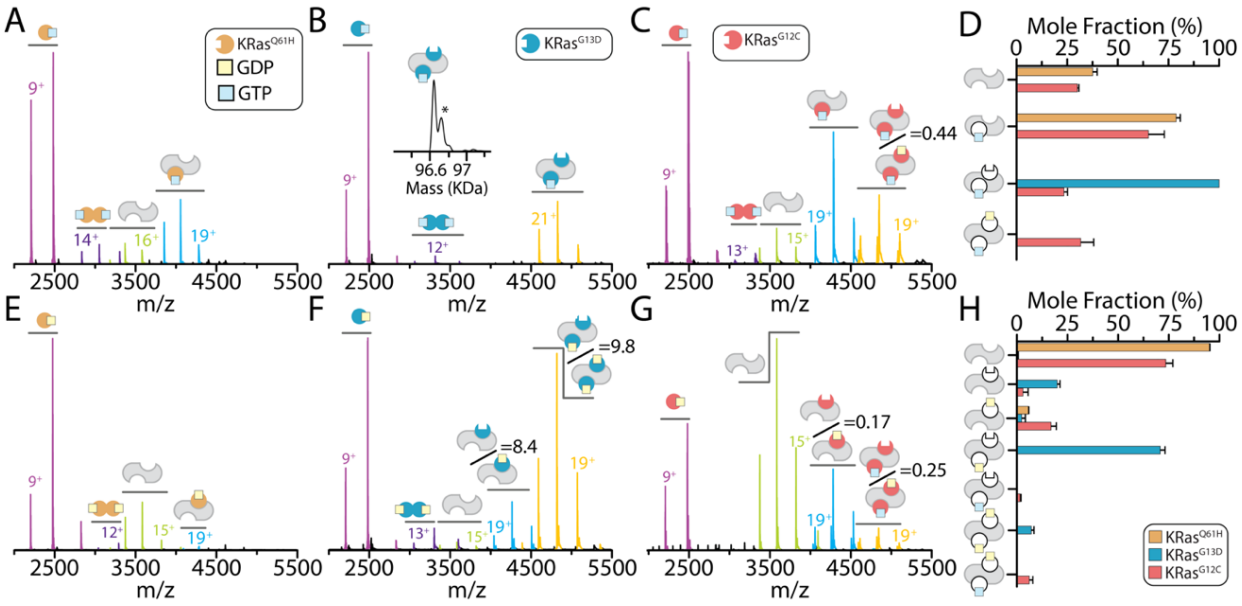

Figure 3.8. Distinct molecular assemblies of SOS^{cat} with oncogenic KRAS mutants. (**A-C**) Native mass spectra of 2μM SOS^{cat} mixed with three equivalents of (A) KRAS^{Q61H}-GTP, (B) KRAS^{G13D}-GTP or (C) KRAS^{G12C}-GTP. Mass spectra are shown as described in Figure 1. (**D**) Plot of the mole fraction of SOS^{cat} complexes formed with GTP loaded proteins. (**E-G**) Mass spectra of 2μM SOS^{cat} mixed with three-fold molar excess of (E) KRAS^{Q61H}-GDP, (F) KRAS^{G13D}-GDP or (G) KRAS^{G12C}-GDP. (**H**) Plot of the mole fraction of SOS^{cat} complexes formed with GDP-loaded proteins. Shown as described in Figure 1.

The SOS^{cat}•KRAS^{Q61H}-GTP-Mg^{2+} complex uniformly contained one GTP and no ternary complexes were observed (**Figure 3.8A and D**). In stark contRASt, KRAS^{G13D}-GTP solely formed a KRAS^{G13D}•SOS^{cat} •KRAS^{G13D}-GTP-Mg^{2+} complex (**Fig 3.8B and D**). The third GTP-loaded mutant KRAS^{G12C} engaged SOS^{cat} in a similar fashion as wild-type KRAS with the exception of an increased abundance of the ternary complex containing GDP (**Fig. 3.8C-D and Fig 3.9**). Of the three oncogenic mutants, GDP was observed only in SOS^{cat}•KRAS^{G12C} complexes. In summary, oncogenic mutants form assemblies with SOS^{cat} that are distinct from those formed with wild-type KRAS.

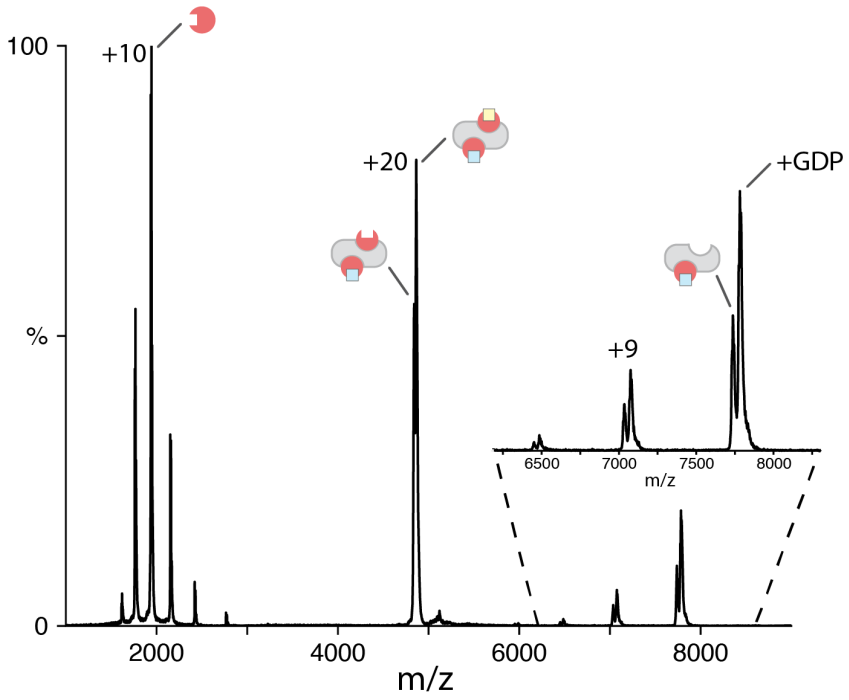

Figure 3.9. The representative mass spectrum for collisional activation of the ternary $KRAS^{G12C}$•SOS^{cat}•$KRAS^{G12C}$-GTP-$Mg^{2+}$$(GDP)_1$ complex. The 20^+ charge state of complex was isolated and subsequently activated in the collision cell. The peaks at low *m/z* range correspond to apo $KRAS^{G12C}$ and those in higher *m/z* range represent SOS^{cat}•$KRAS^{G12C}$-GTP.Mg^{2+} with a peak corresponding to bound GDP.

We next investigated the three oncogenic mutants loaded with GDP and their assembly with SOS^{cat}. The mass spectrum of a 3:1 mixture of $KRAS^{Q61H}$ to SOS^{cat} had weak signal for a GDP bound binary complex (**Fig 3.8E and H**). $KRAS^{G13D}$-GDP predominantly formed ternary complexes composed of $KRAS^{G13D}$•SOS^{cat}•$KRAS^{G13D}$-$GDP(GDP)_{0-1}$ with ~90% of the signal accounting for the complex bound to only one GDP (**Fig 3.8F and H**). This unexpected observation of a prevalent ternary complex for $KRAS^{G13D}$-GDP suggests it can bind the allosteric site and possibly function as an allosteric modulator of SOS^{cat}. Assembly of SOS^{cat} and $KRAS^{G12C}$-GDP led to the formation of complexes reminiscent of wild-type KRAS but overall lower in abundance (**Fig 3.8G and H**).

3.3.6. Complexes of KRAS with a mutant form of SOS^{cat}

SOS^{cat} containing the W729E mutation (SOS^{W729E}) has been reported to abolish RAS binding at the allosteric site (153). The mixture of KRAS-GTP and SOS^{W729E} showed a significant depletion of higher-order complexes (**Fig 3.10A and C**).

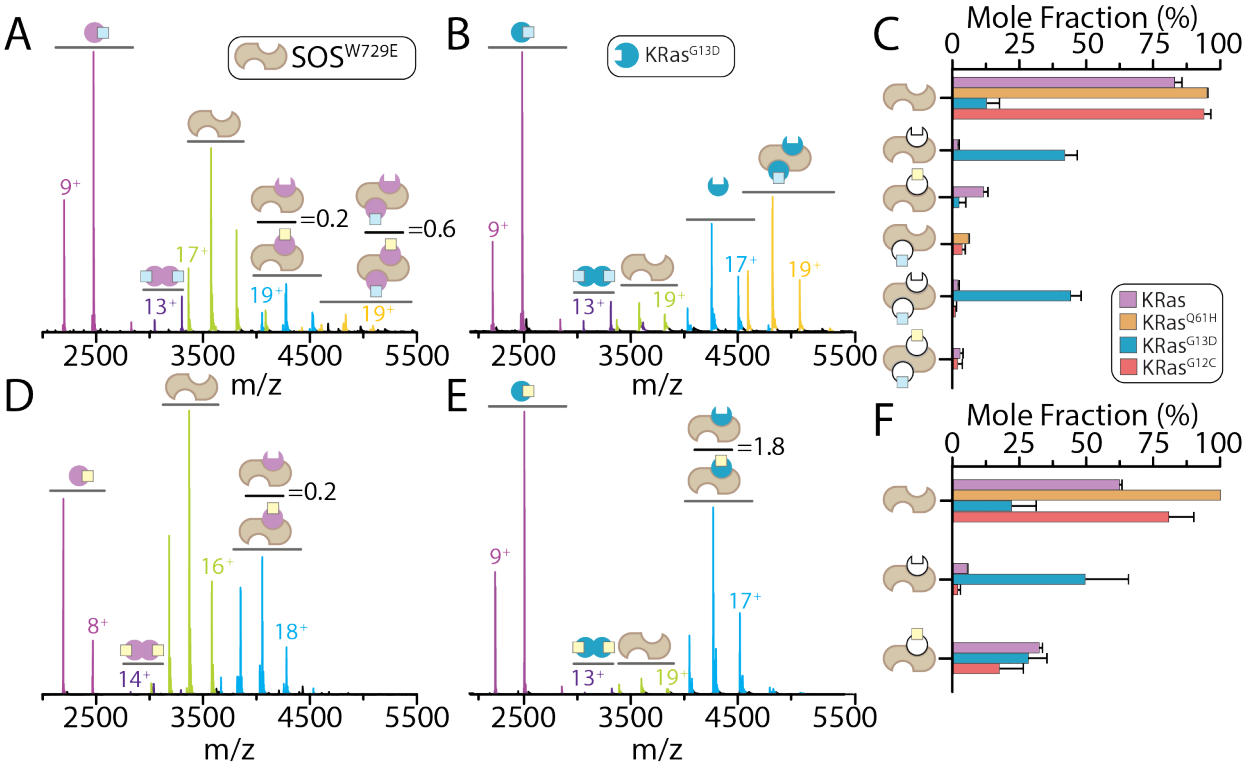

Figure 3.10. Complexes of a mutant form of SOS^{cat} with KRAS and oncogenic mutants. (**A-B**) Native mass spectra of 2 µM SOS^{W729E} mixed with 6µM of (A) KRAS-GTP or (B) KRAS^{G13D}-GTP. Mass spectra are shown as described in Figure 1. (**C**) Plot of the mole fraction of SOS^{W729E} complexes formed with GTP loaded proteins. Shown as described in Fig. 1. (**D-E**) Mass spectra for a 1:3 mixture of SOS^{W729E} with (D) KRAS-GDP or (E) KRAS^{G13D}-GDP. (**F**) Plot of the mole fraction of SOS^{W729E} complexes formed with GDP loaded proteins. Shown as described in Fig. 1.

Again, GDP is present in the ternary complex with a ratio skewed to those containing GDP. KRAS^{Q61H}-GTP and KRAS^{G12C}-GTP also displayed an overall reduction in complex formation (**Fig 3.10C and Fig 3.11**). Surprisingly, KRAS^{G13D}-GTP formed complexes composed of KRAS^{G13D}•SOS^{W729E} and KRAS^{G13D}•SOS^{W729E}•KRAS^{G13D}-GTP-Mg^{2+} (**Fig 3.10B and C**).

Moreover, SOS^{W729E} and KRAS-GDP formed two binary complexes, KRAS•$SOS^{W729E}(GDP)_{0-1}$, in the same ratio but lower in signal abundance compared to SOS^{cat} alone (**Fig 3.10D and F**). $KRAS^{G13D}$-GDP primarily assembled into binary complexes with a majority (~64%) containing nucleotide-free $KRAS^{G13D}$ (**Fig 3.10E and F**). $KRAS^{G12C}$•$SOS^{W729E}(GDP)_{0-1}$ complexes were observed for the assembly of $KRAS^{G12C}$-GDP and SOS^{W729E}, and $KRAS^{Q61H}$-GDP did not engage SOS^{W729E} (**Fig 3.10F and Fig 3.11**). Taken together, these results demonstrate a clear preference for the active site of SOS^{cat} toward KRAS-GDP.

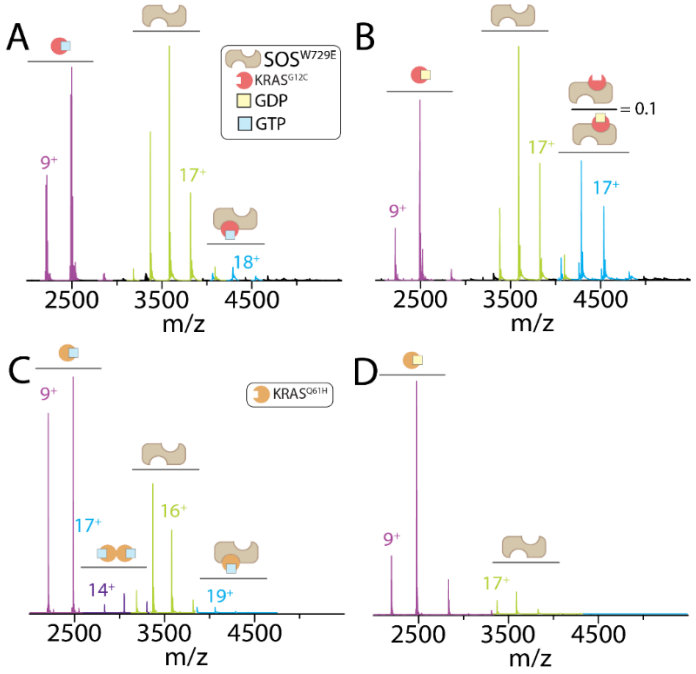

Figure 3.11. Complexes of SOS^{cat} mutant with KRAS and oncogenic mutants. (A-D) Native mass spectra of 2 µM SOS^{W729E} mixed with 6 µM of (A) $KRAS^{G12C}$-GTP, (B) $KRAS^{G12C}$-GDP, (C) $KRAS^{Q61H}$-GTP and (D) $KRAS^{Q61H}$-GDP.

3.3.7. Structural characterization of the $KRAS^{G13D}$-GTP and SOS^{cat} ternary complex

The unique properties of $KRAS^{G13D}$ to form predominantly ternary complexes with SOS^{cat} prompted us to determine the structure using cryo-electron microscopy. The ternary complex was

prepared using KRAS^{G13D} loaded with 5'-Guanylyl imidodiphosphate (GppNp), a non-hydrolyzable analog of GTP (**Fig 3.12**).

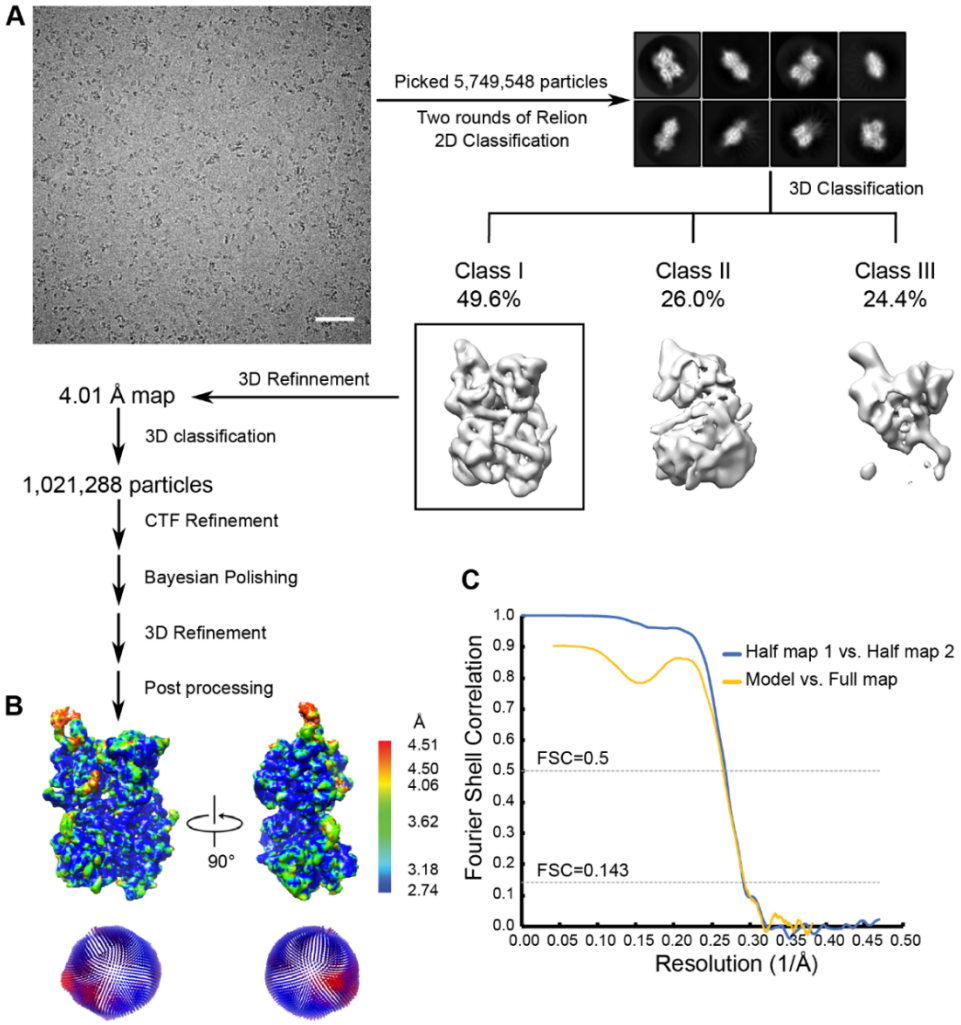

Figure 3.12. Single-particle cryo-EM analysis for the KRAS^{G13D}•SOS^{cat} complex. (A) The workflow of data processing. The data was acquired at the National Center for CryoEM Access and Training (NCCAT) using a Titan Krios electron microscope operating at 300 KV. Initial motion correction was carried out using MotionCor2 (173). A representative micrograph is shown along with a scale bar corresponding to 50 nm. The following steps were performed in Relion (175). Representative 2D class averages are shown, with the box edge corresponding to 170 Å. After disposing contamination and poorly-aligned 2D classes, three maps were resolved using 3D classification. Subsequent refinement and polishing were performed on the best 3D class. (B-C) Fourier shell correlation curves of the half map 1 versus the half map 2 (blue), and the refined model versus the overall map (yellow). The resolution of the reconstruction was determined by the FSC=0.143 criterion.

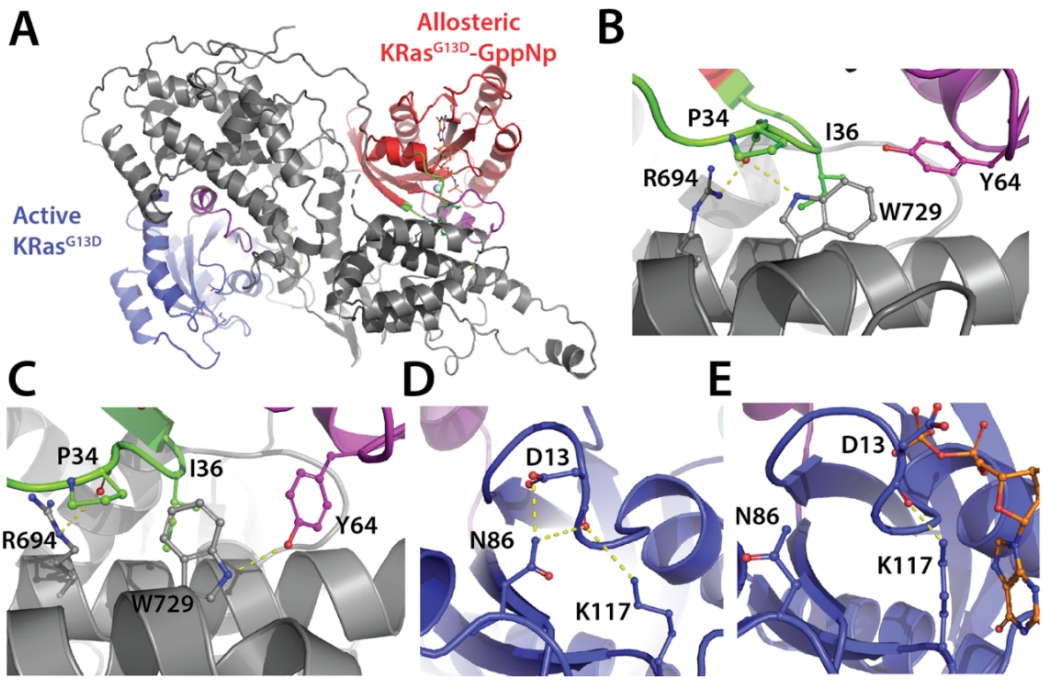

Figure 3.13. Structure of KRAS^{G13D} in complex with SOS^{cat}. (**A**) The structure is shown in carton representation with KRAS^{G13D} molecules bound at the active and allosteric sites of SOS^{cat} (grey) are colored blue and red, respectively. Switch I and II regions of KRAS^{G13D} are colored in green and purple, respectively. Allosteric KRAS^{G13D} is bound to GppNp and magnesium. (**B**) Molecular interactions formed at the interface between KRAS^{G13D}-GppNp and SOS^{cat}. Hydrogen bonds are shown as yellow dashed lines. (**C**) The allosteric interface for HRAS-GppNp and SOS^{cat} (PDB 1NVW) (152) shown in similar orientation as panel B. (**D**) KRAS^{G13D} bound at the active site with Asp13 forming interactions with Asn86 and K117. (**E**) X-ray structure of KRAS^{G13D} bound to GDP (PDB 6E6G) (179) shows the sidechain of Asp13 is oriented in the opposite direction, away from Asn86.

The structure of the complex was determined to a resolution of 3.47 Å (see SI methods) with KRAS^{G13D} and KRAS^{G13D}-GTP bound at the active and allosteric sites of SOS^{cat}, respectively (**Fig 3.13A and Fig 3.14**).

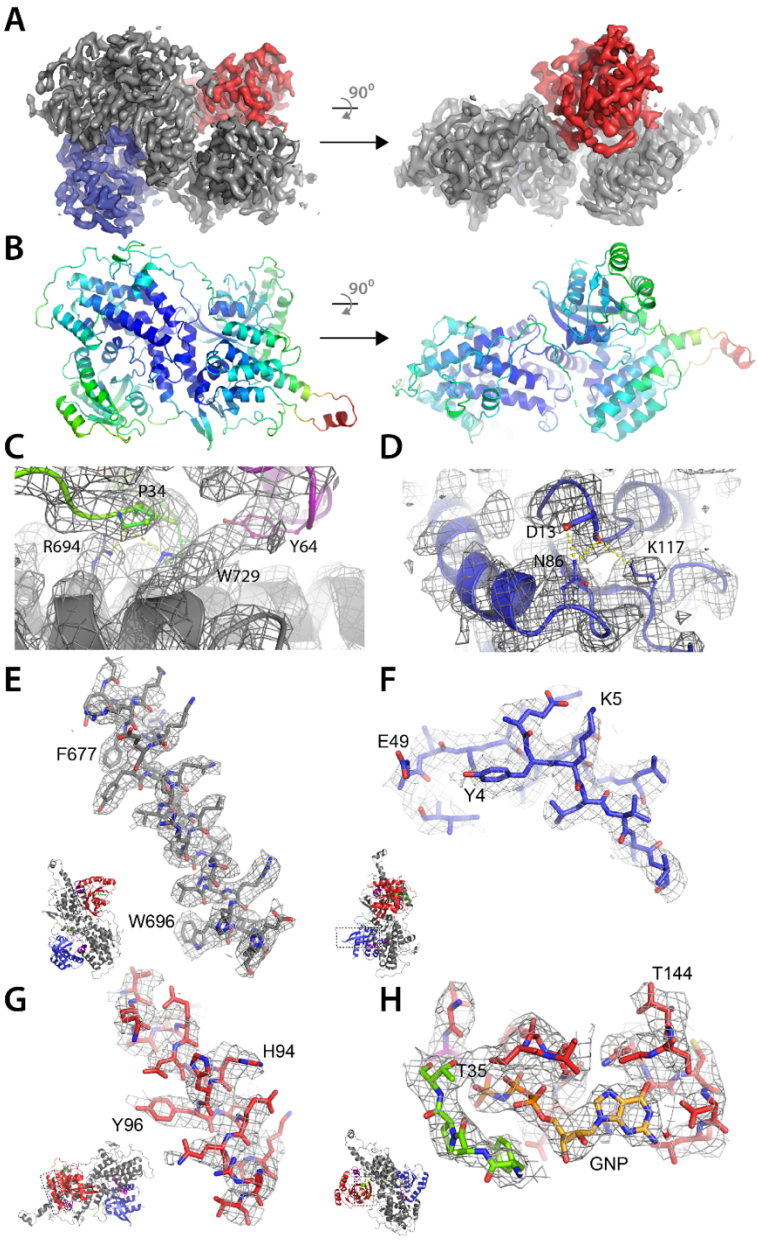

Figure 3.14. Atomic model of the ternary KRAS^{G13D}•SOS^{cat} complex and the cryoEM density. (A) The cryoEM density map of the overall structure contoured at 6 rmsd. Density corresponding to KRAS^{G13D} molecules bound at the active and allosteric sites of SOS^{cat} (grey) are colored blue and red, respectively. (B) The structure shown in cartoon representation and color-coded by B-factor, ranging from 22 (dark blue) to 142 (red) Å^2. Selected regions along with density map are shown: (C-D) KRAS^{G13D} molecules bound at the allosteric and active sites of SOS^{cat}, respectively; (E) an α-helix of SOS^{cat}, contour level 5.0 rmsd; (F) a β-sheet of KRAS^{G13D} at the active site, contour level 5.0 rmsd; (G) an α-helix of KRAS^{G13D} at the allosteric site, contour level 5.0 rmsd; and (E) GppNp (GNP) of KRAS^{G13D} at the allosteric site, contour level 6.0 rmsd.

The presence of nucleotide-free $KRAS^{G13D}$ at the active site is in line with MS results (**Fig 3.8B**). The structure is largely reminiscent with that of HRAS•SOS^{cat} •HRAS-GppNp (PDB 1NVW) with some notable structural differences, such as a ~2.5 Å displacement of the $KRAS^{G13D}$ molecule at the active site (**Fig 3.15E-F**). Analysis of $KRAS^{G13D}$-GTP bound at the allosteric site reveals that $KRAS^{G13D}$ adopts a state 2 conformation, characterized by interaction of the γ-phosphate with the side chain of Thr35 within switch I and the amide of Gly60 within switch II (**Fig 3.15B**) (180). Moreover, the structure of $KRAS^{G13D}$-GppNp bound at the allosteric site of SOS^{cat} aligns well with that of active conformation of HRAS-GTP (**Fig 3.15C**) (180). However, the molecular interactions of $KRAS^{G13D}$-GTP bound at the allosteric site of SOS^{cat} differs from that observed for SOS^{cat} in complex with HRAS-GTP. More specifically, the side chain of tryptophan at position 729 of SOS^{cat} is reoriented and interacting with the carbonyl of Pro34 of $KRAS^{G13D}$ (**Fig 3.13A and B**). This orientation is similar to the crystal structure of the Tyr64A mutant of HRAS bound at the allosteric site of SOS^{cat} (**Fig 3.15D**), which this mutant HRAS protein has significantly reduced binding affinity to the active site of SOS^{cat} (181). Trp729 adopts a different orientation that interacts with Try64 in the structure of HRAS-GppNp bound at the allosteric site of SOS^{cat} (**Fig 3.13C**).

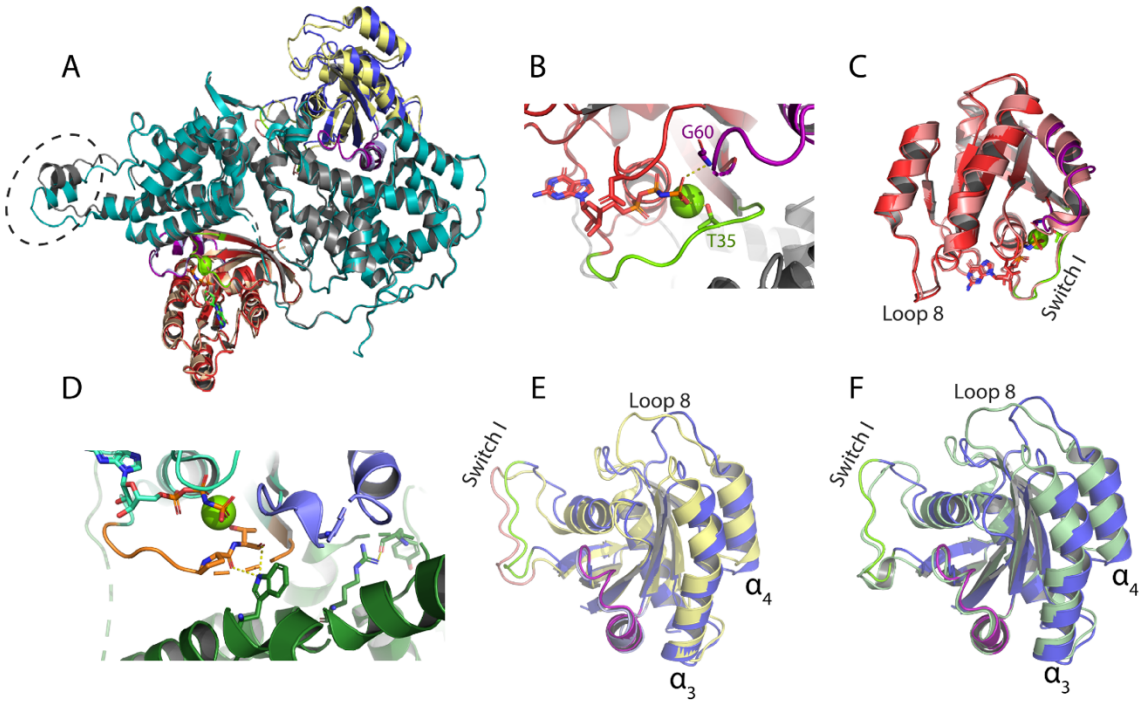

Figure 3.15. Comparison of the structure of KRAS^{G13D} in complex with SOS^{cat} to other structures. (A) Superimposition of the KRAS^{G13D} ternary structure with the crystal structure of H-RAS-GppNp in complex with SOS^{cat} (PDB id: 1NVW) yielding an RMSD of 2.5 Å. The KRAS^{G13D} is shown as in figure 4. For the HRAS complex, SOS^{cat} is colored cyan (SOS^{cat}), the active site yellow, and allosteric site wheat. A notable shift in the α3 and α4 helices by ~2.5 Å. (B) The interaction of Thr35 and Gly60 residues with the phosphate of GppNp bound to KRAS^{G13D}. (C) Alignment of KRAS^{G13D}-GTP with HRAS-GppNp (PDB 3K8Y). (D) Molecular interactions of HRAS-GppNp (PDB id: 1NVV) at the allosteric site of SOS^{cat}. (E-F) Superimposition of KRAS^{G13D} bound at the active site with (E) HRAS and (F) KRAS^{G12C} (PDB 6EPP).

The density for residues 62-67 within the switch II region was not clear, possibly due to this region populating different conformations. The most marked difference in the structure of the KRAS^{G13D} in complex with SOS^{cat} compared to other available structures (152, 160) is the structure of KRAS^{G13D} bound at the active site (**Fig 3.13D**). Aspartic acid at position 13 forms hydrogen bonds with Asn86 and Lys117. These interactions, for example, reposition loop 8 by ~4 Å compared to HRAS in complex with SOS^{cat} along with displacing other regions, such as helices 3 and 4, p-loop and switch I (**Fig 3.13D and Fig 3.15E**). The observed conformation of KRAS^{G13D} also differs from

the structure of a mutated form of $KRAS^{G12C}$ bound only at the active site of SOS^{cat} (**Fig 3.15F**). Comparison of the $KRAS^{G13D}$-GDP structure (PDB 6E6G) with $KRAS^{G13D}$ bound at the active site reveals the sidechain of Asp13 is rotated 180 degrees and pointing away from Asn86 (**Fig 3.13E**).

3.3.8. The modulation of SOS^{cat} activity by $KRAS^{G13D}$-GTP

Competition and nucleotide exchange assays were conducted to better understand the significance of the interaction between $KRAS^{G13D}$ and SOS^{cat}. First, the complex formed between SOS^{cat} with GTP-loaded KRAS harboring the N-terminal hexa-histidine affinity tag (His_6-KRAS-GTP) displayed similar abundances of molecular species as the tag-less protein (**Fig 3.16A**).

Interestingly, addition of $KRAS^{G13D}$-GTP to this complex not only completely abolished the binding of wild-type KRAS to SOS^{cat} but predominantly formed a ternary complex of $KRAS^{G13D}$•SOS^{cat} •$KRAS^{G13D}$-GTP-Mg^{2+} (**Fig 3.16B**). The experiment performed in the opposite fashion, where His_6-KRAS-GTP is added to preformed complexes of $KRAS^{G13D}$-GTP and SOS^{cat}, resulted in no disruption of $KRAS^{G13D}$•SOS^{cat} complexes (**Fig 3.17**).

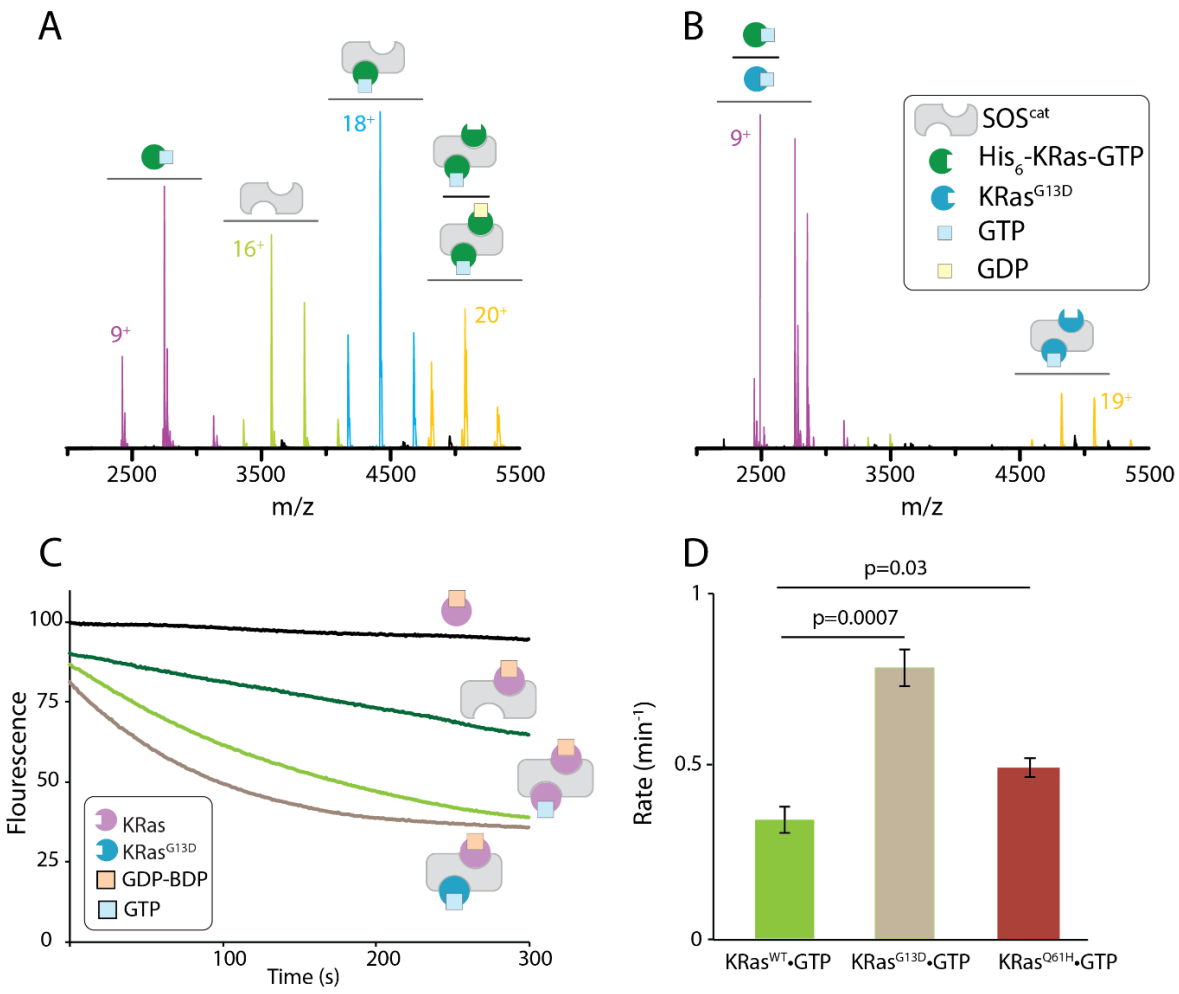

Figure 3.16. Competition and cross-activation of KRAS^{G13D}-GTP. (**A**) Native mass spectrum of 1 µM SOS^{cat} in complex with 3 µM His$_6$-KRAS-GTP. (**B**) Native mass spectrum after adding KRAS^{G13D}-GTP to the mixture in A to a final concentration of 3 µM. Mass spectra are shown as described in Figure 1. (**C**) Intrinsic (black line) and SOS^{cat}-mediated (dark green line) nucleotide exchange of KRAS loaded with B-GDP. The addition of KRAS-GTP (light green line) or KRAS^{G13D}-GTP (brown line) to a mixture of KRAS-B-GDP and SOS^{cat} accelerates the nucleotide exchange rate. (**D**) Nucleotide exchange rates determined for data presented in panel C. The SOS^{cat}-mediated nucleotide exchange rate in the presence of KRAS^{Q61H}-GTP is also provided. Reported are the mean and standard deviation from three independent experiments.

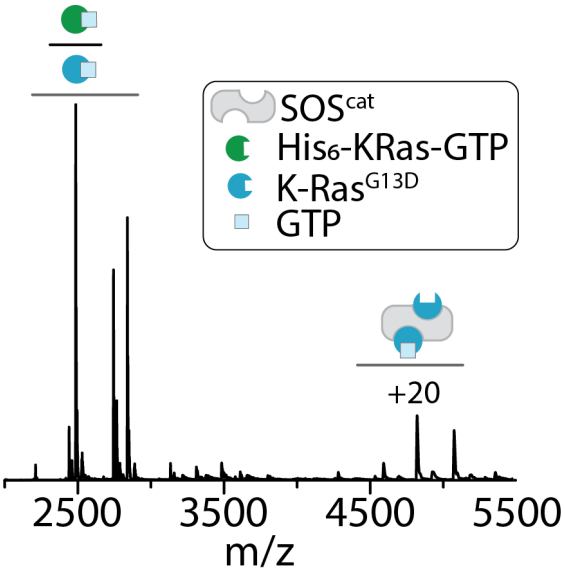

Figure 3.17. KRAS does not dissociate KRAS^{G13D} bound at either the allosteric and active site of SOS^{cat}. The addition of His_6-KRAS (3 μM final concentration) to pre-incubated mixture of 1 μM SOS^{cat} and 3 μM KRAS^{G13D}-GTP.

Next, the SOS^{cat}-stimulated nucleotide exchange rate of KRAS bound to B-GDP in the absence and presence of KRAS^{G13D}-GTP was determined. The intrinsic nucleotide exchange rate of KRAS-B-GDP is slow (182) (k = 0.12 min^{-1}) but enhanced in the presence of SOS^{cat} (**Fig 3.16C**). The rate of nucleotide exchange is allosterically modulated (k = 0.3 min^{-1}) in the presence of KRAS-GTP (**Fig 3.16C and D**) consistent with previous studies (152). However, the addition of KRAS^{G13D}-GTP increased the exchange rate by more than two-fold, k = 0.7 min^{-1} (**Fig 3.16C and D**). The addition of KRAS^{Q61H}-GTP (k = 0.4 min^{-1}) marginally increased the nucleotide exchange rate compared to KRAS-GTP and much less than KRAS^{G13D}-GTP. Attempts to measure SOS^{cat}-mediated nucleotide exchange rate of KRAS^{G13D} in the presence of allosteric KRAS^{G13D}-GTP was not possible due to extremely fast nucleotide exchange rate of this mutant protein consistent with previous studies (155). In short, KRAS^{G13D} exhibits not only a higher affinity for SOS^{cat} but is also a more potent allosteric modulator of SOS^{cat} activity.

3.3.9. Disruption of the interaction between KRAS and SOS^{cat}

As the disruption of the interaction between RAS and SOS is an attractive approach to curb aberrant RAS signaling (159, 183), we next investigated whether small molecule RAS•SOS disruptors can efficiently disrupt complexes of SOS^{cat} and KRAS mutants. Recent traction has been made on the development of specific covalent inhibitors of KRAS^{G12C}, such as ARS-1620 (158, 184). Reacting ten equivalents of ARS-1620 with KRAS^{G12C} loaded with either GTP or GDP showed complete reactivity when the enzyme is bound to GDP and limited reactivity when GTP is bound (**Fig 3.18**).

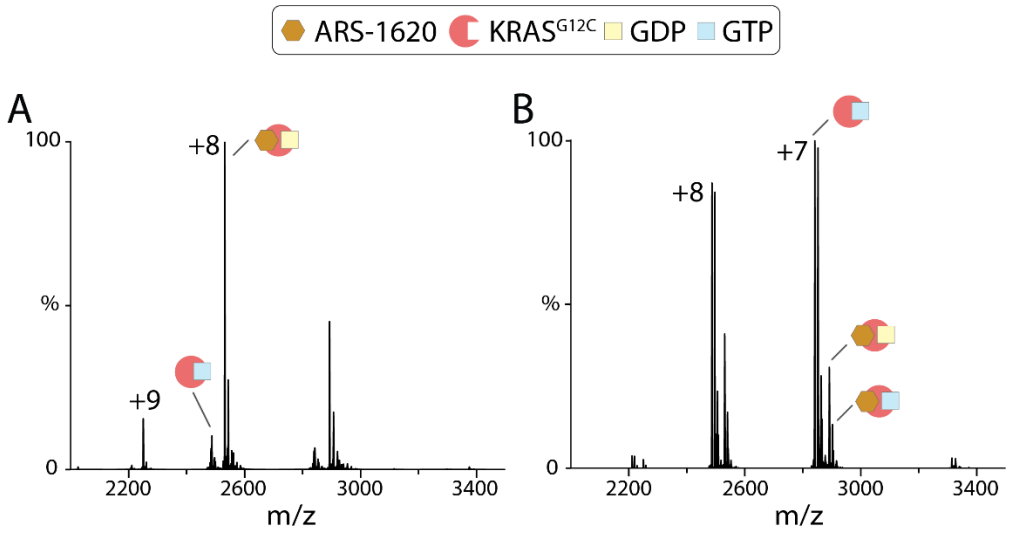

Figure 3.18. The specificity of ARS-1620 towards the inactive state of KRAS^{G12C}. The native mass spectra recorded for 10 µM ARS-1620 mixed with 3 µM (A) KRAS^{G12C}-GDP or (B) KRAS^{G12C}-GTP.

These results agree with the specificity of ARS-1620 toward the inactive, GDP bound state of KRAS^{G12C}. Moreover, the addition of ARS-1620 to an incubated mixture of SOS^{cat} and KRAS^{G12C}-GDP resulted in complete disruption of complexes (**Fig 3.19A**), consistent with a SOS-mediated nucleotide exchange assay (184). However, ARS-1620 added to a pre-incubated mixture of SOS^{cat}

and KRAS^{G12C}-GTP had no appreciably disruption of binary and ternary complexes (**Fig 3.19E**). This result suggests KRAS^{G12C}-GTP allosterically modulates the affinity of KRAS^{G12C} at the active site of SOS^{cat} thereby hindering the reactivity of ARS-1620. These findings highlight the inability of ARS-1620 to disrupt assemblies of SOS^{cat} and KRAS^{G12C}-GTP.

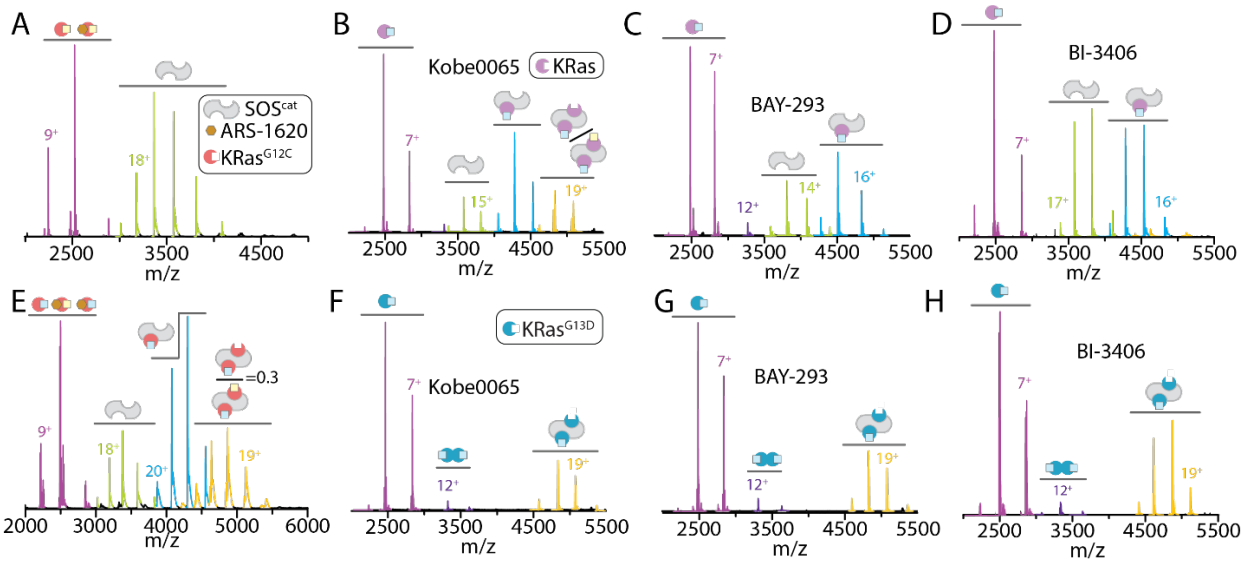

Figure 3.19. The effect of ARS-1620, BAY-293 and Kobe0065 on assemblies of KRAS and SOS^{cat}. (**A-E**) Mass spectrum recorded after adding 10 μM ARS-1620 to preincubated mixtures of 1 μM SOS^{cat} with 3 μM (A) KRAS^{G12C}-GDP and (E) KRAS^{G12C}-GTP. Mass spectra are shown as described in Figure 1. (**B-F**) Mass spectrum recorded after adding 2.5 μM Kobe0065 to preincubated mixtures of 1 μM SOS^{cat} with 3 μM (B) KRAS-GTP and (F) KRAS^{G13D}-GTP (**C-G**) Mass spectrum recorded after adding 2.5 μM BAY-293 to preincubated mixtures of 1 μM SOS^{cat} with 3 μM (C) KRAS-GTP and (G) KRAS^{G13D}-GTP. (**D-H**) Mass spectrum recorded after adding 2.5 μM of BI-3406 to pre-incubated mixtures of 1 μM SOS^{cat} with 3 μM (D) KRAS-GTP and (H) KRAS^{G13D}-GTP.

We next tested the efficacy of small molecule RAS•SOS disruptors, Kobe0065 (IC_{50}=20 μM), BAY-293 (IC_{50}=21 nM) and BI-3406 (IC_{50}=5 nM) (160, 161, 185). Kobe0065 binds directly to RAS-GTP and is reported to alter the binding at the allosteric site of SOS (185). The addition of 2.5 equivalents of Kobe0065 to SOS^{cat} in complex with KRAS-GTP or KRAS^{G13D}-GTP resulted in marginal and no disruption, respectively (**Fig 3.19B and F**). Increasing the concentration of

Kobe0065 to 200 µM, ten times the reported IC_{50} value, did not disrupt binary and ternary complexes. In addition, the small molecule was ineffective at disrupting complexes of $KRAS^{G12C}$ and SOS^{cat} (**Fig 3.20C**).

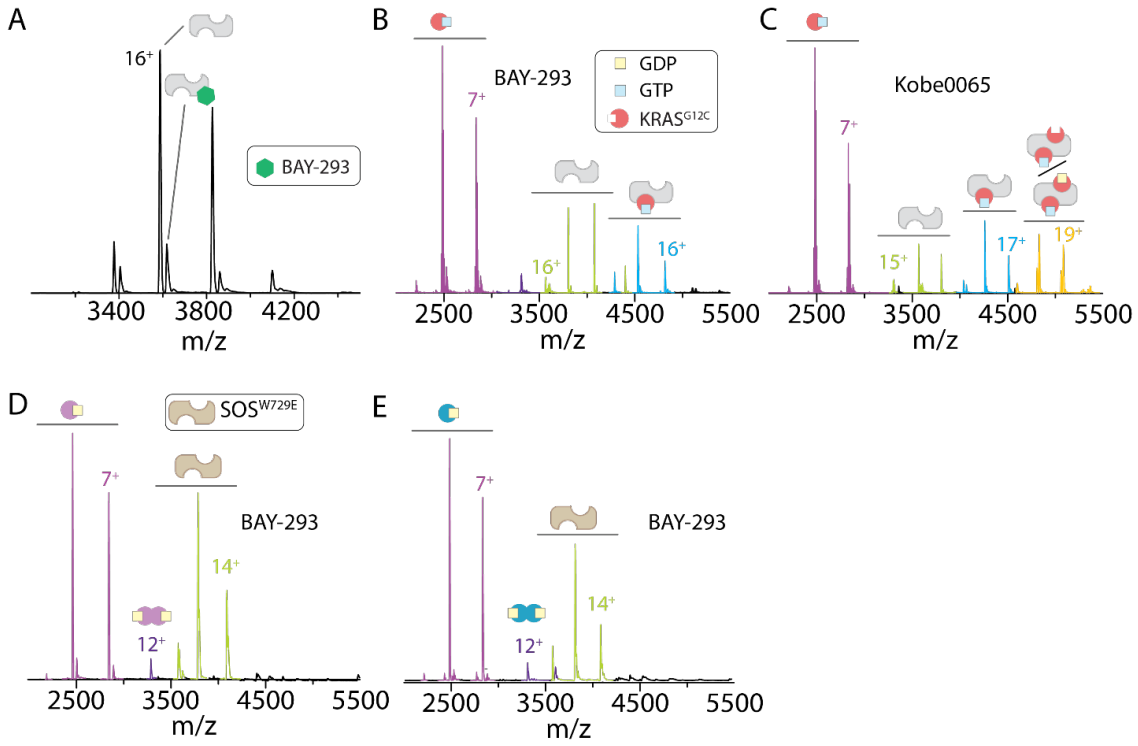

Figure 3.20. Kobe0065 does not disrupt the complexes of SOS^{cat} with $KRAS^{G12C}$. (A) Native mass spectrum of 2 µM SOS^{cat} and 10 µM of BAY-293. (B-C) The addition of (B) BAY-293 or (C) Kobe0065 at final concentration of 2.5 µM to a pre-incubated mixtures of 1 µM SOS^{cat} and 3 µM $KRAS^{G12C}$-GTP. The addition of 2.5 µM BAY-293 to a pre-incubated mixtures of 1 µM SOS^{W729E} with 3 µM of (D) KRAS-GTP or (E) $KRAS^{G13D}$-GDP.

BAY-293 has been shown to efficiently disrupt the interaction between $KRAS^{G12C}$ and SOS^{cat} leading to antiproliferative activity (160). However, the small molecule was not effective at disrupting the binding of KRAS-GTP and $KRAS^{G12C}$-GTP at the allosteric site of SOS^{cat} (**Fig 3.19C and Fig 3.20B**). BAY-293 binds directly to SOS^{cat} (**Fig 3.20A**) and disrupts the ternary complexes formed between SOS^{cat} and KRAS or $KRAS^{G12C}$ (**Fig 3.19C and Fig 3.20B**). Moreover, BAY-293 did not disrupt the ternary complex of $KRAS^{G13D}$-GTP and SOS^{cat} (**Fig**

3.19G). The compound, however, does inhibit the formation of complexes formed between SOS^{W729E} and either KRAS-GDP or $KRAS^{G13D}$-GDP (**Fig 3.20D and E**). BI-3406 (161), a recently reported highly selective and potent inhibitor of SOS1, was screened for the ability to disrupt complexes formed between SOS^{cat} and wild-type and mutants of KRAS. At 2.5 µM, BI-3406 binds directly to SOS^{cat} (**Fig 3.21A**) and disrupts the ternary complex between SOS^{cat} and KRAS (**Fig 3.19D**). In contRASt, BI-3406 at the same concentration did not disrupt the ternary $KRAS^{G13D}$•SOS^{cat} complex (**Fig 3.19H**), even after overnight incubation (**Fig 3.21B**). At higher concentrations of the compound (4000-fold the reported IC_{50}), the ternary complex between $KRAS^{G13D}$ and SOS^{cat} was almost completely disrupted (**Fig 3.21C**). Similar to BAY-293, BI-3406 disrupts the binary complex between $KRAS^{G13D}$-GDP and SOS^{W729E} (**Fig 3.21D**).

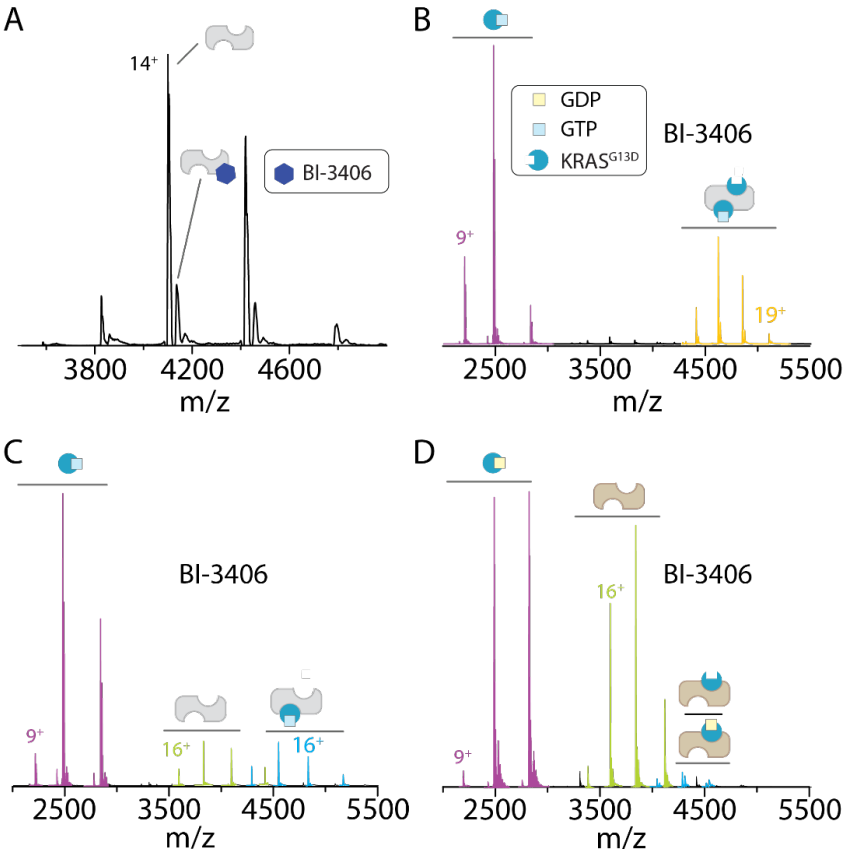

Figure 3.21. BI-3406 interaction with SOS^{cat} and SOS^{W729E}:$KRAS^{G13D}$-GDP and SOS^{cat}:$KRAS^{G13D}$-GTP complexes. (A) Native mass spectrum of 1 µM SOS^{cat} and 5 µM of BI-3406. (B-C) The mass spectra of (B) 2.5 µM and (C) 20 µM BI-3406 added to a complex of 1 µM SOS^{cat} and 3 µM $KRAS^{G13D}$-GTP and incubated overnight at 4 °C. (D) Addition of 2.5 µM BI-3406 to a pre-incubated mixture of 1 µM SOS^{W729E} and 3 µM $KRAS^{G13D}$-GDP.

3.4. Discussion

Dynamics of signaling proteins play crucial roles in their function (186). Although conformational heterogeneity has been reported for SOS^{cat} (156, 157), ion mobility measurements provide direct experimental evidence of the protein populating at least three conformers in solution with distinct conformers engaging KRAS. If the dynamics were fast, the depleted conformers that engage with KRAS would be repopulated. Instead, depletion of specific conformers in the presence of KRAS is in direct agreement with the long-lived, interconverting dynamical nature of SOS^{cat} (156, 157). To the best of our knowledge, this is the first demonstration of ion mobility showing clear evidence of conformational selection for a protein-protein interaction.

Native mass spectrometry provides a unique opportunity to monitor the molecular assemblies of SOS^{cat} with RAS. Unlike other approaches, the sensitivity and resolution of modern mass spectrometers enable not only measurements of proteins at low micromolar concentration but use of unmodified nucleotides. Native mass spectra resolve a number of molecular assemblies formed between KRAS and SOS^{cat} that populate different nucleotide bound states. The abundances of various nucleotide bound states of binary and ternary complexes provides a glimpse into the affinity of nucleotides. For example, binary and ternary complexes of $KRAS^{G13D}$ are dominated by nucleotide-free states that may have bearing to the reported fast nucleotide exchange rates of the mutant protein (182). We also find an unexpected abundance of GDP immediately after mixing KRAS-GTP with SOS^{cat}, and addition of B-GTP to preformed ternary complex further validates the SOS^{cat} mediated stimulation of KRAS GTPase activity. However, no GDP was observed when a non-hydrolyzable analog is added to the complex. The presence of GDP was also observed for $KRAS^{G12C}$, which has reduced intrinsic GTPase activity compared to the wild-type protein (169). These results provide compelling evidence that SOS^{cat} has GAP-like characteristics. Nevertheless,

it is unknown if the hydrolysis reaction is carried out at the active or allosteric site(s) of SOS^{cat}. The observed ions corresponding to KRAS•$SOS^{W729E}$$(GDP)_1$ after immediate MS analysis of a KRAS-GTP and SOS^{W729E} mixtures suggests that the hydrolysis reaction likely occurs at the active site. Furthermore, SOS^{W729E} engineered to disrupt binding at the distal site shows a clear preference for binding KRAS-GDP at the active site, consistent with previous reports (153-155). However, our data also shows SOS^{W729E} does not completely abolish binding at the distal site as reported (153) thereby convoluting the interpretation of reported binding affinities (153-155). In addition, signal is detected corresponding to dimers of wild-type and oncogenic mutants of KRAS. At the concentration of KRAS (3 μM) used in the native MS studies, it is unlikely that the homodimers arise from non-specific association and provide direct evidence of KRAS dimerization, which has been implicated in RAS signaling (187).

The structure of $KRAS^{G13D}$•SOS^{cat}•$KRAS^{G13D}$-GppNp provides molecular details and clues to understanding the observed higher binding affinity of $KRAS^{G13D}$ for SOS^{cat}. First, $KRAS^{G13D}$ bound at the active site of SOS^{cat} is displaced compared to those in complex with HRAS and $KRAS^{G12C}$ (152, 160). Asp13 forms molecular interactions that reorients its sidechain away from the nucleotide binding pocket that is essentially primed for binding GTP to a greater extent than the wild-type protein. This observation draws a corollary to native MS results, where the majority of the ternary complex is not bound to GDP. Aside from structural differences observed at the active site, the overall structural similarity to the HRAS•SOS^{cat}•HRAS-GppNp complex indicate the molecular interactions would be similar for HRAS, KRAS, and $KRAS^{G13D}$. Therefore, a plausible explanation for the observed higher binding affinity of $KRAS^{G13D}$ is likely due to the altered dynamics of the mutant protein. In particular, Switch II of $KRAS^{G13D}$ is known to become less flexible, regardless of nucleotide bound state, and positively correlated with ß2- ß3 loop

motions (188). Importantly, switch II forms key interactions at the allosteric site of SOS^{cat} and the altered dynamics of switch II in $KRAS^{G13D}$ could result in an increase in the apparent binding affinity *i.e.* a larger fraction of $KRAS^{G13D}$ adopts a conformation(s) that can selectively engage SOS^{cat}. Moreover, the reduced dynamics of the switch II region of the $KRAS^{G13D}$-GDP can partly explain the ability of the GDP bound protein to bind at the allosteric site and form ternary complexes with SOS^{cat}.

As oncogenic mutants have impaired GTPase activity, it has been surmised that activation of oncogenic RAS is independent of SOS (189). For example, activation of $KRAS^{G13D}$ and $KRAS^{Q61H}$ has been suggested to be independent of SOS due to their fast nucleotide exchange rate and impaired-GTPase activity, respectively (155, 182). However, results from native MS reveal KRAS oncogenic mutants show an assortment of molecular assemblies ranging from weakly interacting $KRAS^{Q61H}$ to $KRAS^{G13D}$ that robustly engages SOS^{cat}. More specifically, $KRAS^{Q61H}$-GTP does not exert an allosteric effect implying that activation of this mutant is likely SOS-independent. In contRASt, $KRAS^{G13D}$-GTP unexpectedly forms predominantly a $KRAS^{G13D}$•SOS^{cat}•$KRAS^{G13D}$-GTP complex. $KRAS^{G13D}$-GDP also forms $KRAS^{G13D}$•SOS^{cat} •$KRAS^{G13D}$-$GDP(GDP)_{0\text{-}1}$ complexes suggesting the GDP bound form of this mutant may serve as an allosteric modulator of SOS^{cat}. Moreover, $KRAS^{G13D}$-GTP is a potent allosteric modulator of SOS^{cat} and can also enhance the SOS-mediated nucleotide exchange of wild-type KRAS. Considering cancer cells can be heterozygous for the $KRAS^{G13D}$ mutation, these findings are of particular importance as SOS activity can be allosterically modulated by $KRAS^{G13D}$, regardless of nucleotide bound state, that in turn would lead to robust SOS-mediated activation of KRAS. These findings provide additional evidence that oncogenic RAS bound at the allosteric site of SOS can cross-activate KRAS, which has been shown to be essential for tumorigenesis (190).

RAS activation is tightly regulated by SOS and disruption of this interaction is an attractive route for targeting RAS-driven cancers (159, 183). ARS-1620 (IC_{50}:120 nM) cannot disrupt assemblies of SOS^{cat} and $KRAS^{G12C}$-GTP suggesting $KRAS^{G12C}$-GDP within the ternary complex is shielded from reaction with ARS-1620. $KRAS^{G12C}$-GTP allosterically promotes the interaction of $KRAS^{G12C}$ at the active site, which diminishes the efficacy of the inhibitor to dissociate the complex. Kobe0065, designed to disrupt RAS binding at the allosteric site of SOS^{cat}, was ineffective for complexes formed with KRAS, $KRAS^{G12C}$ and $KRAS^{G13D}$. The recent discovery of KRAS•SOS disruptors have shown promising antiproliferative activity (160, 161). However, we show that while BAY-293 successfully disrupts KRAS and $KRAS^{G12C}$ complexes with SOS^{cat}, it fails to disrupt those formed with $KRAS^{G13D}$ at 119-fold the IC_{50} (IC_{50}=21 nM). Addition of BI-3406, 500-fold above the IC_{50} (IC_{50}=5nM), did not disrupt the ternary complex of $KRAS^{G13D}$-GTP and SOS^{cat}. Although BAY-293 and BI-3406 compounds can disrupt $KRAS^{G13D}$ binding to the active site of SOS^{cat} (**Fig 3.20E and 3.21D**), the presence of $KRAS^{G13D}$-GTP bound at the allosteric site of SOS^{cat} leads to enhanced stability of the ternary complex that is persistent to disruption with these small molecule disruptors. The antitumor activity of BAY-293 and BI-3406 is greatly enhanced in combination with specific $KRAS^{G12C}$ and MEK1 inhibitors (160, 161), and this strategy may mitigate cases where the efficacy of small molecule RAS•SOS disruptors is reduced when SOS is engaged with oncogenic RAS mutants, such as $KRAS^{G13D}$. Overall, the ability of $KRAS^{G13D}$ to exclusively form ternary complexes with SOS^{cat}, compete with KRAS binding SOS^{cat}, activate SOS^{cat} to facilitate loading of wild-type KRAS, and resistance to small molecule disruptors may explain the aggressive biology of tumors associated with this mutant (191). Moreover, the higher binding affinity of $KRAS^{G13D}$, and likely other RAS mutants, for SOS may lead to not only an increase in the recruitment of SOS to the plasma membrane but also

prolong dwell time allowing an increase in RAS activation by SOS (192). In closing, these results showcase the ability of native IM-MS to provide unprecedented insight into molecular assemblies, such as those formed between SOS^{cat} and KRAS, and open new avenues to develop more potent RAS-SOS inhibitors, especially for RAS mutants that robustly bind and activate SOS.

4. BIOCHEMICAL CHARACTERIZATION OF BRAF IN THE PRESENCE OF ATP COFACTOR AND COPPER

4.1. Introduction

The MAPK pathway has a critical role in multitude of cellular processes including cell proliferation, survival and differentiation. Dysregulation of the pathway is the leading cause of many cancers. Although RAS is the most common mutated protein in this pathway, the downstream alteration of other signaling pathway components such as RAF has been stablished more than 30 years ago (30, 193). In fact, RAF is the most frequent altered gene downstream of RAS in MAPK pathway and is observed in 7% of human tumors. The mammalian RAF kinase family (ARAF, BRAF and CRAF) share three conserved regions including CR1, CR2 and CR3. The N-terminus of RAF (CR1 and CR2) forms an intramolecular interaction with the kinase domain (CR3) and renders RAF as an inactive state in cytosol. The most recent cryo structure of BRAF shows that BRAF is in complex with MEK1 and 14-3-3 dimers, and interaction with14-3-3 dimers allows BRAF to adopt an inactive conformation (34). However, the role of 14-3-3 dimers on RAF regulation is not exactly known and has been the subject of controversy (34, 194, 195). It has been shown that 14-3-3 dimers are necessary for stabilization of both active and inactive conformation of RAF (196, 197). Interaction with active RAS relieves the autoinhibition of RAF and leads to the formation of RAF dimers. Active RAF then phosphorylates its downstream effector MEK1/2 and MEK1/2 subsequently activates ERK1/2.

The most common alterations observed in RAF genes belongs to BRAF with point mutations at valine 600. Point mutations at this residue constitute 90% of RAF alterations in cancer (30). More than 90% of $BRAF^{V600}$ mutations belong to substitution by glutamic acid,

$BRAF^{V600E}$(30). It has been shown that $BRAF^{V600E}$ is the central driving force behind the proliferation of melanoma. Although there are several FDA-approved inhibitors to prevent the catalytic activity of $BRAF^{V600E}$ mutant allele, resistance against these therapeutics have been developed by adapting to other escape mechanisms including upregulation of receptor tyrosine kinases and oncogenic RAS mutations in which lead to enhanced cell proliferation and tumor growth (198). This paradoxical behavior of RAF inhibitors is due to binding of small molecule to a single RAF monomer leading to allosteric activation of other RAF monomer which primes it for RAF dimerization and initiating the downstream signaling. The acquired resistance against different classes of BRAF inhibitors reflects a complex regulation of RAF kinases, and demands for deeper and more systematic study of relation between the activity of RAF kinases and its structure and interaction with other binding proteins. More specifically, it remains poorly understood how metal ions (Zn^{2+} and Cu^{2+}) and ATP binding influence the structure and function of BRAF that in turn regulates the cellular signaling? Brady et al discovered that decreasing the level of the copper by knocking down CTR1 (Cu transporter 1) or using copper chelators (*e.g.* TTM) decreases the $BRAF^{V600E}$-driven tumorigenesis and candidates TTM as a potential drug candidate to reduce melanoma growth (199). However, the molecular mechanism of how copper influx can increase the phosphorylation of ERK1/2 by MEK1/2 and the role of BRAF in this context are not known. Thus, we used native MS approaches to address key questions in the field of RAF regulation and more specifically to better understand how different metals and cofactors such as ATP regulate BRAF function and the MAPK signaling pathway.

We co-expressed BRAF with MEK1 in sf9 insect cells and subsequently characterized using high resolution UHMR equipped with a quadrupole mass analyzer. Our native MS results reveals that BRAF populates two different sub-complexes including BRAF bound to 14-3-3

dimers (BRAF-$(14\text{-}3\text{-}3)_2$) and BRAF bound to MEK1 and 14-3-3 dimers (BRAF-MEK1-$(14\text{-}3\text{-}3)_2$). We observed three different 14-3-3 dimers $(14\text{-}3\text{-}3)_2$ consisted of light and heavy subunits *i.e.* homodimers and heterodimer wherein the heterodimer is the dominant 14-3-3 dimer. The addition of ATP leads to the dimerization of BRAF in complex with 14-3-3 dimers. Copper also enhances the BRAF dimer formation and elevates gas-phase stability of BRAF-MEK1 complex . In addition, our study indicates that KRAS-GTP binds to both BRAF-$(14\text{-}3\text{-}3)_2$ and BRAF-MEK1-$(14\text{-}3\text{-}3)_2$ complexes, however, it does not induce dimerization of BRAF.

4.2. Methods

4.2.1. Protein expression and purification

The full-length BRAF and MEK1 were cloned into the baculovirus pACE acceptor and pIDC donor vectors, respectively. BRAF has an N-terminal His_6-tag and a C-terminal strep-tag with TEV protease cleavable at both sites. Both BRAF and MEK1 were infused using Cre-fusion reaction and integrated into MultiBac bacmid with Tn7 transposon (DH10EMBacY). After integration into MultiBac bacmid, baculoviral MEK1-BRAF DNA was lysed using Invitrogen kit (Thermo fisher scientific) and used to infect 30 ml of sf9 cells to generate viral stock. For production of BRAF heterologous complex, 200 ml cultures of Tni cells were infected with 20 ml of viral stock and cells were collected after 72 hours post infection. The BRAF-MEK1 complex was purified as previously described (34). In brief, the cell pellets of recombinant baculovirus BRAF-MEK1 complex were thawed on ice and resuspended in buffer A (150 mM NaCl, 50 mM Tris, 20 mM imidazole, 50 μM ATP, 2 mM $MgCl_2$, 1 mM DTT pH 7.4) supplemented with a complete protease inhibitor tablet (Roche). The cell suspension was lysed by a microfluidizer (Microfluidics M-110P) at 20000 psi and was clarified by centrifugation at 40000g for 20 minutes. All purification steps were performed at 4 °C. The clarified lysate was loaded onto a 5 mL HisTrap

HP column (GE Healthcare) pre-equilibrated in buffer A. The protein was eluted with buffer A containing 500 mM imidazole and pH adjusted to 8.0. The fractions containing protein were pooled and desalted using a HiPrep 26/10 desalting column (GE Healthcare) equilibrated in buffer A. The desalted protein was then digested with TEV protease at 4 °C and incubated overnight to remove the N- and C-terminal affinity tags. The proteins were passed over a 5 mL HisTrap HP column equilibrated with buffer A, and flow-through containing tag-less protein was collected. The flow-through was concentrated and subjected to size exclusion chromatography using a Highload 16/600 Superdex 75 pg column (GE Healthcare) equilibrated in buffer B (150 mM sodium chloride, 50 mM Tris, 1 mM DTT, 2 mM $MgCl_2$ and 50 μM ATP pH 7.4). Peak fractions containing protein were pooled, concentrated using a centrifugal concentrator (Millipore, 50K molecular weight cutoff (MWCO)), flash-frozen using liquid nitrogen, and stored at -80 °C.

4.2.2. Native mass spectrometry.

BRAF complexes were introduced into a Q Exactive UHMR hybrid quadrupole Orbitrap MS (Thermo Fisher Scientific, San Jose, CA). Samples were loaded into pulled borosilicate glass capillaries prepared in-house, and electrosprayed into the instrument with the voltage applied using a platinum wire inserted into the solution. Instrument parameters were tuned to minimize gas phase activation and to preserve non-covalent interactions between BRAF, MEK1 and 14-3-3 dimers.

4.3. Results and discussion

4.3.1. Characterization of BRAF complex

Figure 4.1 shows the mass spectrum of the full length BRAF co-expressed with MEK1 and analyzed by UHMR Orbitrap MS. The characterized complex by native MS reveals a high abundance of $(14\text{-}3\text{-}3)_2$ at low m/z region (Figure 4.1A). The mass isolation and subsequent

activation of the dominant 14-3-3 dimer results in peaks corresponding to light and heavy 14-3-3 monomers with masses of 27980 and 29680 Da, respectively.

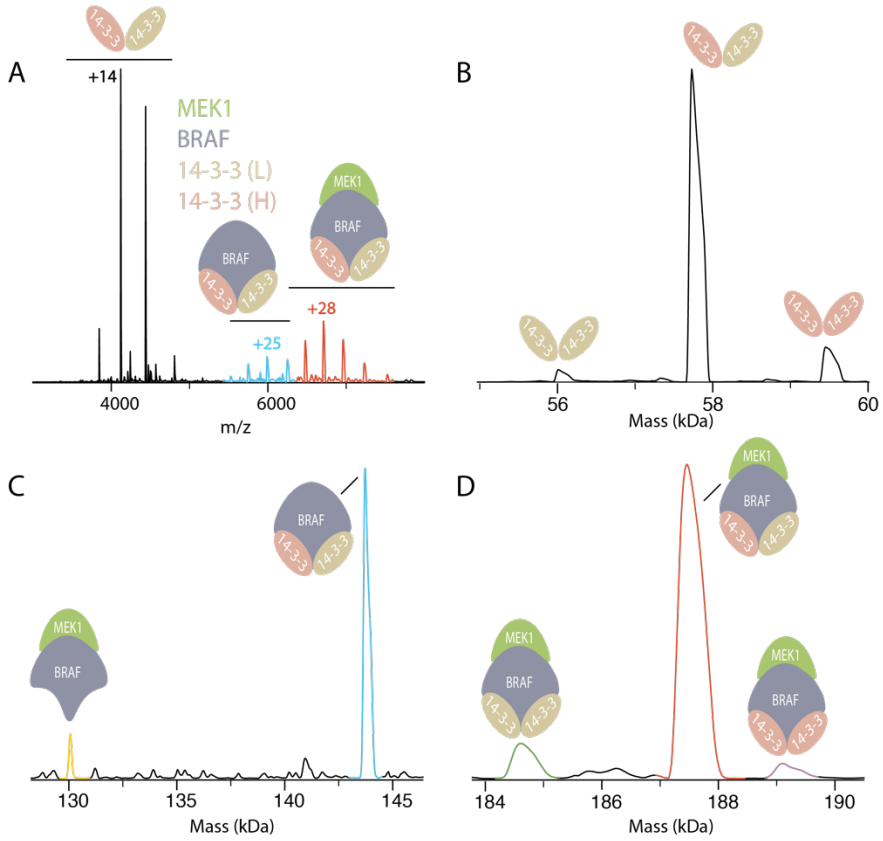

Figure 4.1. Characterization of full lenghth BRAF in complex with MEK1 and 14-3-3 dimer using high resolution mass spectrometry. (A) The native mass spectrum of full length BRAF co-expressed with MEK1 and endogenous 14-3-3 dimer. Cyan and red charge state distributions (CSDs) correspond to BRAF(14-3-3)$_2$ without and with MEK1 bound, repectively. Black CSD represents 14-3-3 heterodimer. Deconvoluted mass spectra of ions are shown in (B) black, (C) cyan and (D) red.

Three different 14-3-3 dimers shown in Figure 4.1B correspond to light homodimer (LL), heavy homodimer (HH) and heterodimer (LH). These results shows that the formation of the heterodimer is favored in cell due to their higher abundance shown in the deconvoluted mass spectrum (Figure 4.1B). At higher m/z region, BRAF bound to (14-3-3)$_2$ and MEK1-(14-3-3)$_2$ were detected shown in cyan and red, respectively. These BRAF complexes are composed of mainly the dominant 14-

3-3 heterodimer (Figure 4.1D, red peak). However, BRAF complexes with light and heavy homodimers are also formed (Figure 4.1D, green and purple peaks respectively). A closer inspection of the deconvoluted mass spectrum in Figure 4.1C reveals that BRAF also forms a complex with MEK1 in the absence of 14-3-3 dimers.

4.3.2. The effect of copper on BRAF activity

Given the role of copper in increasing the $BRAF^{V600E}$-driven tumorigenesis, we investigated the effect of copper on the interaction of the full-length BRAF with MEK1 and $(14\text{-}3\text{-}3)_2$ (199). The addition of 15 μM $Cu(OAC)_2$ induces the dimerization of full length BRAF bound to $(14\text{-}3\text{-}3)_2$ dimers resulting in $(BRAF)_2(14\text{-}3\text{-}3)_4$ complex (Figure 4.2A). The mass spectrum of BRAF dimer reveals that BRAF dimers are mainly consisted of high abundant 14-3-3 heterodimer (LH) (Figure 4.2B).

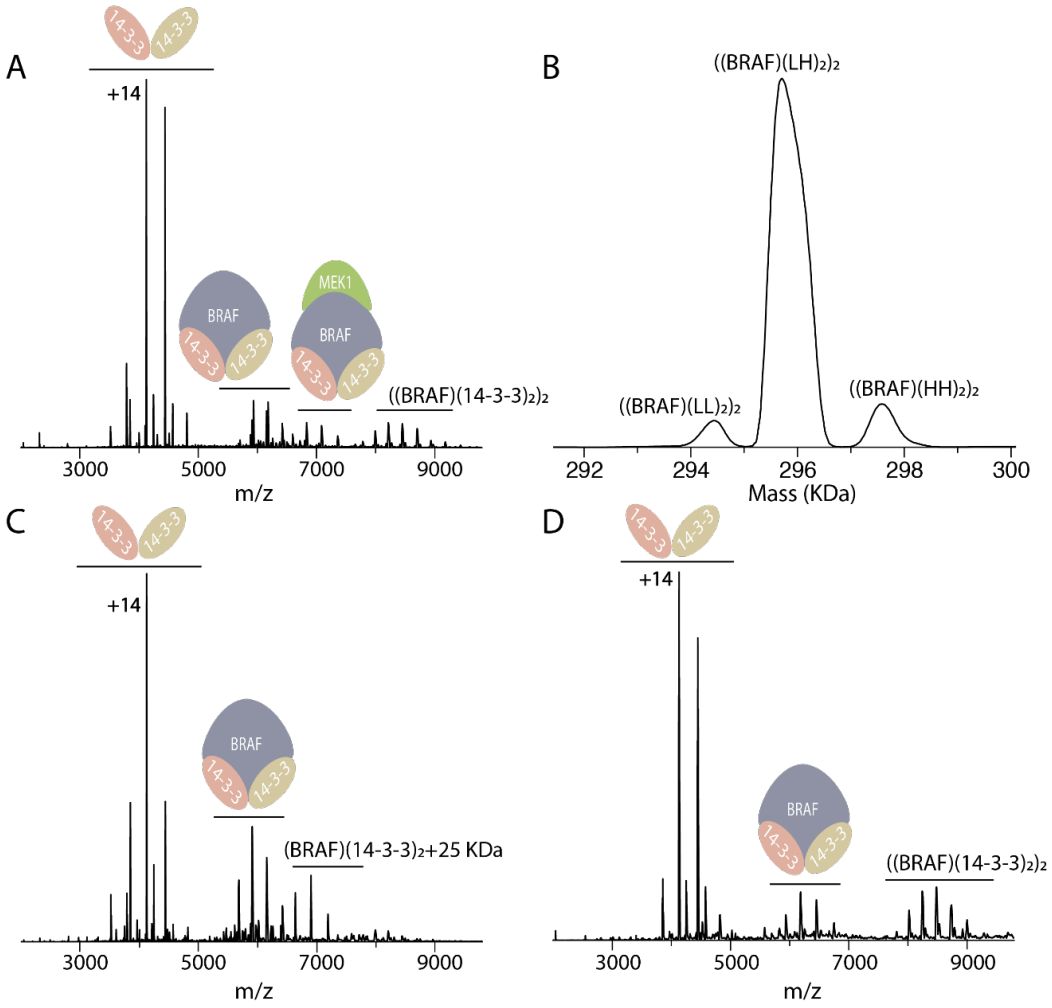

Figure 4.2. Copper induces the dimerization of BRAF in complex with 14-3-3 dimer. (A) 15 μM $Cu(OAC)_2$ was added to 5 μM of BRAF complex. (B) Deconvoluted MS of BRAF dimer shown in (A) reveals that BRAF forms dimer with both light and heavy 14-3-3 homodimer and heterodimer. The native MS of (C) BRAF expressed alone in sf9 cells and (D) in the presence of 15 μM $Cu(OAC)_2$.

Previous studies have shown that MEK1 binds directly to two copper ions with high affinity (10^{-18} M) (200). Copper promotes the interaction of MEK1 with ERK1/2 and stimulates MEK1-mediated phosphorylation of ERK1 in a dose dependent manner (200). Due to the extensive role of MEK1 on ERK phosphorylation and the high affinity of MEK1 for copper, we hypothesized that MEK1 upregulates BRAF activity by inducing the dimerization of BRAF. To test this

hypothesis, we also expressed BRAF in the absence of MEK1 in insect cell (Figure 4.2C). The addition of Copper to BRAF(14-3-3)$_2$ complex also stimulates BRAF dimerization in the absence of MEK1 by forming (BRAF)$_2$(14-3-3)$_4$ hetero-complex (Figure 4.2D). These results suggest that copper-induced dimerization of BRAF is independent of MEK1. However, no copper binding sites on full length BRAF has been identified, thus further experiments are warranted to identify potential copper binding sites of RAF. In addition, gas phase activation of BRAF-MEK1 in the presence of copper suggests that copper may enhance the interaction between BRAF and MEK1. In the absence of copper, activation of complex leads to ejection of (14-3-3)$_2$ dimers and MEK1 (Figure 4.3B) whereas in presence of copper no MEK1dissociate from the complex. (Figure 4.3 A)

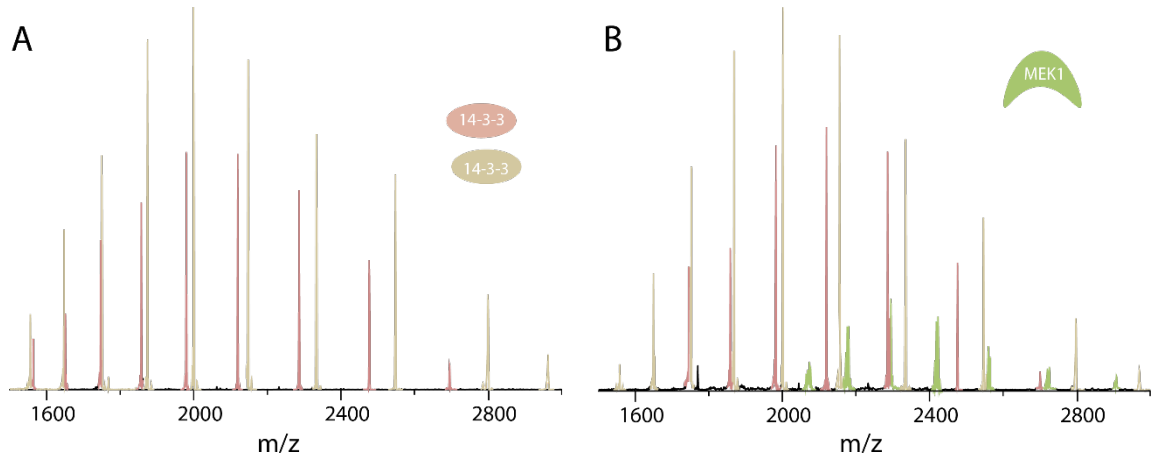

Figure 4.3. Copper may enhance the association of MEK1 with BRAF. The low m/z region mass spectra shown for 5 µM BRAF complex in the (A) presence and (B) absence of 15 µM copper acetate. Both mass spectra were collected under high collision energy (CE = 200 V).

4.3.3. The effect of ATP on dimerization of BRAF

It has been proposed that ATP imposes a negative regulatory mechanism on RAF and prevents the dimerization of RAF by promoting the BRAF autoinhibited conformation (10, 201). However, both ATP binding and RAF dimerization is needed to drive RAF into fully activated state; yet, the

occurrence of each of these phenomena seems to be mutually exclusive. In order to pinpoint how ATP affects the RAF dimerization, we investigated the stoichiometry of BRAF in complex with MEK1 and 14-3-3 dimer in the presence of ATP. The ATP addition leads to the dimerization of BRAF in a dose dependent manner (Figure 4.4). Although the measured mass of the BRAF dimer complex (~410 kDa) is close to the theoretical mass of the BRAF-MEK1-$(14\text{-}3\text{-}3)_2$ dimer (429 kDa), further experiments are necessary to confirm the exact stoichiometry of the complex.

The effect of ATP on BRAF activity remains to be controversial. The crystal structure of BRAF in complex with full length MEK1 and 14-3-3 dimer in the presence of ATP reveals that ATP stabilizes the inactive conformation of the kinase domain of BRAF (34). On the other hand, the presence of 14-3-3 dimers have been shown to overcome the negative regulatory of ATP (195) and to be essential for coupling RAF activity with downstream effectors (194). Our MS results reveal that BRAF in complex with MEK1 and $(14\text{-}3\text{-}3)_2$ dimerizes in the presence of ATP suggesting that BRAF complex does not favor the inactive conformation in the presence of ATP contradicting the previous studies. However, our results are in agreement with the role of 14-3-3 dimers that prevails the negative regulatory effect of ATP. Further experiments are needed to test the ability of isolated BRAF kinase domain to form dimer in the presence of ATP and clarify the effect of 14-3-3 dimer.

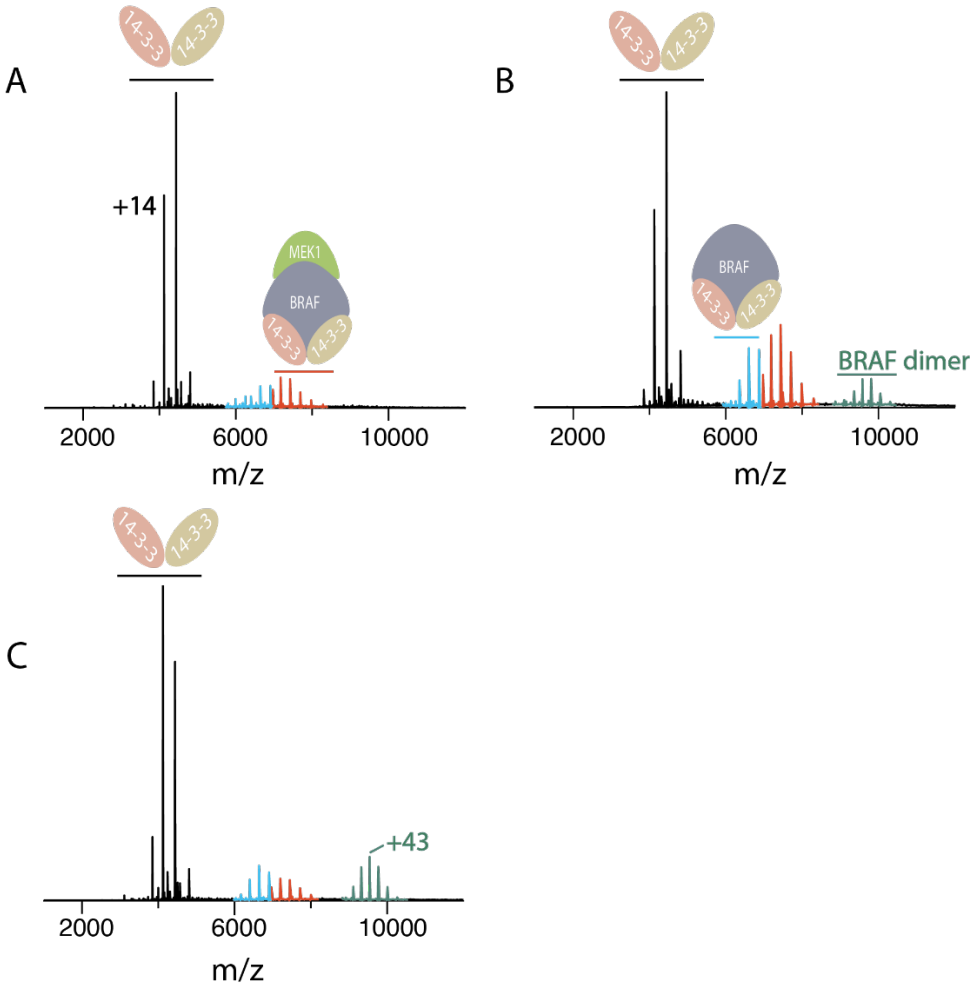

Figure 4.4. ATP increases BRAF dimerization in a dose dependent manner. The native mass spectra of (A) BRAF-MEK1-(14-3-3)$_2$ complex and in the presence of (B) 5µM and (C) 12.5 µM ATP. The green CSD represents dimer of BRAF complex.

4.3.4. KRAS4B interacts with full length BRAF complex

One of proposed mechanism of RAF activation involves binding of RAS to the RBD domain of RAF and is believed to drive the dimerization of RAF (3). It is speculated that this binding event allosterically exerts conformational changes to the RAF kinase domain and drives activation of RAF which is capable of dimer formation. However, little is known about how and to what extent RAS has an impact on RAF activation and dimerization. The majority of studies on RAF

interaction with RAS has been performed on truncated kinase domain of RAF suggesting that RAS increases dimerization of RAF kinase domain (10, 198). A recent study has utilized the full length BRAF in the absence of MEK1 and $(14\text{-}3\text{-}3)_2$ and measured BRAF activity against dead MEK1 in the presence of active HRAS (31). The activity of BRAF was not enhanced after quantification of MEK1 phosphorylation. Considering that BRAF exists in a complex with MEK1 and $(14\text{-}3\text{-}3)_2$ in the cytosol (34), we decided to investigate the interaction of RAF complex with active RAS using native MS. We show that the full length BRAF in complex with MEK1 and $(14\text{-}3\text{-}3)_2$ can bind to KRAS4B-GTP with HVR region truncated, although, no dimerization of BRAF is observed upon KRAS-GTP addition (Figure 4.5). These results indicate that BRAF activation is likely independent of RAS interaction as RAS can bind to RBD domain in both activated and inactivated states of RAF (34).

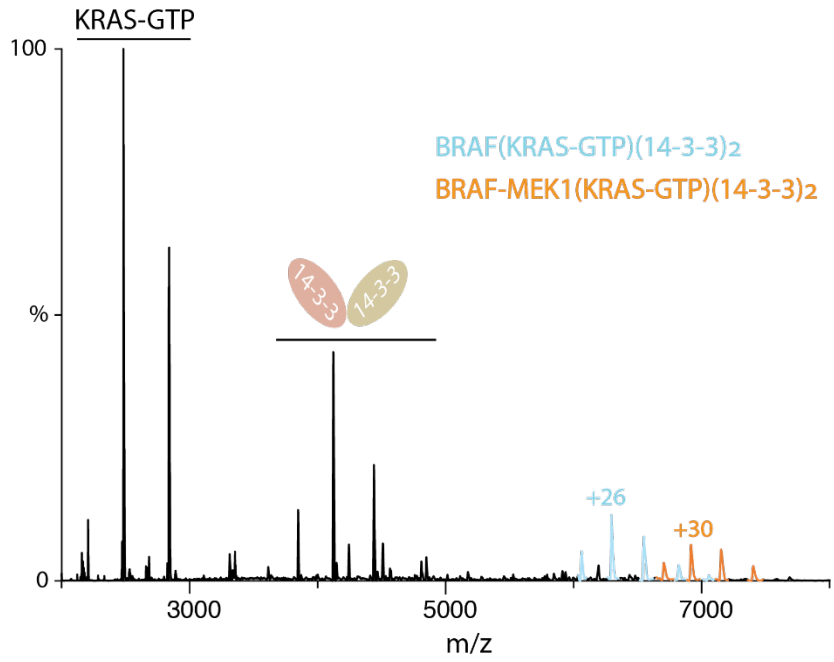

Figure 4.5. KRAS-GTP binds to BRAF-MEK1 -$(14\text{-}3\text{-}3)_2$ complex. Binding of active KRAS does not lead to BRAF dimerization.

In conclusion, the results obtained by native MS reveal that BRAF forms complex with MEK1, light and heavy $(14\text{-}3\text{-}3)_2$. Also, copper enhances the formation of BRAF homodimer and it appears to be independent of MEK1. Copper also prevents the MEK1 dissociation from BRAF complex suggesting that it most likely promotes the interaction of BRAF and MEK1. These results provide some plausible explanation why reducing the copper level leads to decreased tumorigenesis in cells carrying $BRAF^{V600E}$ allele. The dimerization of BRAF in the presence of ATP demonstrates that purified BRAF complex is in active conformation and is capable to undergo dimerization. Lastly, KRAS-GTP binding does not lead to the dimerization of BRAF and further proves the complex regulation of RAF kinases.

5. CONCLUSIONS AND FUTURE DIRECTIONS

In chapter 2, high-resolution native MS was used to determine the kinetics and thermodynamics of intrinsic GTP hydrolysis of KRAS and mutants. Native MS is a rapid and sensitive (minimal sample consumption) technique that revealed heterogeneity of the nucleotide bound to the "as isolated" proteins. For oncogenic mutants, the rates of hydrolysis of dGTP were faster than GTP hydrolysis. This result implies that the mutants bound to dGTP spend less time in the active state. Moreover, activation energetics reveals the barrier of the transition state is dominated by enthalpy and to a much lesser extent by entropy. The reduction in intrinsic hydrolysis for oncogenic mutants is due to an increased enthalpic barrier. The characterization of "as isolated" of other oncogenic mutants can be extended to HRAS and NRAS to determine the abundance of different nucleotide pool and any potential bound endogenous ligand similar to $KRAS^{G13D}$.

The second study was extended to study the assembly of SOS^{cat} with KRAS and its oncogenic mutants. IM spectrometry revealed the conformational dynamics of SOS^{cat} and KRAS conformational selection engaging the two first compact conformers of SOS^{cat}. With the capability of high resolution MS to discern the mass difference between GDP and GTP, it was shown that SOS^{cat} accelerates the intrinsic hydrolysis of KRAS presumably at the active site of SOS^{cat}, and the GAP-like activity of SOS^{cat} was discovered for the first time. Different assemblies between wild-type KRAS and mutants with SOS^{cat} were observed including binary and ternary complexes. Different KRAS mutants showed different modes of interaction with SOS^{cat}. While $KRAS^{Q61H}$ weakly engages with both active and allosteric sites of SOS^{cat}, the strong interaction of $KRAS^{G13D}$ with SOS^{cat} leads to the exclusive formation of the ternary complex. In addition, $KRAS^{G13D}$-GTP can outcompete KRAS wild-type at both active and allosteric sites of SOS^{cat} and allosterically

increases the SOS^{cat}-mediated nucleotide exchange rate of KRAS more than KRAS-GTP and $KRAS^{Q61H}$-GTP. The structural characterization of the ternary complex of $KRAS^{G13D}$-GTP and SOS^{cat} further provided insights into the unique behavior of $KRAS^{G13D}$ to form a predominant ternary complex at both active and allosteric site. However, the overall structural similarity of the complex with previously reported ternary complex of HRAS and SOS^{cat} suggests that high affinity of $KRAS^{G13D}$ at allosteric site may arise from different dynamics of $KRAS^{G13D}$ that populates a conformation that selectively bind to allosteric site of SOS^{cat}.

Disrupting the interaction between RAS and SOS has emerged as an attractive therapeutic strategy. The efficiency of strong small molecule RAS•SOS disruptors including BAY-293 and BI-3406 was tested to determine the stability of the ternary complex formed with active $KRAS^{G13D}$. These small molecules disrupted the binary complex of $KRAS^{G13D}$ and SOS^{cat} in the absence of active $KRAS^{G13D}$ at allosteric site. However, these inhibitors could not dissociate the robust ternary complex of SOS^{cat} and active $KRAS^{G13D}$. These results revealed the strong allosteric effect of $KRAS^{G13D}$ exerted on the ternary complex that prevents the disruption of the complex, in contrast to active KRAS and $KRAS^{G12C}$ where small molecules were able to dissociate their ternary complexes. Insights offered by RAS•SOS disruptors provides strategy to prevent SOS^{cat}-mediated activation of $KRAS^{G13D}$ by targeting $KRAS^{G13D}$ binding to allosteric site. Overall, the robust engagement of $KRAS^{G13D}$ with SOS^{cat}, cross-activation of wild-type KRAS and the ability to outcompete KRAS binding SOS^{cat} shows the unique behavior of $KRAS^{G13D}$ activated by SOS^{cat}. Taken together, native IM-MS provides direct evidence of conformational heterogeneity of SOS^{cat} and KRAS conformational selection, different assemblies of SOS^{cat} and KRAS, GAP-like activity of SOS^{cat} and different mode of interaction of $KRAS^{G13D}$ and $KRAS^{Q61H}$ being likely supersensitive and independent of SOS^{cat}, respectively. Given the importance of disruption of RAS

activation by SOS to curb the aberrant RAS signaling, it is imperative to understand how other oncogenic mutants of KRAS, HRAS and NRAS interact with SOS. To achieve this goal, similar studies will be conducted to generate a complete map of RAS interaction with catalytic domain of SOS to provide new avenues for improved therapeutic interventions.

The last study in chapter 4 is focused on characterization of BRAF, a downstream effector of RAS, and the effect of ATP cofactor and copper on BRAF activity. Our native MS results indicate that BRAF forms the complex with different populations of homodimer and heterodimer of $(14\text{-}3\text{-}3)_2$ with or without MEK1 bound to the complex. Copper stimulates the dimerization of BRAF while bound to $(14\text{-}3\text{-}3)_2$, and copper-induced dimerization of BRAF is MEK1-independent. We have also shown that full-length BRAF in complex with MEK1 and $(14\text{-}3\text{-}3)_2$ forms dimer in the presence of ATP indicating that purified BRAF complex does not adopt an inactive conformation. However, further experiments are warranted to confirm the exact stoichiometry of the ATP-induced BRAF complex including surface induced dissociation (SID) characterization. Lastly, the interaction of BRAF complex with KRAS-GTP does not lead to the dimerization of BRAF suggesting that binding of KRAS is not the sole driving factor to release autoinhibition state of BRAF. Further experiments are needed to examine the effect of HVR of RAS, responsible for PM association, on BRAF activation. In the light of the insights obtained by native MS, we will attempt to solve the structure of BRAF complex in the presence of copper and RAS-GTP to provide more structural insights on how copper and RAS binding regulate BRAF dimerization and activation, respectively.

REFERENCES

1. Harvey JJ (1964) An Unidentified Virus which causes the Rapid Production of Tumours in Mice. *Nature* 204(4963):1104-1105.
2. Chang EH, Gonda MA, Ellis RW, Scolnick EM, & Lowy DR (1982) Human genome contains four genes homologous to transforming genes of Harvey and Kirsten murine sarcoma viruses. *P Natl Acad Sci USA* 79(16):4848-4852.
3. Lu S*, et al.* (2016) Ras Conformational Ensembles, Allostery, and Signaling. *Chemical Reviews* 116(11):6607-6665.
4. Rojas JM, Oliva JL, & Santos E (2011) Mammalian Son of Sevenless Guanine Nucleotide Exchange Factors: Old Concepts and New Perspectives. *Genes & Cancer* 2(3):298-305.
5. Wittinghofer A, Scheffzek K, & Ahmadian MR (1997) The interaction of Ras with GTPase-activating proteins. *FEBS Letters* 410(1):63-67.
6. Downward J (2003) Targeting RAS signalling pathways in cancer therapy. *Nat Rev Cancer* 3(1):11-22.
7. Stephen AG, Esposito D, Bagni RK, & McCormick F (2014) Dragging ras back in the ring. *Cancer Cell* 25(3):272-281.
8. Moran MF, Polakis P, McCormick F, Pawson T, & Ellis C (1991) Protein-tyrosine kinases regulate the phosphorylation, protein interactions, subcellular distribution, and activity of p21ras GTPase-activating protein. *Molecular and cellular biology* 11(4):1804-1812.
9. Holderfield M, Deuker MM, McCormick F, & McMahon M (2014) Targeting RAF kinases for cancer therapy: BRAF-mutated melanoma and beyond. *Nature Reviews Cancer* 14(7):455-467.
10. Lavoie H*, et al.* (2013) Inhibitors that stabilize a closed RAF kinase domain conformation induce dimerization. *Nature Chemical Biology* 9(7):428-436.
11. Nussinov R, Jang H, & Tsai C-J (2014) The structural basis for cancer treatment decisions. *Oncotarget* 5(17):7285-7302.
12. Downward J (2008) Targeting RAS and PI3K in lung cancer. *Nature Medicine* 14(12):1315-1316.
13. Sadeghi N & Gerber DE (2012) Targeting the PI3K pathway for cancer therapy. *Future Med Chem* 4(9):1153-1169.
14. Malumbres M & Barbacid M (2003) RAS oncogenes: the first 30 years. *Nature Reviews Cancer* 3(6):459-465.
15. Castellano E & Santos E (2011) Functional Specificity of Ras Isoforms: So Similar but So Different. *Genes & Cancer* 2(3):216-231.
16. Quinlan MP & Settleman J (2009) Isoform-specific ras functions in development and cancer. *Future Oncology* 5(1):105-116.
17. Thompson H (2013) US National Cancer Institute's new Ras project targets an old foe. *Nature Medicine* 19(8):949-950.
18. Bollag G & Zhang C (2013) Pocket of opportunity. *Nature* 503(7477):475-476.

19. Adjei AA (2001) Blocking Oncogenic Ras Signaling for Cancer Therapy. *JNCI: Journal of the National Cancer Institute* 93(14):1062-1074.
20. Schubbert S, Shannon K, & Bollag G (2007) Hyperactive Ras in developmental disorders and cancer. *Nature Reviews Cancer* 7(4):295-308.
21. Smith MJ, Neel BG, & Ikura M (2013) NMR-based functional profiling of RASopathies and oncogenic RAS mutations. *Proceedings of the National Academy of Sciences* 110(12):4574-4579.
22. Pai EF*, et al.* (1990) Refined crystal structure of the triphosphate conformation of H-ras p21 at 1.35 A resolution: implications for the mechanism of GTP hydrolysis. *The EMBO journal* 9(8):2351-2359.
23. Milburn MV*, et al.* (1990) Molecular switch for signal transduction: structural differences between active and inactive forms of protooncogenic ras proteins. *Science* 247(4945):939.
24. Mosteller RD, Han J, & Broek D (1994) Identification of residues of the H-ras protein critical for functional interaction with guanine nucleotide exchange factors. *Molecular and Cellular Biology* 14(2):1104.
25. Cherfils J & Chardin P (1999) GEFs: structural basis for their activation of small GTP-binding proteins. *Trends in Biochemical Sciences* 24(8):306-311.
26. Gureasko J*, et al.* (2008) Membrane-dependent signal integration by the Ras activator Son of sevenless. *Nature Structural & Molecular Biology* 15(5):452-461.
27. Chardin P*, et al.* (1993) Human Sos1: a guanine nucleotide exchange factor for Ras that binds to GRB2. *Science* 260(5112):1338.
28. Boriack-Sjodin PA, Margarit SM, Bar-Sagi D, & Kuriyan J (1998) The structural basis of the activation of Ras by Sos. *Nature* 394(6691):337-343.
29. Margarit SM*, et al.* (2003) Structural Evidence for Feedback Activation by Ras·GTP of the Ras-Specific Nucleotide Exchange Factor SOS. *Cell* 112(5):685-695.
30. Yaeger R & Corcoran RB (2019) Targeting Alterations in the RAF–MEK Pathway. *Cancer Discovery* 9(3):329.
31. Cope N*, et al.* (2018) Mechanism of BRAF Activation through Biochemical Characterization of the Recombinant Full-Length Protein. *Chembiochem* 19(18):1988-1997.
32. Kolch W (2000) Meaningful relationships: the regulation of the Ras/Raf/MEK/ERK pathway by protein interactions. *The Biochemical journal* 351 Pt 2(Pt 2):289-305.
33. Roskoski R (2010) RAF protein-serine/threonine kinases: Structure and regulation. *Biochemical and Biophysical Research Communications* 399(3):313-317.
34. Park E*, et al.* (2019) Architecture of autoinhibited and active BRAF–MEK1–14-3-3 complexes. *Nature* 575(7783):545-550.
35. Loo JA (1997) Studying noncovalent protein complexes by electrospray ionization mass spectrometry. *Mass Spectrometry Reviews* 16(1):1-23.
36. Leney AC & Heck AJR (2017) Native Mass Spectrometry: What is in the Name? *Journal of The American Society for Mass Spectrometry* 28(1):5-13.
37. Annis DA, Nazef N, Chuang C-C, Scott MP, & Nash HM (2004) A General Technique To Rank Protein−Ligand Binding Affinities and Determine Allosteric versus Direct Binding Site Competition in Compound Mixtures. *Journal of the American Chemical Society* 126(47):15495-15503.

38. Berezovskaya Y*, et al.* (2011) Metal binding to a zinc-finger peptide: a comparison between solution and the gas phase. *Chemical Communications* 47(1):412-414.
39. Zhou M & Wysocki VH (2014) Surface Induced Dissociation: Dissecting Noncovalent Protein Complexes in the Gas phase. *Accounts of Chemical Research* 47(4):1010-1018.
40. Zhang S, Van Pelt CK, & Wilson DB (2003) Quantitative Determination of Noncovalent Binding Interactions Using Automated Nanoelectrospray Mass Spectrometry. *Analytical Chemistry* 75(13):3010-3018.
41. Cong X*, et al.* (2016) Determining Membrane Protein–Lipid Binding Thermodynamics Using Native Mass Spectrometry. *Journal of the American Chemical Society* 138(13):4346-4349.
42. Gülbakan B, Barylyuk K, & Zenobi R (2015) Determination of thermodynamic and kinetic properties of biomolecules by mass spectrometry. *Current Opinion in Biotechnology* 31:65-72.
43. Wilm M (2011) Principles of electrospray ionization. *Mol Cell Proteomics* 10(7):M111.009407-M009111.009407.
44. Alexandrov ML*, et al.* (2008) Extraction of ions from solutions under atmospheric pressure as a method for mass spectrometric analysis of bioorganic compounds. *Rapid Commun Mass Sp* 22(3):267-270.
45. Kebarle P & Tang L (1993) From ions in solution to ions in the gas phase - the mechanism of electrospray mass spectrometry. *Analytical Chemistry* 65(22):972A-986A.
46. Konermann L (2009) A simple model for the disintegration of highly charged solvent droplets during electrospray ionization. *Journal of the American Society for Mass Spectrometry* 20(3):496-506.
47. Thomson BA & Iribarne JV (1979) Field induced ion evaporation from liquid surfaces at atmospheric pressure. *Journal of Chemical Physics* 71:4451-4463.
48. Iribarne JV & Thomson BA (1976) On the evaporation of small ions from charged droplets. *Journal of Chemical Physics* 64:2287.
49. Clegg GA & Dole M (1971) Molecular beams of macroions. III. Zein and polyvinylpyrrolidone. *Biopolymers* 10(5):821-826.
50. Lomeli SH, Yin S, Ogorzalek Loo RR, & Loo JA (2009) Increasing charge while preserving noncovalent protein complexes for ESI-MS. *Journal of the American Society for Mass Spectrometry* 20(4):593-596.
51. Ahadi E & Konermann L (2012) Modeling the Behavior of Coarse-Grained Polymer Chains in Charged Water Droplets: Implications for the Mechanism of Electrospray Ionization. *The Journal of Physical Chemistry B* 116(1):104-112.
52. Benesch JLP & Robinson CV (2006) Mass spectrometry of macromolecular assemblies: preservation and dissociation. *Current Opinion in Structural Biology* 16(2):245-251.
53. Galhena AS, Dagan S, Jones CM, Beardsley RL, & Wysocki VH (2008) Surface-Induced Dissociation of Peptides and Protein Complexes in a Quadrupole/Time-of-Flight Mass Spectrometer. *Analytical Chemistry* 80(5):1425-1436.
54. Lermyte F, Williams JP, Brown JM, Martin EM, & Sobott F (2015) Extensive Charge Reduction and Dissociation of Intact Protein Complexes Following Electron Transfer on a Quadrupole-Ion Mobility-Time-of-Flight MS. *Journal of The American Society for Mass Spectrometry* 26(7):1068-1076.

55. Brodbelt JS (2014) Photodissociation mass spectrometry: new tools for characterization of biological molecules. *Chemical Society reviews* 43(8):2757-2783.
56. Zhou M*, et al.* (2008) Mass spectrometry reveals modularity and a complete subunit interaction map of the eukaryotic translation factor eIF3. *Proceedings of the National Academy of Sciences* 105(47):18139.
57. Johnson AR & Carlson EE (2015) Collision-Induced Dissociation Mass Spectrometry: A Powerful Tool for Natural Product Structure Elucidation. *Analytical Chemistry* 87(21):10668-10678.
58. Jennings KR (2000) The changing impact of the collision-induced decomposition of ions on mass spectrometry. *International Journal of Mass Spectrometry* 200(1):479-493.
59. Shukla AK & Futrell JH (2000) Tandem mass spectrometry: dissociation of ions by collisional activation. *Journal of Mass Spectrometry* 35(9):1069-1090.
60. Sleno L & Volmer DA (2004) Ion activation methods for tandem mass spectrometry. *Journal of Mass Spectrometry* 39(10):1091-1112.
61. Benesch JLP (2009) Collisional activation of protein complexes: Picking up the pieces. *Journal of the American Society for Mass Spectrometry* 20(3):341-348.
62. Quintyn RS, Yan J, & Wysocki VH (2015) Surface-Induced Dissociation of Homotetramers with D 2 Symmetry Yields their Assembly Pathways and Characterizes the Effect of Ligand Binding. *Chemistry & biology* 22(5):583-592.
63. McLean JA (2009) The mass-mobility correlation redux: The conformational landscape of anhydrous biomolecules. *Journal of the American Society for Mass Spectrometry* 20(10):1775-1781.
64. Lanucara F, Holman SW, Gray CJ, & Eyers CE (2014) The power of ion mobility-mass spectrometry for structural characterization and the study of conformational dynamics. *Nature Chemistry* 6:281.
65. Hill HH, Siems WF, & St. Louis RH (1990) Ion mobility spectrometry. *Analytical Chemistry* 62(23):1201A-1209A.
66. Giles K*, et al.* (2004) Applications of a travelling wave-based radio-frequency-only stacked ring ion guide. *Rapid Commun Mass Sp* 18(20):2401-2414.
67. Purves RW & Guevremont R (1999) Electrospray Ionization High-Field Asymmetric Waveform Ion Mobility Spectrometry−Mass Spectrometry. *Analytical Chemistry* 71(13):2346-2357.
68. Mason EA & Schamp HW (1958) Mobility of gaseous lons in weak electric fields. *Annals of Physics* 4(3):233-270.
69. Scarff CA, Thalassinos K, Hilton GR, & Scrivens JH (2008) Travelling wave ion mobility mass spectrometry studies of protein structure: biological significance and comparison with X-ray crystallography and nuclear magnetic resonance spectroscopy measurements. *Rapid Commun Mass Sp* 22(20):3297-3304.
70. Hyung S-J, Robinson CV, & Ruotolo BT (2009) Gas-Phase Unfolding and Disassembly Reveals Stability Differences in Ligand-Bound Multiprotein Complexes. *Chemistry & Biology* 16(4):382-390.
71. Hopper JTS & Oldham NJ (2009) Collision induced unfolding of protein ions in the gas phase studied by ion mobility-mass spectrometry: The effect of ligand binding on conformational stability. *Journal of the American Society for Mass Spectrometry* 20(10):1851-1858.

72. Smith DP, Radford SE, & Ashcroft AE (2010) Elongated oligomers in β₂-microglobulin amyloid assembly revealed by ion mobility spectrometry-mass spectrometry. *Proceedings of the National Academy of Sciences* 107(15):6794.
73. Beveridge R, Chappuis Q, Macphee C, & Barran P (2013) Mass spectrometry methods for intrinsically disordered proteins. *Analyst* 138(1):32-42.
74. Jenner M*, et al.* (2011) Detection of a Protein Conformational Equilibrium by Electrospray Ionisation-Ion Mobility-Mass Spectrometry. *Angewandte Chemie International Edition* 50(36):8291-8294.
75. Bereszczak JZ*, et al.* (2012) Structure, stability and dynamics of norovirus P domain derived protein complexes studied by native mass spectrometry. *Journal of Structural Biology* 177(2):273-282.
76. Uetrecht C*, et al.* (2008) Stability and Shape of Hepatitis B Virus Capsids In Vacuo. *Angewandte Chemie International Edition* 47(33):6247-6251.
77. Labastie P & Doy M (1989) A high mass range quadrupole spectrometer for cluster studies. *International Journal of Mass Spectrometry and Ion Processes* 91(2):105-112.
78. Benesch JLP, Ruotolo BT, Simmons DA, & Robinson CV (2007) Protein Complexes in the Gas Phase: Technology for Structural Genomics and Proteomics. *Chemical Reviews* 107(8):3544-3567.
79. Mehmood S, Allison TM, & Robinson CV (2015) Mass Spectrometry of Protein Complexes: From Origins to Applications. *Annual Review of Physical Chemistry* 66(1):453-474.
80. Makarov A (2000) Electrostatic Axially Harmonic Orbital Trapping: A High-Performance Technique of Mass Analysis. *Analytical Chemistry* 72(6):1156-1162.
81. Zubarev RA & Makarov A (2013) Orbitrap Mass Spectrometry. *Analytical Chemistry* 85(11):5288-5296.
82. Wiesmuller L & Wittinghofer F (1994) Signal-Transduction Pathways Involving Ras. *Cell Signal* 6(3):247-267.
83. Pylayeva-Gupta Y, Grabocka E, & Bar-Sagi D (2011) RAS oncogenes: weaving a tumorigenic web. *Nature Reviews Cancer* 11:761-774.
84. Drosten M*, et al.* (2010) Genetic analysis of Ras signalling pathways in cell proliferation, migration and survival. *EMBO J* 29(6):1091-1104.
85. Colicelli J (2004) Human RAS superfamily proteins and related GTPases. *Sci STKE* 2004(250):RE13.
86. Goitre L, Trapani E, Trabalzini L, & Retta SF (2014) The Ras superfamily of small GTPases: the unlocked secrets. *Methods Mol Biol* 1120:1-18.
87. Bourne HR, Sanders DA, & McCormick F (1991) The GTPase superfamily: conserved structure and molecular mechanism. *Nature* 349(6305):117-127.
88. Downward J (1990) The ras superfamily of small GTP-binding proteins. *Trends in Biochemical Sciences* 15(12):469-472.
89. Vetter IR & Wittinghofer A (2001) The Guanine Nucleotide-Binding Switch in Three Dimensions. *Science* 294(5545):1299-1304.
90. Wennerberg K, Rossman KL, & Der CJ (2005) The Ras superfamily at a glance. *Journal of Cell Science* 118(5):843-846.

91. Vetter IR & Wittinghofer A (2001) The guanine nucleotide-binding switch in three dimensions. *Science* 294(5545):1299-1304.
92. Cox AD, Fesik SW, Kimmelman AC, Luo J, & Der CJ (2014) Drugging the undruggable RAS: Mission possible? *Nat Rev Drug Discov* 13(11):828-851.
93. Cherfils J & Zeghouf M (2013) Regulation of Small GTPases by GEFs, GAPs, and GDIs. *Physiological Reviews* 93(1):269-309.
94. Cox AD & Der CJ (2010) Ras history: The saga continues. *Small GTPases* 1(1):2-27.
95. Malumbres M & Barbacid M (2003) RAS oncogenes: the first 30 years. *Nat Rev Cancer* 3(6):459-465.
96. Prior IA, Lewis PD, & Mattos C (2012) A comprehensive survey of Ras mutations in cancer. *Cancer Res* 72(10):2457-2467.
97. Forbes SA*, et al.* (2011) COSMIC: mining complete cancer genomes in the Catalogue of Somatic Mutations in Cancer. *Nucleic acids research* 39(Database issue):D945-D950.
98. Miller MS & Miller LD (2011) RAS Mutations and Oncogenesis: Not all RAS Mutations are Created Equally. *Front Genet* 2:1-19.
99. Schubbert S, Shannon K, & Bollag G (2007) Hyperactive Ras in developmental disorders and cancer. *Nature Reviews Cancer* 7:295-308.
100. Vigil D, Cherfils J, Rossman KL, & Der CJ (2010) Ras superfamily GEFs and GAPs: validated and tractable targets for cancer therapy? *Nature Reviews Cancer* 10:842-857.
101. Fernandez-Medarde A & Santos E (2011) Ras in cancer and developmental diseases. *Genes Cancer* 2(3):344-358.
102. Karnoub AE & Weinberg RA (2008) Ras oncogenes: split personalities. *Nature Reviews Molecular Cell Biology* 9:517-531.
103. Morelli MP & Kopetz S (2012) Hurdles and Complexities of Codon 13 KRAS Mutations. *Journal of Clinical Oncology* 30(29):3565-3567.
104. Guerrero S*, et al.* (2000) K-ras codon 12 mutation induces higher level of resistance to apoptosis and predisposition to anchorage-independent growth than codon 13 mutation or proto-oncogene overexpression. *Cancer Research* 60(23):6750-6756.
105. Kraus MC, Seelig MH, Linnemann U, & Berger MR (2006) The balanced induction of K-ras codon 12 and 13 mutations in mucosa differs from their ratio in neoplastic tissues. *International Journal of Oncology* 29(4):957-964.
106. Neal SE, Eccleston JF, Hall A, & Webb MR (1988) Kinetic analysis of the hydrolysis of GTP by p21N-ras. The basal GTPase mechanism. *Journal of Biological Chemistry* 263(36):19718-19722.
107. Self AJ & Hall A (1995) [8] Measurement of intrinsic nucleotide exchange and GTP hydrolysis rates. *Methods in Enzymology*, (Academic Press), Vol 256, pp 67-76.
108. Webb MR & Hunter JL (1992) Interaction of GTPase-activating protein with p21ras, measured using a continuous assay for inorganic phosphate release. *The Biochemical journal* 287 (Pt 2)(Pt 2):555-559.
109. Gideon P*, et al.* (1992) Mutational and kinetic analyses of the GTPase-activating protein (GAP)-p21 interaction: the C-terminal domain of GAP is not sufficient for full activity. *Molecular and Cellular Biology* 12(5):2050-2056.
110. Kötting C & Gerwert K (2004) Time-resolved FTIR studies provide activation free energy, activation enthalpy and activation entropy for GTPase reactions. *Chemical Physics* 307(2):227-232.

111. Heck AJR & van den Heuvel RHH (2004) Investigation of intact protein complexes by mass spectrometry. *Mass Spectrometry Reviews* 23(5):368-389.
112. Hilton Gillian R & Benesch Justin LP (2012) Two decades of studying non-covalent biomolecular assemblies by means of electrospray ionization mass spectrometry. *Journal of The Royal Society Interface* 9(70):801-816.
113. Pacholarz KJ, Garlish RA, Taylor RJ, & Barran PE (2012) Mass spectrometry based tools to investigate protein-ligand interactions for drug discovery. *Chemical Society Reviews* 41(11):4335-4355.
114. Hilton GR & Benesch JL (2012) Two decades of studying non-covalent biomolecular assemblies by means of electrospray ionization mass spectrometry. *J R Soc Interface* 9(70):801-816.
115. Ruotolo BT*, et al.* (2005) Evidence for macromolecular protein rings in the absence of bulk water. *Science* 310(5754):1658-1661.
116. Ruotolo BT, Tate CC, & Russell DH (2004) Ion mobility-mass spectrometry applied to cyclic peptide analysis: conformational preferences of gramicidin S and linear analogs in the gas phase. *J Am Soc Mass Spectrom* 15(6):870-878.
117. Daneshfar R, Kitova EN, & Klassen JS (2004) Determination of protein-ligand association thermochemistry using variable-temperature nanoelectrospray mass spectrometry. *J Am Chem Soc* 126(15):4786-4787.
118. Rose RJ, Damoc E, Denisov E, Makarov A, & Heck AJR (2012) High-sensitivity Orbitrap mass analysis of intact macromolecular assemblies. *Nature Methods* 9:1084-1086.
119. Patrick JW*, et al.* (2018) Allostery revealed within lipid binding events to membrane proteins. *Proceedings of the National Academy of Sciences* 115(12):2976-2981.
120. Shirzadeh M, Boone CD, Laganowsky A, & Russell DH (2019) Topological Analysis of Transthyretin Disassembly Mechanism: Surface-Induced Dissociation Reveals Hidden Reaction Pathways. *Analytical Chemistry* 91(3):2345-2351.
121. Maple HJ*, et al.* (2014) Application of the Exactive Plus EMR for automated protein-ligand screening by non-covalent mass spectrometry. *Rapid Commun Mass Sp* 28(13):1561-1568.
122. Poltash ML*, et al.* (2019) New insights into the metal-induced oxidative degradation pathways of transthyretin. *Chemical Communications* 90(28):10472-10478.
123. Lanucara F, Holman SW, Gray CJ, & Eyers CE (2014) The power of ion mobility-mass spectrometry for structural characterization and the study of conformational dynamics. *Nature Chemistry* 6:281-294.
124. Laganowsky A, Reading E, Hopper JT, & Robinson CV (2013) Mass spectrometry of intact membrane protein complexes. *Nat Protoc* 8(4):639-651.
125. Marty MT*, et al.* (2015) Bayesian deconvolution of mass and ion mobility spectra: from binary interactions to polydisperse ensembles. *Anal Chem* 87(8):4370-4376.
126. May JC*, et al.* (2014) Conformational Ordering of Biomolecules in the Gas Phase: Nitrogen Collision Cross Sections Measured on a Prototype High Resolution Drift Tube Ion Mobility-Mass Spectrometer. *Analytical Chemistry* 86(4):2107-2116.
127. Stow SM*, et al.* (2017) An Interlaboratory Evaluation of Drift Tube Ion Mobility–Mass Spectrometry Collision Cross Section Measurements. *Analytical Chemistry* 89(17):9048-9055.

128. Lanzetta PA, Alvarez LJ, Reinach PS, & Candia OA (1979) An improved assay for nanomole amounts of inorganic phosphate. *Analytical Biochemistry* 100(1):95-97.
129. Quan A & Robinson PJ (2005) Rapid Purification of Native Dynamin I and Colorimetric GTPase Assay. *Methods in Enzymology*, (Academic Press), Vol 404, pp 556-569.
130. Eyring H (1935) The Activated Complex in Chemical Reactions. *The Journal of Chemical Physics* 3(2):107-115.
131. Johnson KA, Simpson ZB, & Blom T (2009) Global kinetic explorer: a new computer program for dynamic simulation and fitting of kinetic data. *Anal Biochem* 387(1):20-29.
132. Johnson KA, Simpson ZB, & Blom T (2009) FitSpace explorer: an algorithm to evaluate multidimensional parameter space in fitting kinetic data. *Anal Biochem* 387(1):30-41.
133. Novelli ET, First JT, & Webb LJ (2018) Quantitative Measurement of Intrinsic GTP Hydrolysis for Carcinogenic Glutamine 61 Mutants in H-Ras. *Biochemistry* 57(44):6356-6366.
134. Guymer D, Maillard J, Agacan MF, Brearley CA, & Sargent F (2010) Intrinsic GTPase activity of a bacterial twin-arginine translocation proofreading chaperone induced by domain swapping. *The FEBS Journal* 277(2):511-525.
135. Buckstein MH, He J, & Rubin H (2008) Characterization of Nucleotide Pools as a Function of Physiological State in Escherichia coli. *Journal of Bacteriology* 190(2):718-726.
136. Liao J*, et al.* (2008) Two conformational states of Ras GTPase exhibit differential GTP-binding kinetics. *Biochemical and Biophysical Research Communications* 369(2):327-332.
137. Shima F*, et al.* (2010) Structural Basis for Conformational Dynamics of GTP-bound Ras Protein. *J Biol Chem* 285(29):22696-22705.
138. Araki M*, et al.* (2011) Solution Structure of the State 1 Conformer of GTP-bound H-Ras Protein and Distinct Dynamic Properties between the State 1 and State 2 Conformers. *J Biol Chem* 286(45):39644-39653.
139. Lu S, Jang H, Nussinov R, & Zhang J (2016) The Structural Basis of Oncogenic Mutations G12, G13 and Q61 in Small GTPase K-Ras4B. *Scientific Reports* 6:21949:1-15.
140. Buhrman G, Wink G, & Mattos C (2007) Transformation Efficiency of RasQ61 Mutants Linked to Structural Features of the Switch Regions in the Presence of Raf. *Structure* 15(12):1618-1629.
141. Poltash ML*, et al.* (2018) Fourier Transform-Ion Mobility-Orbitrap Mass Spectrometer: A Next-Generation Instrument for Native Mass Spectrometry. *Anal Chem* 90(17):10472-10478.
142. Glaskin RS, Valentine SJ, & Clemmer DE (2010) A Scanning Frequency Mode for Ion Cyclotron Mobility Spectrometry. *Analytical Chemistry* 82(19):8266-8271.
143. MISTOU M-Y, COOL RH, & PARMEGGIANI A (1992) Effects of ions on the intrinsic activities of c-H-ras protein p21. *European Journal of Biochemistry* 204(1):179-185.
144. Wey M, Lee J, Jeong SS, Kim J, & Heo J (2013) Kinetic Mechanisms of Mutation-Dependent Harvey Ras Activation and Their Relevance for the Development of Costello Syndrome. *Biochemistry* 52(47):8465-8479.
145. Pavlova NN & Thompson CB (2016) The Emerging Hallmarks of Cancer Metabolism. *Cell metabolism* 23(1):27-47.

146. Buj R & Aird KM (2018) Deoxyribonucleotide Triphosphate Metabolism in Cancer and Metabolic Disease. *Frontiers in Endocrinology* 9(177):1-10.
147. Åqvist J & Kamerlin SCL (2016) Conserved Motifs in Different Classes of GTPases Dictate their Specific Modes of Catalysis. *ACS Catalysis* 6(3):1737-1743.
148. Villà J*, et al.* (2000) How important are entropic contributions to enzyme catalysis? *Proceedings of the National Academy of Sciences* 97(22):11899-11904.
149. Warshel A (1998) Electrostatic Origin of the Catalytic Power of Enzymes and the Role of Preorganized Active Sites. *J Biol Chem* 273(42):27035-27038.
150. Cannon WR & Benkovic SJ (1998) Solvation, Reorganization Energy, and Biological Catalysis. *J Biol Chem* 273(41):26257-26260.
151. Vigil D, Cherfils J, Rossman KL, & Der CJ (2010) Ras superfamily GEFs and GAPs: validated and tractable targets for cancer therapy? *Nature Reviews Cancer* 10(12):842-857.
152. Margarit SM*, et al.* (2003) Structural evidence for feedback activation by Ras.GTP of the Ras-specific nucleotide exchange factor SOS. *Cell* 112(5):685-695.
153. Sondermann H*, et al.* (2004) Structural Analysis of Autoinhibition in the Ras Activator Son of Sevenless. *Cell* 119(3):393-405.
154. Vo U*, et al.* (2016) Monitoring Ras Interactions with the Nucleotide Exchange Factor Son of Sevenless (Sos) Using Site-specific NMR Reporter Signals and Intrinsic Fluorescence. *J Biol Chem* 291(4):1703-1718.
155. Smith MJ, Neel BG, & Ikura M (2013) NMR-based functional profiling of RASopathies and oncogenic RAS mutations. *Proceedings of the National Academy of Sciences* 110(12):4574.
156. Freedman TS*, et al.* (2009) Differences in Flexibility Underlie Functional Differences in the Ras Activators Son of Sevenless and Ras Guanine Nucleotide Releasing Factor 1. *Structure* 17(1):41-53.
157. Iversen L*, et al.* (2014) Molecular kinetics. Ras activation by SOS: allosteric regulation by altered fluctuation dynamics. *Science* 345(6192):50-54.
158. Ostrem JM & Shokat KM (2016) Direct small-molecule inhibitors of KRAS: from structural insights to mechanism-based design. *Nat Rev Drug Discov* 15(11):771-785.
159. Lu S, Jang H, Zhang J, & Nussinov R (2016) Inhibitors of Ras–SOS Interactions. *ChemMedChem* 11(8):814-821.
160. Hillig RC*, et al.* (2019) Discovery of potent SOS1 inhibitors that block RAS activation via disruption of the RAS-SOS1 interaction. *Proc Natl Acad Sci U S A* 116(7):2551-2560.
161. Hofmann MH*, et al.* (2021) BI-3406, a Potent and Selective SOS1–KRAS Interaction Inhibitor, Is Effective in KRAS-Driven Cancers through Combined MEK Inhibition. *Cancer Discovery* 11(1):142.
162. Allison TM & Bechara C (2019) Structural mass spectrometry comes of age: new insight into protein structure, function and interactions. *Biochemical Society Transactions* 47(1):317-327.
163. Gault J*, et al.* (2016) High-resolution mass spectrometry of small molecules bound to membrane proteins. *Nat Methods* 13(4):333-336.
164. Cong X*, et al.* (2016) Determining Membrane Protein-Lipid Binding Thermodynamics Using Native Mass Spectrometry. *J Am Chem Soc* 138(13):4346-4349.

165. Benesch JL, Sobott F, & Robinson CV (2003) Thermal dissociation of multimeric protein complexes by using nanoelectrospray mass spectrometry. *Anal Chem* 75(10):2208-2214.
166. El-Baba TJ*, et al.* (2017) Melting Proteins: Evidence for Multiple Stable Structures upon Thermal Denaturation of Native Ubiquitin from Ion Mobility Spectrometry-Mass Spectrometry Measurements. *J Am Chem Soc* 139(18):6306-6309.
167. Raab SA*, et al.* (2020) Evidence for Many Unique Solution Structures for Chymotrypsin Inhibitor 2: A Thermodynamic Perspective Derived from vT-ESI-IMS-MS Measurements. *J Am Chem Soc* 142(41):17372-17383.
168. Cong X, Liu Y, Liu W, Liang X, & Laganowsky A (2017) Allosteric modulation of protein-protein interactions by individual lipid binding events. *Nat Commun* 8(1):2203.
169. Moghadamchargari Z*, et al.* (2019) Intrinsic GTPase Activity of K-RAS Monitored by Native Mass Spectrometry. *Biochemistry* 58(31):3396-3405.
170. McCabe JW*, et al.* (2020) THE IMS PARADOX: A PERSPECTIVE ON STRUCTURAL ION MOBILITY-MASS SPECTROMETRY. *Mass Spectrometry Reviews* n/a(n/a).
171. Mason EA & McDaniel EW (1988) Transport properties of ions in gases. *NASA STI/Recon Technical Report A* 89:15174.
172. Zhou M, Huang C, & Wysocki VH (2012) Surface-Induced Dissociation of Ion Mobility-Separated Noncovalent Complexes in a Quadrupole/Time-of-Flight Mass Spectrometer. *Analytical Chemistry* 84(14):6016-6023.
173. Zheng S, Palovcak E, Armache J-P, Cheng Y, & Agard D (2016) Anisotropic Correction of Beam-induced Motion for Improved Single-particle Electron Cryo-microscopy. *bioRxiv*:061960-061960.
174. Mindell JA & Grigorieff N (2003) Accurate determination of local defocus and specimen tilt in electron microscopy. *Journal of Structural Biology* 142(3):334-347.
175. Scheres SHW (2012) RELION: Implementation of a Bayesian approach to cryo-EM structure determination. *Journal of Structural Biology* 180(3):519-530.
176. Pettersen EF*, et al.* (2004) UCSF Chimera - A visualization system for exploratory research and analysis. *Journal of Computational Chemistry* 25(13):1605-1612.
177. Emsley P & Cowtan K (2004) Coot: Model-building tools for molecular graphics. *Acta Crystallographica Section D: Biological Crystallography* 60(12 I):2126-2132.
178. Adams PD*, et al.* (2010) PHENIX: a comprehensive Python-based system for macromolecular structure solution. *Acta crystallographica. Section D, Biological crystallography* 66(Pt 2):213-221.
179. Johnson CW*, et al.* (2019) Isoform-Specific Destabilization of the Active Site Reveals a Molecular Mechanism of Intrinsic Activation of KRas G13D. *Cell Reports* 28(6):1538-1550.e1537.
180. Lu S, Jang H, Nussinov R, & Zhang J (2016) The Structural Basis of Oncogenic Mutations G12, G13 and Q61 in Small GTPase K-Ras4B. *Scientific Reports* 6:21949.
181. Hall BE, Yang SS, Boriack-Sjodin PA, Kuriyan J, & Bar-Sagi D (2001) Structure-based mutagenesis reveals distinct functions for Ras switch 1 and switch 2 in Sos-catalyzed guanine nucleotide exchange. *J Biol Chem* 276(29):27629-27637.
182. Hunter JC*, et al.* (2015) Biochemical and Structural Analysis of Common Cancer-Associated KRAS Mutations. *Molecular Cancer Research* 13(9):1325.

183. Patgiri A, Yadav KK, Arora PS, & Bar-Sagi D (2011) An orthosteric inhibitor of the Ras-Sos interaction. *Nature Chemical Biology* 7(9):585-587.
184. Janes MR*, et al.* (2018) Targeting KRAS Mutant Cancers with a Covalent G12C-Specific Inhibitor. *Cell* 172(3):578-589.e517.
185. Shima F*, et al.* (2013) In silico discovery of small-molecule Ras inhibitors that display antitumor activity by blocking the Ras–effector interaction. *Proceedings of the National Academy of Sciences* 110(20):8182.
186. Smock RG & Gierasch LM (2009) Sending Signals Dynamically. *Science* 324(5924):198.
187. Rhett JM, Khan I, & O'Bryan JP (2020) Biology, pathology, and therapeutic targeting of RAS. *Adv Cancer Res* 148:69-146.
188. Vatansever S, Erman B, & Gümüş ZH (2020) Comparative effects of oncogenic mutations G12C, G12V, G13D, and Q61H on local conformations and dynamics of K-Ras. *Computational and Structural Biotechnology Journal* 18:1000-1011.
189. Li S, Balmain A, & Counter CM (2018) A model for RAS mutation patterns in cancers: finding the sweet spot. *Nature Reviews Cancer* 18(12):767-777.
190. Jeng H-H, Taylor LJ, & Bar-Sagi D (2012) Sos-mediated cross-activation of wild-type Ras by oncogenic Ras is essential for tumorigenesis. *Nature Communications* 3(1):1168.
191. Loree JM*, et al.* (2017) Not all RAS mutations created equal: Functional and clinical characterization of 80 different KRAS and NRAS mutations. *Journal of Clinical Oncology* 35(15_suppl):3589-3589.
192. Huang WYC*, et al.* (2019) A molecular assembly phase transition and kinetic proofreading modulate Ras activation by SOS. *Science* 363(6431):1098.
193. Davies H*, et al.* (2002) Mutations of the BRAF gene in human cancer. *Nature* 417(6892):949-954.
194. MacNicol MC, Muslin AJ, & MacNicol AM (2000) Disruption of the 14-3-3 Binding Site within the B-Raf Kinase Domain Uncouples Catalytic Activity from PC12 Cell Differentiation*. *J Biol Chem* 275(6):3803-3809.
195. Liau NPD*, et al.* (2020) Negative regulation of RAF kinase activity by ATP is overcome by 14-3-3-induced dimerization. *Nature Structural & Molecular Biology* 27(2):134-141.
196. Thorson JA*, et al.* (1998) 14-3-3 proteins are required for maintenance of Raf-1 phosphorylation and kinase activity. *Molecular and cellular biology* 18(9):5229-5238.
197. Tzivion G, Luo Z, & Avruch J (1998) A dimeric 14-3-3 protein is an essential cofactor for Raf kinase activity. *Nature* 394(6688):88-92.
198. Jin T*, et al.* (2017) RAF inhibitors promote RAS-RAF interaction by allosterically disrupting RAF autoinhibition. *Nature Communications* 8(1):1211.
199. Brady DC*, et al.* (2014) Copper is required for oncogenic BRAF signalling and tumorigenesis. *Nature* 509(7501):492-496.
200. Turski ML*, et al.* (2012) A novel role for copper in Ras/mitogen-activated protein kinase signaling. *Molecular and cellular biology* 32(7):1284-1295.
201. Hatzivassiliou G*, et al.* (2010) RAF inhibitors prime wild-type RAF to activate the MAPK pathway and enhance growth. *Nature* 464(7287):431-435.